Alma Mater Studiorum · Università di Bologna

Scuola di Scienze
Corso di Laurea Magistrale in Fisica

Morphological and Optical Properties of SiON Thin Films for Photovoltaic Applications

Relatore:
Prof. Daniela Cavalcoli

Presentata da:
Enrico Di Russo

Correlatore:
Dott. Martina Perani

Sessione III
Anno Accademico 2013/2014

Contents

Riassunto 3

Abstract 5

1. Solar Cells 7

1.1 Solar Energy and Solar Electricity 7

1.2 First Generation Solar Cells 10

1.3 Second Generation Solar Cells 11

1.4 Third Generation Solar Cells 11

1.5 High Efficiency Silicon Solar Cells 12

1.6 Hetero-Junctions with Intrinsic Thin-Layers 14

2. Surface Properties 15

2.1 Height Distribution Functions 15

2.2 Autocorrelation Function. 17

2.3 Height-Height Correlation Function 19

2.4 Power Spectra Density Function. 20

2.5 Self-Affine Surfaces 21

2.6 Mounded Surfaces 23

3. Optical Properties 25

3.1 Interband Transitions 25

3.2 Optical Energy Gap 32

3.3 Urbach Tails 34

3.4 Determination of Absorption Coefficient 35

4. Materials and Methods **39**

4.1 PECVD Deposition and Annealing Treatment **39**

4.2 Samples **41**

4.3 Atomic Force Microscopy and Image Processing **44**

4.4 Optical Spectroscopy **49**

5. Experimental Results **57**

5.1 Measurements of RMS Roughness at Different Magnifications **57**

5.2 Annealing Effect on Surface Morphology **60**

5.3 Changes in Surface Morphology with Increasing R(N_2O). **67**

5.4 Changes in the Morphology Induced by the Growth Substrate. **71**

5.5 Annealing Effect on Optical Properties. **72**

5.6 R(N_2O) Effects on Optical Properties. **77**

5.7 The Effects of Doping on the Optical Properties and the Band Structure **78**

Conclusions **83**

List of Abbreviations **85**

Bibliography **87**

Publications **90**

Ringraziamenti **91**

Riassunto

Nell'ultimo decennio si è assistito ad un incredibile sviluppo del settore delle energie rinnovabili. Il crescente interesse verso fonti di energia ecosostenibili, associato alla forte diminuzione dei costi di fabbricazione delle celle solari, ha portato il fotovoltaico ad una rapida diffusione, soprattutto in Germania e Italia. In particolare l'attenzione dei ricercatori è stata rivolta allo sviluppo di nuovi tipi di celle solari, dette di terza generazione, caratterizzate da un'elevata efficienza. In questo dinamico panorama la ricerca di materiali innovativi ha ricoperto un ruolo fondamentale.

In questa tesi sono indagate le proprietà morfologiche e ottiche di film sottili ossinitruro di silicio nanocristallino (nc-$\mathrm{SiO_xN_y}$). Questo complesso materiale presenta ottima conducibilità elettrica, ampi energy-gap e alta trasmittanza, tutte caratteristiche che lo elevano a ideale candidato per applicazioni in celle solari fotovoltaiche ad eterogiunzione.

I film di nc-$\mathrm{SiO_xN_y}$, depositati presso l'Università di Costanza (Germania), sono stati studiati impiegando tecniche di microscopia a forza atomica e spettroscopia ottica. Lo scopo principale della tesi è quello di sviluppare un metodo di indagine in grado di analizzare le proprietà morfologiche e ottiche di questo nuovo materiale, studiando l'adattabilità dei modelli attualmente impiegati per descrivere le caratteristiche del silicio.

I dati raccolti durante questo lavoro saranno poi utilizzati per meglio comprendere l'evoluzione delle varie proprietà del nc-$\mathrm{SiO_xN_y}$ in funzione dei parametri di deposizione dei films sottili. La scelta delle caratteristiche dei film che verranno depositati sulle celle solari finali sarà effettuata considerando un ampio spettro di proprietà elettriche, ottiche e strutturali, indagate mediate differenti tecniche sperimentali che completano questo lavoro di tesi. Il naturale sviluppo del programma di ricerca sul nc-$\mathrm{SiO_xN_y}$ per applicazioni fotovoltaiche sarà la creazione di una cella solare perfettamente funzionante e il conseguente studio sul miglioramento dell'efficienza di questa.

Abstract

In the last years technologies related to photovoltaic energy are rapidly developed and the interest on removable energy source substantially increased. In particular, cost reduction and appropriate feed-in tariff contributed to increase photovoltaic installation, especially in Germany and Italy. However, for several technologies, the observed experimental efficiency of solar cells is still far from the theoretical maximum efficiency, and thus there is still room for improvement. In this framework the research and development of new materials and new devices is mandatory.

In this thesis the morphological and optical properties of thin films of nanocrystalline silicon oxynitride (nc-SiO_xN_y) have been investigated. This material has been investigated in view of its application in Si based heterojunction solar cells. Amorphous SiO_xN_y has already showed excellent properties, such as electrical conductivity, optical energy gap and transmittance higher than a-Si:H, which is used now in these cells as emitter layer. Nc-SiO_xN_y has never been investigated up to now but its properties can ever surpass the ones of amorphous SiO_xN_y.

The films of nc-SiO_xN_y have been deposited at the University of Konstanz (Germany). The properties of these films have been studied using of atomic force microscopy and optical spectroscopy methods. As this material is complex as is made by different coexisting phases, the main purpose of the thesis is to develop methods to analyze the morphological and optical properties of nc-SiO_xN_y, and to study the reliability of the model used to describe the characteristics of these silicon films.

The collected data will be used understand the evolution of the properties of nc-SiO_xN_y, where the deposition parameters of the films change. The results here obtained show that nc-SiO_xN_y films have even better properties with respect to both a-Si:H and a-SiO_xN_y, i. e. higher optical band-gap and transmittance. In addition, the analysis of the variation of the observed properties as a function of the deposition parameters allows for the optimization of deposition conditions for obtaining optimal efficiency on a HIT cell with SiO_xN_y layer.

1. Solar Cells

In the first chapter a brief overview on the PhotoVoltaic (PV) technology of the last years is discussed. A very comprehensive discussion of this argument is reported in reference [1]. In particular the evolution Si-based solar cells architecture is presented and how nano-crystalline hydrogenated silicon oxy-nitride (nc-$\mathrm{SiO_xN_y}$:H) could be used in a solar cell is shown.

1.1 Solar Energy and Solar Electricity

The sun energy that reaches the earth is $1.8 \cdot 10^{17}$ watt (W) per year. This value is about 10^4 times the word energy consumption. The solar irradiance is the amount of power that the sun deposits per unit area that is direct exposed to sunlight and perpendicular to it. Because the earth distance from the sun is about 150 millions of km the solar irradiance is 1368 W/m^2. This measure is called the solar constant. The atmosphere of the earth attenuates part of this radiation and less power arrives at the surface. In good atmospheric conditions about 1000 W/m^2 reaches the surface when the sun is near the zenith. The sun energy shows a spectral dependence in agreement with black body radiation law (fig. 1.1).

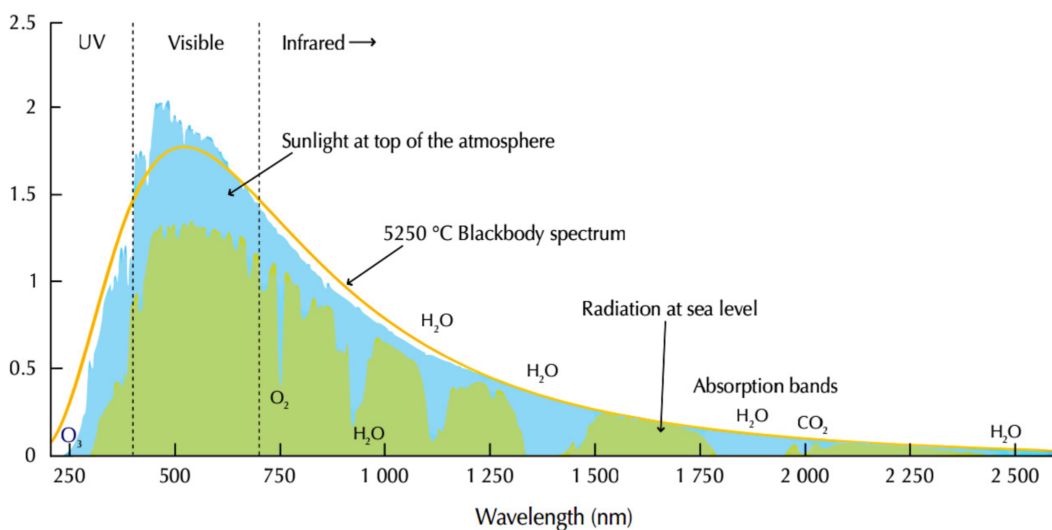

Figure 1.1: It is shown the spectrum of solar radiation at the top of the atmosphere (blue) and at the sea level (green) [1].

Of these 1000 W/m^2:

- 23% are reflected back to space by the clouds and the atmosphere;
- 20% are absorbed by the atmosphere;
- 57% hits on average the earth surface.

About 885 million terawatt-hour (TWh) reacts with the surface of the earth in a year (a watt-hour is equal to 3600 joule). It is estimated that this quantity is 6200 times the commercial primary energy consumed by humankind in 2008. The average energy received in Europe is about 1200 kWh/m^2 per years. USA, Africa, large fraction of Latin America, Australia, most of India and parts of China could be good-to-excellent solar energy producers.

The photovoltaic technology is based on the photoelectric effect discovered by Edmond Becquerel in 1839. This effect was explained in 1905 by Albert Einstein, who won the Nobel Prize in 1921. The first patents for solar cells were filed in the 1920s by Walter Snelling and Walter Schottky. The silicon solar cell for space applications was developed by Calvin Fuller and Gerald Pearson in 1954. PV was adapted to terrestrial applications in the early 1970s and the use of thin-films is appeared for the first time in 1986. Afterwards the growth of the global PV has been impressive since 2003 (fig. 1.2). The average annual growth rate was 40% in 2009 and about 135% in 2010.

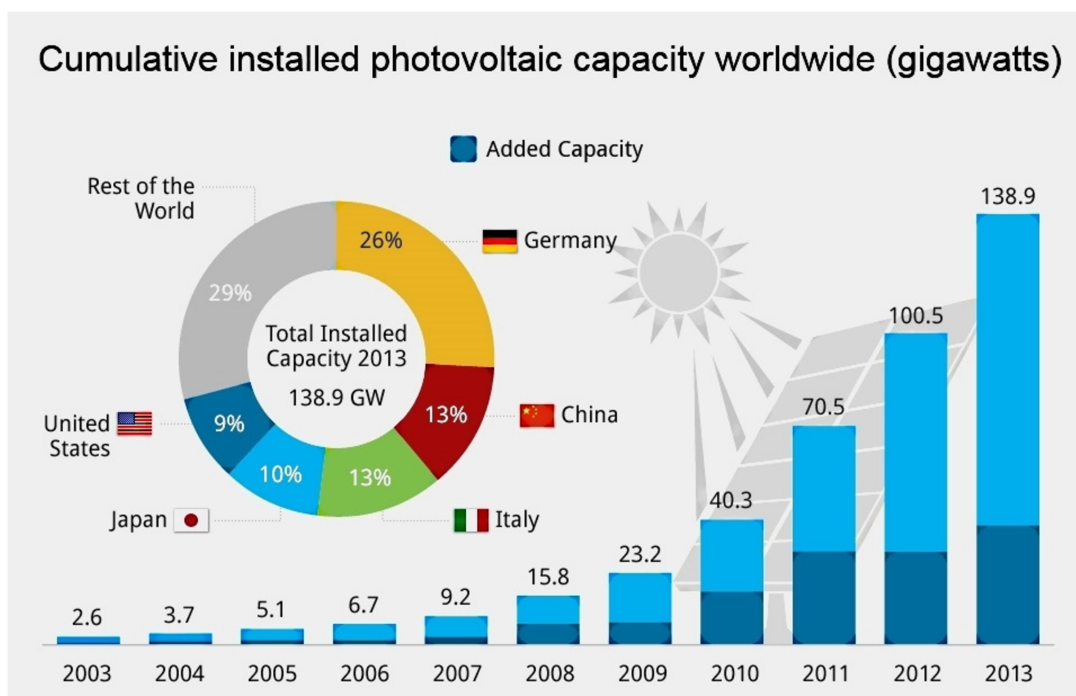

Figure 1.2: Cumulative installed photovoltaic capacity worldwide from 2003 to 2013 [2].

The PV Learning Rate (LR) is the highest even seen in the energy sector. The LR is defined as the rate of change in average cost (in dollars) as a function of the cumulative production. The LR for PV modules was 19.3% per year on average over 1976-2010 (fig. 1.3). The three principal costs reduction factors associated to the PV technology from 1980 to 2001 are the following:

1. the manufacturing cost: the role of scaling-up in cost reduction is fundamental for the success of the large scale production;
2. the increase of PV module efficiency and the role of public research: 10 out of the 16 major advancements in module efficiency can be traced back to government and university research programs;
3. the reduction of the cost of purified silicon.

In 2013, the lowest manufacturing cost of a PV modules is USD 0.57 per watt-peak (W_p is a measure of the nominal power of a PV device), achieved by the cadmium-telluride (CdTe) modules made by the PV company *First Solar*. The cost of this technology for the large scale applications was around USD 0.9/W_p. Silicon PV modules had a manufacturing cost of 1.8 USD/W_p.

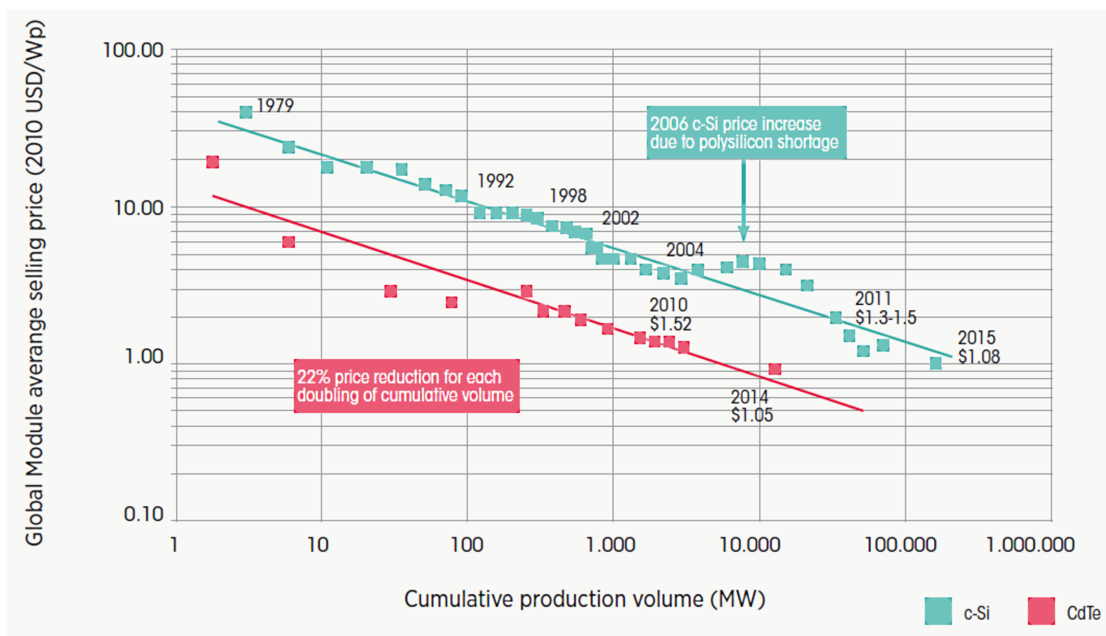

Figure 1.3: Price and learning rate for CdTe and Si PV modules [1].

Solar cell technology can be divided into three main generations. The first generation refers to cells that are relatively expensive to produce, and have a low efficiency. The second generation refers to solar cells that have an even lower efficiency, but are much cheaper to produce, such that the cost per watt is lower than in first generation cells. The term third generation is referred to cells that are very efficient. Most technologies in this generation are not yet commercialized, but there is a lot of

research going on in this area. The goal is to make third generation solar cells cheap to produce.

1.2 First Generation Solar Cells

The solar cell efficiency η is the ratio of the electrical output of a solar cell to the incident energy (fig. 1.4). If P_m is the maximum power output, E the effective solar irradiance and A the solar cell area, it is possible to write η as:

$$\eta = \frac{P_m}{E \cdot A}. \qquad (1.1)$$

First-generation solar cells are made from silicon doped with boron or phosphorous forming a p-n junction. Silicon cells have quite high efficiency η but the price is high compared to the power output because these cells required very pure silicon that is a very expensive material. Silicon cells are divided into single-crystal silicon (c-Si) cells and multy-crystalline silicon (mc-Si) cells. c-Si cells show efficiencies from 14% to 22%, mc-Si from 12% to 19%. The sc-Si cell represents the most mature PV technology but requires further reduction of the thickness of the cells to reduce the energy and labor costs and to increase the efficiency and lifetime of the cells. Around 85% of manufactured solar cells are based on crystalline silicon (c-Si).

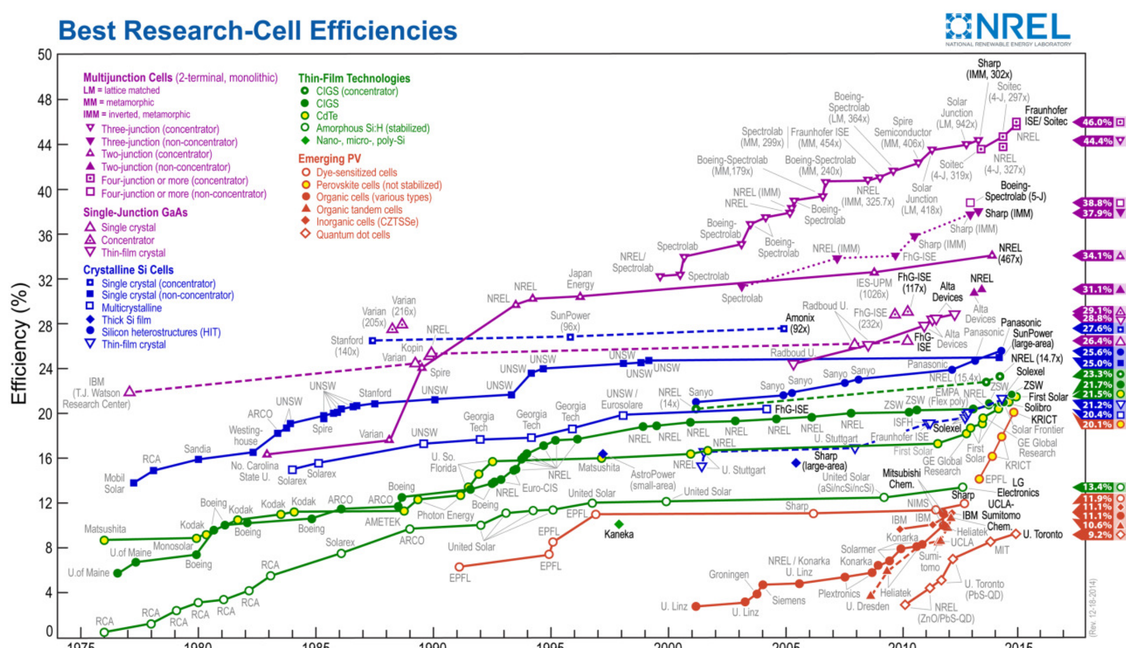

Figure 1.4: Solar cells efficiency η for different solar cells types and manufactures. [3].

1.3 Second Generation Solar Cells

The second-generation solar cells are represented by thin-film solar cell. Thin-film solar cell are made up by thin layers (1 to 4 µm thick) deposited onto a large inexpensive substrate such as glass, metal or polymer. This technology requires less semiconductor materials in order to absorb the same amount of sunlight. The principal types of thin-films solar cell that are commercially developed could be divided into three categories.

1. Amorphous silicon (a-Si) based cells are the most developed and widely known. A-Si could be deposited on cheap and large substrates, based on continuous deposition techniques that reduce manufacturing costs. The solar cells efficiencies are from 8% to 12%. The main disadvantage of a-Si solar cells is that they suffer a significant reduction in power output over time (15% to 35%), as the sun degrades the cell performance. This degradation effects is the Staebler-Wronsky Effect (SWE), discovered in 1977 [4]. It is observed that the solar cells efficiency drops during the first thousand hours of operations and the most common solution to reduce this effect is to substitute a-Si with nano-crystalline silicon (nc-Si) or hydrogenated amorphous Si (a-Si:H). Although it is observed that the Staebler-Wronsky effect could be reversed by annealing the material at temperatures of about 150°C and the performance of the solar cells are largely restored.
2. CdTe cells have lower production cost and highest cell efficiency than other thin-film technologies. Cadmium and tellurium are the by-products of zinc mining and copper processing. The problems associated to CdTe solar cells are that cadmium is a very toxic element and tellurium is produced in very low amounts.
3. Copper Indium diSelenide (CIS) and Copper-Indium-Gallium-Diselenide (CIGS) have the highest efficiencies of all thin-film cells. CIGS thin-films are often used to produce flexible and colored PV modules, going from the building-adapted (BAPV) to the building- integrated (BIPV) PV.

1.4 Third Generation Solar Cells

The third generation solar cells include advance thin-films and organic solar cells at pre-commercial stage. The fundamental third-generation PV technologies are divided in the following categories.

1. Organic solar cells are composed of organic or polymer materials. They are inexpensive but have very low efficiency and short life-times. Organic cells can be obtained by usual printing technologies, making them flexible and ideal for unever surfaces. Another advantage is that the materials used are non-toxic.
2. Muti-junction solar cells are made by semiconductors compounds from groups III and V of the period table and show highest efficiency η (fig. 1.4). They are made by a stack of layered p-n junctions and each layer is formed on semiconductors with different energy gap (E_g) to absorbs as much as the solar spectrum as possible. The materials most widely used are Ge (E_g= 0.67 eV), GaAs or InGaAs (E_g= 1.4 eV) and InGaP (E_g= 1.85 eV). A triple-junction cell based on semiconductors with band gaps of 0.74, 1.2 and 1.8 eV could achieve a theoretical efficiency of 58%. Due to their complexity and high cost, multi-junctions are used only for small-area cells with high sunlight concentration and for space applications.
3. Quantum Dot Solar Cells (QDSCs) are based on promising technologies. Quantum confinement phenomena at small semiconductor nano-crystal allow for obtaining systems with band gap. Quantum dots typically show enhanced v, but actually the QDSCs show efficiency <10%.

1.5 High Efficiency Silicon Solar Cells

The evolution of silicon solar cells is discussed in detail by [5]. In order to achieve high efficiency several issues must be considered:

1. enhancement of sun light absorption. This is typically achieved with light trapping architecture pyramidal that are first used in 1974, increasing the cells performance by 10-15% relative. Silicon nitride as antireflection coatings has been introduced from 1984, increasing the silicon solar cells efficiency to 17-18%. Since them, the performance of the best laboratories silicon solar cells has improved by 40-50% relative.
2. optimization of electrical contact. Silver (Ag) is the major component used in the screen-printing technique.

A standard solar cell in 1970s is shown in fig. 1.5. Among the high efficiency solar cells it is worth interesting Hetero-junction with Intrinsic Thin-layer (HIT) cells developed by *SANYO Electric* in 1992. Currently, the HIT efficiency is about 26%. The structure of HIT cells is shown in fig. 1.6: an intrinsic amorphous-silicon (i(a-Si)) layer and a doped amorphous-silicon layer are deposited on both sides of a c-Si substrate. Finally, a Thin-Conductive Oxide (TCO) is grown over the p^+(a-Si).

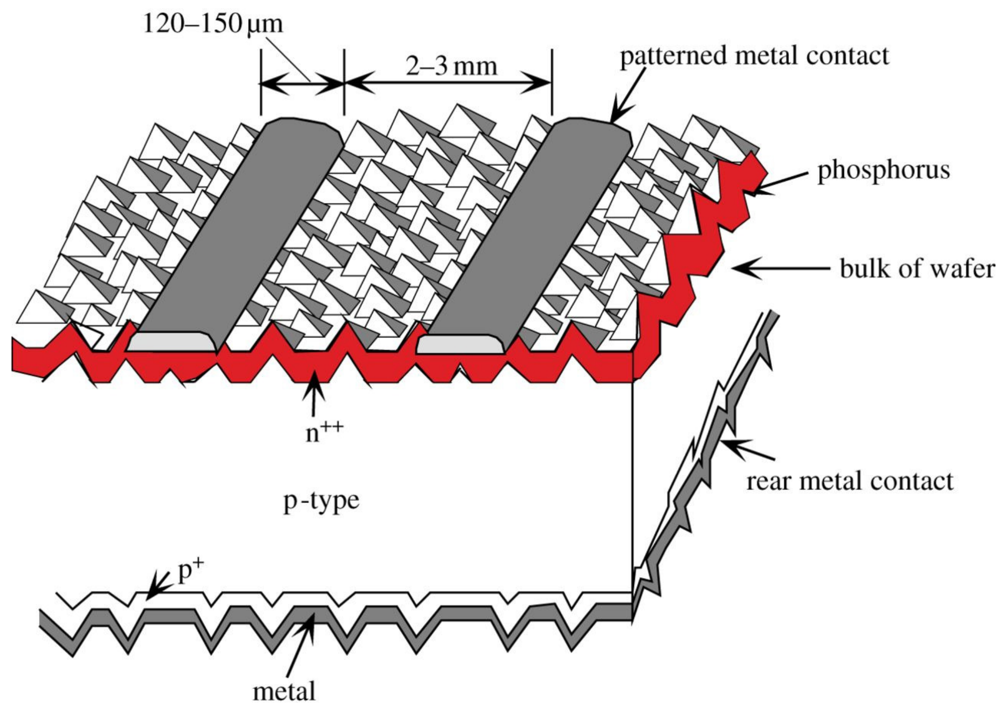

Figure 1.5: Standard screen-printed silicon solar cell in 1970s [5].

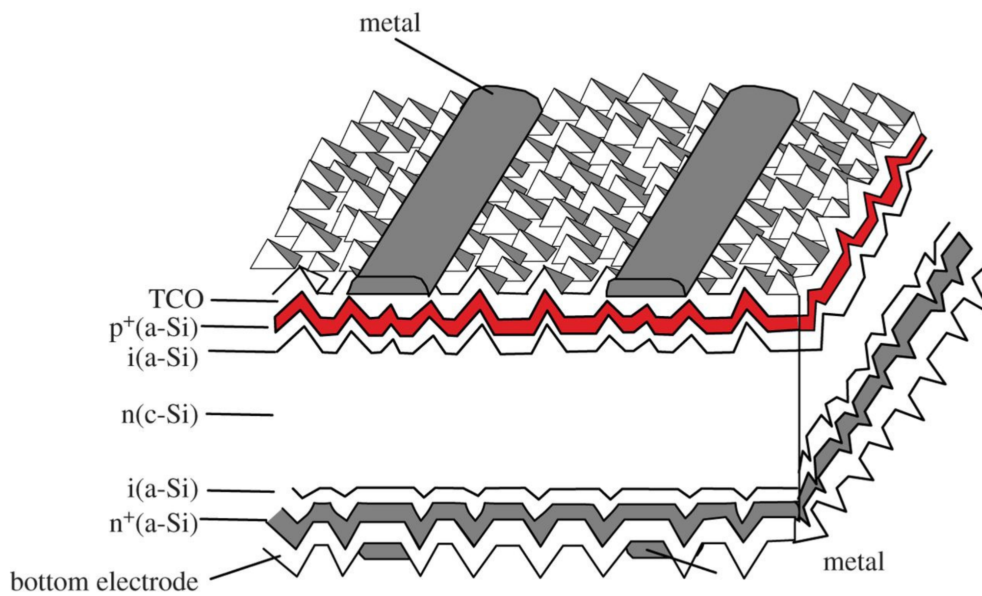

Figure 1.6: Structure of a HIT solar cell [5].

1.6 Hetero-Junction with Intrinsic Thin-Layer

The emitter layer in HIT cells is usually made with hydrogenated amorphous Si (a-Si:H) [6] (fig. 1.6). However a-Si:H presents some issues:

a) Light induced degradation. In c-Si Si atoms are connected by four covalent bounds to four other Si atoms. In a:Si it is not present the same tetrahedral bonding structure and Si atoms create a non-crystalline structure with some dangling-bonds. In a-Si:H the Si-H bonds allows for reconstruction and passivation of dangling-bonds. Si atoms are covalently bonded with three Si neighbors, and the fourth can be found in a Si-H bound. Therefore, hydrogen significantly reduces the dangling-bonds that act like recombination centers in the material. Light induced degradation increases the number of dangling-bonds due to the breaking of weak or strained Si-Si or Si-H bonds.
b) high resistivity. The solar cell power output is reduced if the emitter layer of the cell presents high resistivity, as shown in fig. 1.6.
c) high parasitic absorption. A considerable fraction of solar radiation can be absorbed by a-Si:H layer.

In the last years it is observed [7] that it is possible to use amorphous silicon oxide (a-SiO_x) or amorphous silicon oxy-nitrides (a-SiO_xN_y) instead a-Si with an increasing of the solar cell efficiency. In particular the replacement of a-SiO_xN_y with nc-SiO_xN_y can reduce the contact resistance between this layer and the TCO can be reduced. Another interesting feature of nc-SiO_xN_y is the high optical energy-gap, that reduced parasitic absorption.

The thesis aims to explore morphological and optical properties of the nc-SiO_xN_y layers as function of the deposition parameters. This material is complex, as it contains nano-crystals (nc), nc clusters, different phases and possible variable composition. Therefore, the study of its microscopical properties and the understanding of their relation with macroscopical ones is of major importance.

2. Surface Properties

In the present chapter are discussed the parameters used to describe the surface property of nc- SiO_xN_y films. The morphological features of the films surfaces are investigating using atomic force microscopy techniques.

2.1 Height Distribution Functions

The parameters used to describe surface properties are widely discussed by [8] and [9]. The height distribution function *p*(*h*) is one of the main characteristics of a surface: *p*(*h*) describes the probability to find a point of the surface at height between *h* and *h+dh*. The non-negative distribution function *p*(*h*) could be normalized as follows:

$$\int_{-\infty}^{+\infty} p(h)dh = 1\,. \tag{2.1}$$

Surfaces with different characteristics may have different height distributions: the mostly used is the Gaussian height distribution, with $\langle h \rangle$ the average height over all the surface points:

$$p(h) = \frac{1}{\sqrt{2\pi}R} exp\left(-\frac{h - \langle h \rangle}{2R^2}\right). \tag{2.2}$$

The Root Mean Square (RMS) value *R* is used to quantify the roughness amplitude as:

$$R = \sqrt{\frac{1}{N}\sum_{\boldsymbol{x}}(h(\boldsymbol{x}) - \langle h \rangle)^2}\,, \tag{2.3}$$

where $h(\mathbf{x})$ is the height at the position **x** (in the map) and *N* is the total number of averaged points. Surfaces with different RMS roughness exhibits very different surface features, as shown in fig. 2.1.

Another possible definition of RMS roughness is:

$$R^* = \sqrt{\frac{1}{L}\sum_{j=1}^{L} r_j^2} \ , \qquad (2.4)$$

where r_j is the RMS roughness calculated on the scan line *j* and *L* is the total number of scan lines of the map (for a map with *L*x*L* points).

In addition, the average roughness R_a is also used and defined as:

$$R_a = \frac{1}{N}\sum_{\boldsymbol{x}} (h(\boldsymbol{x}) - \langle h \rangle) \ . \qquad (2.5)$$

In this case it is possible to define R_a^* as the average of the R_a values calculated on the fast scan direction:

$$R_a^* = \frac{1}{L}\sum_{j=1}^{L} |r_{a\,j}| \ , \qquad (2.6)$$

where $r_{a\,j}$ is the average roughness calculated along the scan line *j*.

In this thesis both the equations (2.3) and (2.4) are used. The definition (2.4) is an excellent way to estimate the RMS roughness of a surface because it take into account the modes in which the Atomic Force Microscope (AFM) working.

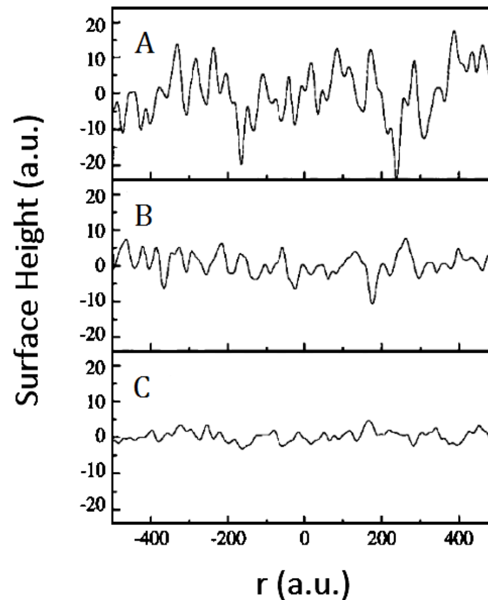

Figure 2.1: Three different rough surfaces with different RMS roughness values: (A) R= 36.6 (a.u.); (B) R=15.5; (C) R=7.5 [9].

2.2 Autocorrelation Function

The previous definitions of roughness depend on the sampling interval of the instrument used and on the map size. Using the fractal geometry method the problem is overcome if the surface is self-affine. In addiction the fractal models contain topography parameters that are independent from the resolution of the instrument used.

Statistical quantities such as the mean height and roughness do not describe correlation between different lateral positions on the surface. To overcome this, the AutoCorrelation Function (ACF) $A(\mathbf{r})$ is introduced:

$$A(\boldsymbol{r}) = \frac{1}{N \cdot R^2} \sum_{\boldsymbol{x}} \big(h(\boldsymbol{x}) \cdot h(\boldsymbol{x} + \boldsymbol{r})\big) \,. \qquad (2.7)$$

This function estimates the correlation of surface points with heights $h(\mathbf{x})$ separated laterally by a vector **r**. If the statistical behavior of the surface does not depend on the direction of the vector **r** the surface can be considered isotropic and the autocorrelation function depends only on $|\mathbf{r}| = r$. Thus the autocorrelation function becomes $A(r)$. An example of ACF associated to a real AFM map is shown in fig. 2.2.

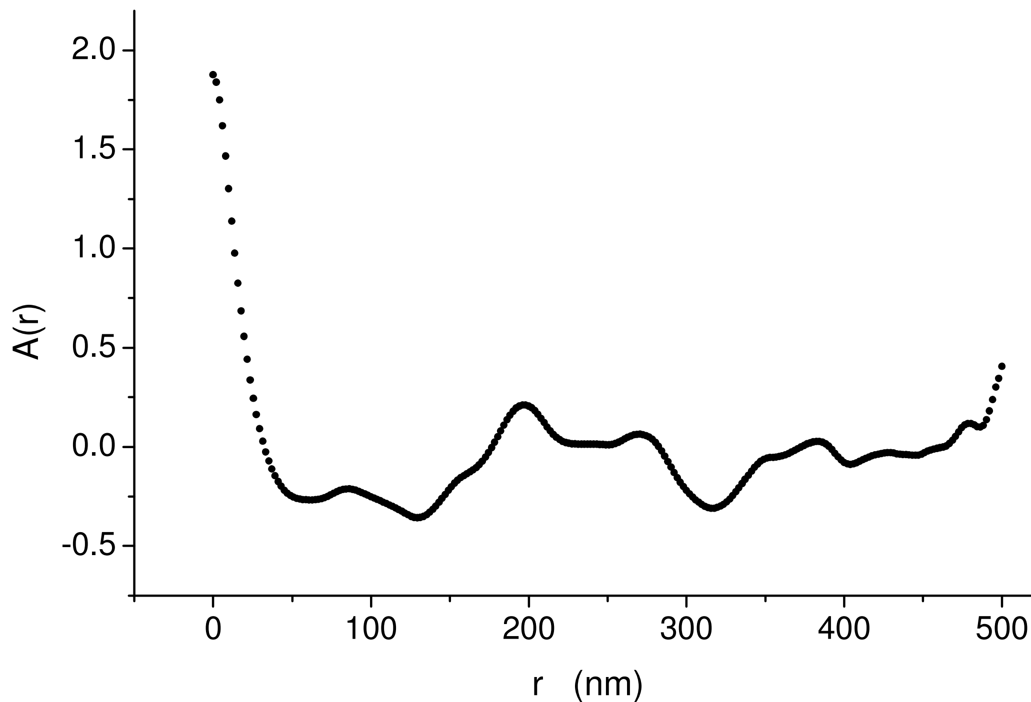

Figure 2.2: ACF associated to a real AFM map.

The general properties of $A(r)$ can be deduced from (2.7):

a) if $\langle h \rangle = 0, r = 0,\ A(0) = 1;$
b) $A(0)$ is the maximum of $A(r);$
c) $A(r)$ is a decreasing function of r.

For a random rough surface, the ACF is very important because it describes the surface morphology. Two different surfaces can exhibit the same Gaussian height distribution but different values of lateral correlation lengths ξ and RMS, as shown in fig.2.3. The lateral correlation length ξ is the value of *r* at which $A(r)$ decreases to *1/e* of its original value:

$$A(\xi) = \frac{1}{e}. \tag{2.8}$$

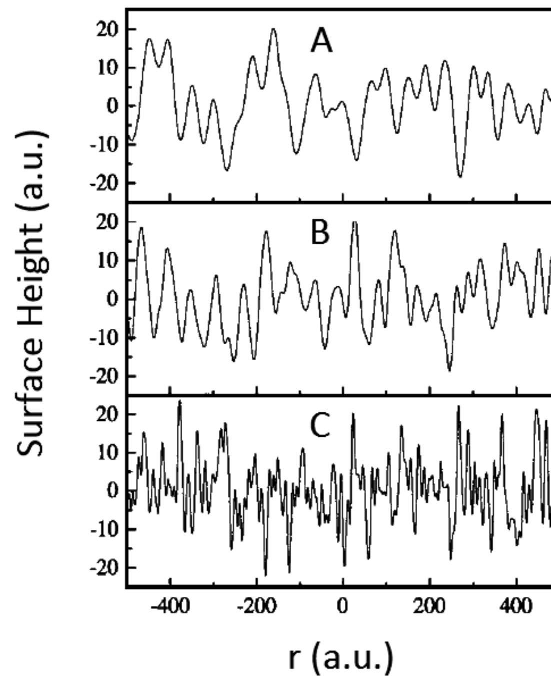

Figure 2.3: Surface profiles with the same Gaussian height distribution but different lateral correlation lengths [9].

For a Gaussian isotropic rough surface the ACF is:

$$A(r) = exp\left[-\left(\frac{r}{\xi}\right)^2\right]; \tag{2.9}$$

for an exponential isotropic rough surface the ACF is:

$$A(r) = exp\left[-\left(\frac{r}{\xi}\right)\right]. \quad (2.10)$$

The lateral correlation length ξ has the following physical meaning: two points of the surface are correlated significantly (on average) if their lateral separation is less than the lateral correlation length ξ. However, if the separation between two points at the surface is much larger than ξ, the heights at these two points are independent of one other. The study of ξ can provide information on the growth of the material investigated.

2.3 Height-Height Correlation Function

A more accurate way to determine the RMS roughness is to study the Height-Height Correlation Function (HHCF). This function is defined as:

$$H(\mathbf{r}) = \frac{1}{N}\sum_{\mathbf{x}}\big(h(\mathbf{x}+\mathbf{r}) - h(\mathbf{x})\big)^2. \quad (2.11)$$

The HHCF is a function of $r = |\mathbf{r}|$ only for isotropic rough surface. The relation between $A(r)$ and $H(r)$ is:

$$H(r) = 2R^2[1 - A(r)]. \quad (2.12)$$

An example of HHCF associated to a real AFM map is shown in fig. 2.4. From the properties of the autocorrelation function $A(r)$ (2.7) follows that:

a) $H(0) = 0$;
b) $H(r) \approx 2R^2$ for *r*-values large enough.

For AFM measurements, it is usually evaluated the one-dimensional HHCF based only on profiles along the fast scanning direction:

$$H_x(\tau_x) = \frac{1}{N(M-m)}\sum_{l=1}^{N}\sum_{n=1}^{M-m}\left[h_{n+m,l} - h_{n,l}\right]^2, \quad (2.12)$$

where h_1 and h_2 are the values of heights at points (x_1, y_1) and (x_2, y_2), $\tau_x = x_1 - x_2$, $\tau_y = y_1 - y_2$, $m = \tau_x/\Delta x$, *N* is the number of rows and *M* the number of columns of the AFM map. Thus, the function can be evaluated in a discrete set of values τ_x separated by the sampling interval Δx.

Note that typically average values of (2.12) are obtained with quite a limited number of data. Where τ_x is maximum the equation (2.12) is only referred to a couple of points for scanning line, and the accuracy of estimation is not good.

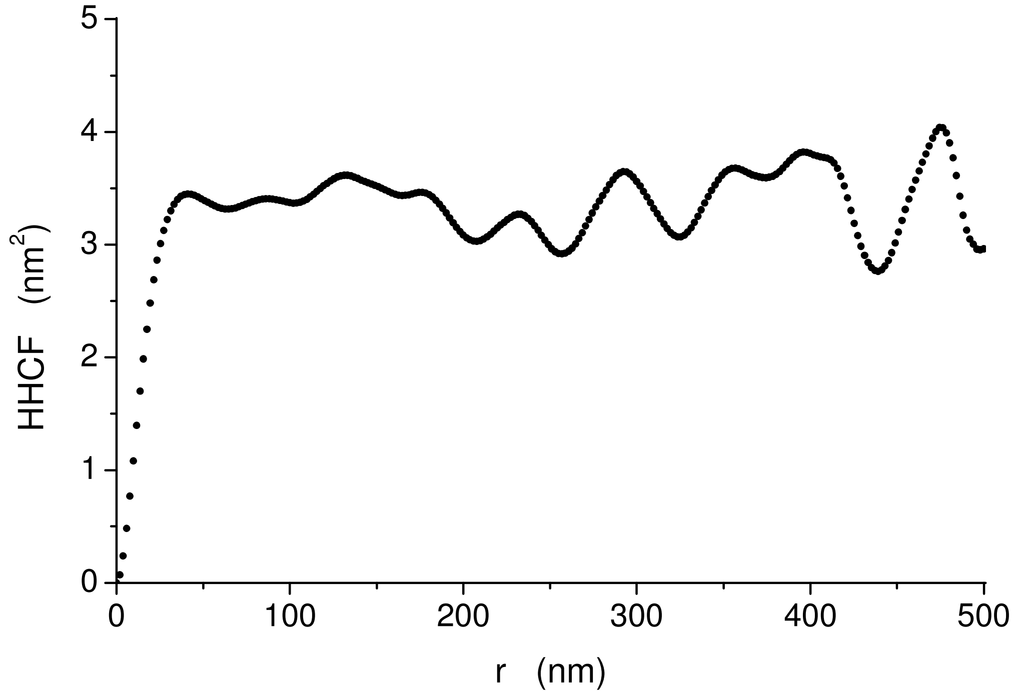

Figure 2.4: HHCF associated to a real AFM map.

2.4 Power Spectral Density Function

The Power Spectral Density Function (PSDF) is a real and non negative function related to a *d*-dimensional Fourier transform of the surface height:

$$P(\mathbf{k}) = \frac{1}{(2\pi)^d} \left| \langle h(\mathbf{x}) \rangle e^{-i\mathbf{k}\cdot\mathbf{r}} \right|^2, \tag{2.13}$$

where **k** is a wave vector in the Fourier space. The relation between ACF and PSDF is:

$$P(\mathbf{k}) = \frac{R^2}{(2\pi)^d} \int A(\boldsymbol{r}) e^{i\mathbf{k}\cdot\mathbf{r}} \mathrm{d}\mathbf{r}\,, \tag{2.14}$$

where *R* is the RMS roughness (2.3). Integrating the equation (2.14) it is possible to find the total volume in **k**-space enclosed by the PSDF:

$$\int P(\mathbf{k})\,d\mathbf{k} = \frac{R^2}{(2\pi)^d}\int A(\boldsymbol{r})\mathrm{d}\mathbf{r}\int e^{i\mathbf{k}\cdot\mathbf{r}}d\mathbf{k} =$$

$$\frac{R^2}{(2\pi)^d}\int A(\boldsymbol{r})\mathrm{d}\mathbf{r}\cdot[(2\pi)^d\delta^d(\mathbf{r})] =$$

$$= R^2\cdot A(0) = R^2, \tag{2.15}$$

because $A(0) = 1$. The PSDF can also be expressed using the HHCF:

$$P(\mathbf{k}) = \frac{R^2}{2(2\pi)^d}\int [2R^2 - H(\mathbf{r})]e^{i\mathbf{k}\cdot\mathbf{r}}\mathrm{d}\mathbf{r}. \tag{2.16}$$

For a homogeneous, isotropic, random rough surface, $P(\mathbf{k}) = P(k)$, so the power spectrum is independent from the direction chosen.

2.5 Self-Affine Surfaces

A regular fractal is an object that possesses exact self-similarity: the structures of regular fractals are exact copies of themselves at all magnification. A self-similar object looks the same when the space it occupies is distended uniformly by a factor ε.

Another way for describing the surface morphology is the self-affine fractal geometry. A self-affine object looks the same when it is distended with different ratios in some directions, so the enlarged object appears as the original object.

A rough surface can be described by a self-affine function, which has the following property:

$$h\left(x_{1,} \ldots, x_n\right) = \varepsilon_1^{-\alpha_1}, \ldots, \varepsilon_n^{-\alpha_n} h(\varepsilon_1 x_1, \ldots, \varepsilon_n x_n) \tag{2.17}$$

where α_i are called roughness exponents or Hurst exponents. Typically there is only one characteristic roughness exponent and the equation (2.17) becomes:

$$h(x) = \varepsilon^{-\alpha}h(\varepsilon x). \tag{2.18}$$

For a single exponent the value of the function is rescaled by a factor $\varepsilon^{-\alpha}$ when the *x* is reduced along the *x*-axis by a factor *1/ε*. The exponent α characterizes the short-range roughness of a self-affine surface.

For a self-affine isotropic rough surface with Gaussian correlation the ACF has the form:

$$A(r) = exp\left[-\left(\frac{r}{\xi}\right)^{2\alpha}\right], \qquad 0 \leq \alpha \leq 1. \tag{2.19}$$

The height-height correlation function *H(r)* becomes:

$$H(r) = 2R^2\left[1 - exp\left[-\left(\frac{r}{\xi}\right)^{2\alpha}\right]\right] = \begin{cases} \rho^2 r^{2\alpha} & for\ r \ll \xi; \\ 2R^2 & for\ r \gg \xi. \end{cases} \tag{2.20}$$

where ρ is the average local slope, α the roughness exponent $(0 \leq \alpha \leq 1)$ and ξ is the lateral correlation length. The value of α describes how locally wiggly the sample surface is, or to what degree the surface randomly fluctuates in short range. As shown in fig. 2.5 a big value of α is related to a locally smooth surface structure, a small one to a locally jagged morphology.

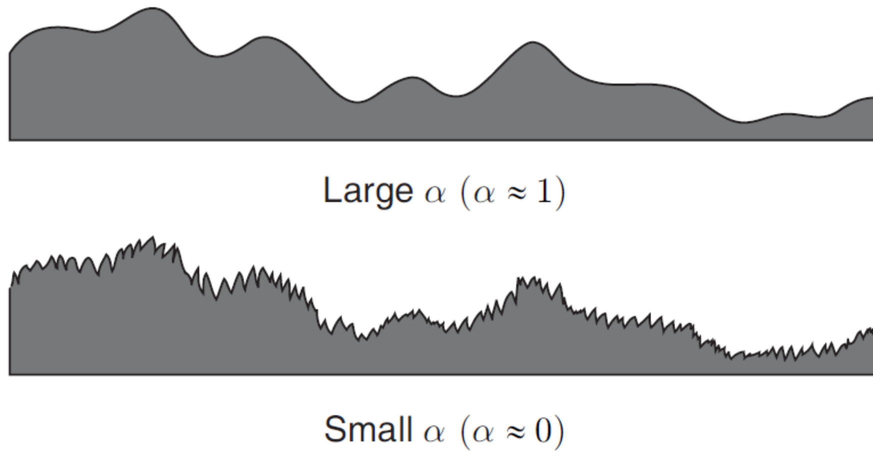

Figure 2.5: The figure shows a comparison of the local surface morphology for a surface with similar values for the RMS roughness R, but different values of α [8].

The roughness exponent α can be extracted from a log-log plot of *H(r):* for $r \ll \xi$ the slope is equal to 2α. For sufficiently large *r* the HHCF turns into a plateau: the turning point estimates ξ. The lateral correlation length ξ provides a length scale that distinguishes the short-range and long-range behaviors of a rough surface (fig. 2.6).

A real thin film surface exhibits self-affine behavior over a certain length scale, and there is a cutoff length scale beneath which the surface may not be self-affine. It is typically supposed that the cutoff length is smaller than the correlation length ξ.

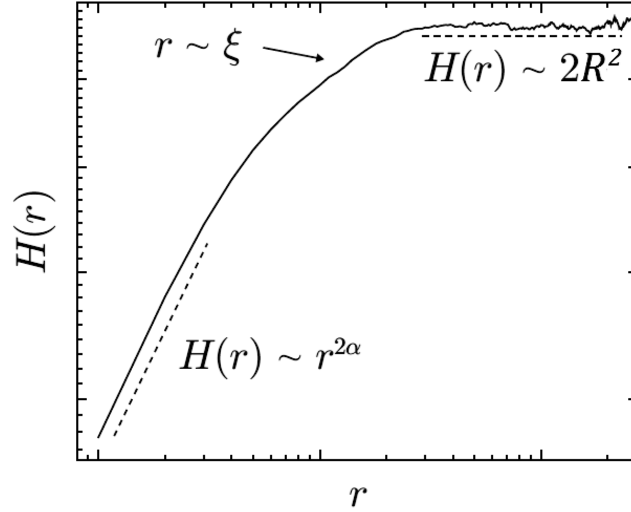

Figure 2.6: HHCF obtained from a simulated self-affine surface [8].

2.6 Mounded Surfaces

The lateral correlation length is not an absolute characteristic length scale of a self-affine surface but a relative length scale. It is impossible to determine a characteristic length scale because it is possible to apply several times the transformation (2.17) and the surface always appears the same.

A surface that possesses a characteristic length scale is called mounded surface. Mounded surfaces are not self-affine surfaces and have a characteristic length scale called wavelength λ. The ACF of mounded surface exhibits oscillations due to the presence of mounds. The lateral correlation length ξ is well defined by the autocorrelation function and is the length beyond which surface heights where not significantly correlated.

The PDSF typically shows a main peak that is associated to a wavenumber k_m . λ is a measure of the average distance between mounds and is defined as:

$$\lambda = \frac{2\pi}{k_m}. \tag{2.21}$$

The wavelength λ and the lateral correlation length ξ are different objects but they must satisfy the relation $\xi \leq \lambda$ because mounds are separated by at least their size. If mounds grow next to each other we have $\xi = \lambda$.

The HHCF for a mounded surface is similar to the HHCF for a self-affine surface (2.16). If $r > \xi$ the HHCF is not constant but periodic for a mounded surface. The presence of frequency peak in PDSF implies that the surface profile has a quasi-periodic behavior which is reflected in an oscillatory behavior of HHCF at $r > \lambda$. For a 2+1 dimensional surfaces the HHCF becomes:

$$H(r) = 2R^2 \left[1 - exp\left[-\left(\frac{r}{\xi}\right)^{2\alpha}\right] J_0\left(\frac{2\pi r}{\lambda}\right)\right] \tag{2.22}$$

where J_0 is the zero-order Bessel function.

If $r \ll \lambda$, $J_0(2\pi r/\lambda)$ is equal to unity and the self-affine HHCF (2.20) is obtained. Under this condition α is well defined but it has not any meaning for mounded surfaces.

3. Optical Properties

This chapter reports the description of optical transitions in crystalline and amorphous semiconductors. In particular is demonstrated the Tauc's formula for the determination of the optical energy gap. At the end of the chapter is describes the procedure to determine experimentally the absorption coefficient of a thin films and are described the effects of the thin-film interference on transmission and reflection spectra.

3.1 Interband Transitions

Optical properties of semiconductors can be obtained considering the interaction between electromagnetic radiation and the semiconductors band structure, including absorption, diffraction, polarization, reflection, refraction and scattering effects. A very comprehensive discussion of the topic is reported in reference [10].

In semiconductor the main electronic conduction mechanism is associated with free carriers at low incident light frequencies. As the photons energy increases and becomes compatible with the energy gap (E_g), interband transitions are allowed: a photon can excite an electron from an occupied state in the Valence Band (VB) to an unoccupied state in the Conduction Band (CB). In this process the photon is absorbed, a free electron state is formed in CB and a corresponding hole is left in VB. The energy gap E_g is defined as the minimum energy difference between the bottom of CB and the top of VB.

Interband transitions have a threshold energy at the energy gap. There are two different types of allowed transitions called direct and indirect. In a direct transition an electron is exited from CB to VB without a significant change in the wave vector $\vec{k}$: $E_v(\vec{k}) \rightarrow E_c(\vec{k})$. An indirect transition involves both a photon and a phonon because the band edges of the conduction and valence bands are widely separated in $\vec{k}$ space. The threshold energy for the indirect process is longer o lower than the band gap E_g: for the indirect transition between the bands edges the absorption threshold is $h\omega = E_g + \hbar\Omega$, where Ω is the frequency of the emitted phonon. The phonons energy $\hbar\Omega$ (≈0.01 to 0.03 eV) is generally much less than E_g.

The interband transitions depend on the coupling between the VB and CB. The Fermi Golden Rule gives the probability per unit time $W_{\vec{k}}$ that a photon of energy ħω makes a transition at a given $\vec{k}$ point:

$$W_{\vec{k}} \cong \frac{2\pi}{\hbar} |\langle v|H'|c\rangle|^2 \delta\left[E_c(\vec{k}) - E_v(\vec{k}) - \hbar\omega\right], \qquad (3.1)$$

where the matrix element for the electromagnetic perturbation H' is taken between the valence and conduction band Bloch states at wave vector $\vec{k}$ and the δ-function $\delta\left[E_c(\vec{k}) - E_v(\vec{k}) - \hbar\omega\right]$ expresses energy conservation evaluated at $\vec{k}$.

It is possible to integrate over $\vec{k}$ because the electronic states in the Brillouin zone are quasi-continuous functions of $\vec{k}$ and the wave vector for the light is small compared to the Brillouin zone dimensions. Both the perturbation matrix element and the joint density of states are $\vec{k}$-dependent, so for a 3D system:

$$W = \frac{2\pi}{\hbar} \int |\langle v|H'|c\rangle|^2 \frac{2}{8\pi^3} \delta\left[E_c(\vec{k}) - E_v(\vec{k}) - \hbar\omega\right] d^3k. \qquad (3.2)$$

If $|\langle v|H'|c\rangle|^2$ is independent of $\vec{k}$ it is possible to define the number of states per unit volume per unit energy $\rho_{cv}(\hbar\omega)$ with an energy difference between the CB and VB that is equal to the photon energy:

$$\rho_{cv}(\hbar\omega) = \frac{2}{8\pi^3} \int \delta\left[E_c(\vec{k}) - E_v(\vec{k}) - \hbar\omega\right] d^3k. \qquad (3.3)$$

The critical points (or Van Hove singularities) are the points in the Brillouin zone where $E_c - E_v$ is stationary. Here the photon energy $\hbar\omega = E_c - E_v$ induces electronic transitions over a large region of the Brillouin zone.

In 3D systems critical points are classified into four categories depending on whether the band separation increases or decreases moving from the critical points. Around the critical point $\vec{k}_0$ the Taylor series of $E_c(\vec{k}) - E_v(\vec{k})$ are:

$$E_c(\vec{k}) - E_v(\vec{k}) \approx E_g(\vec{k}_0) + \sum_{i=1}^{3} a_i (k_i - k_{0i})^2, \qquad (3.4)$$

where the energy gap is $E_g(\vec{k}_0)$ and the sum is over the three direction *x*, *y*, *z*. The coefficients a_i represent the second order derivative of the energy difference: $\frac{\partial^2}{\partial k_i^2}\left[E_c(\vec{k}) - E_v(\vec{k})\right]$. The classification of the critical points in a 3D system depends on how many a_i coefficients are negative in (3.4). The parabolic bands approximation is when only one of the coefficients a_i is negative in (3.4).

If the zero-point energy is taken in the middle of the band gap and m_c and m_v are the effective mass of the carriers in CB and VB, from the parabolic bands approximation follows:

$$E_c(\vec{k}) = \frac{E_g}{2} + \frac{\hbar^2 k^2}{2m_c} \; ; \qquad E_v(\vec{k}) = -\frac{E_g}{2} - \frac{\hbar^2 k^2}{2m_v} . \tag{3.5}$$

The reduced mass m_τ is defined by the relation:

$$\frac{1}{m_\tau} = \frac{1}{m_c} + \frac{1}{m_v} . \tag{3.6}$$

From (3.5) and (3.6):

$$E_c(\vec{k}) - E_v(\vec{k}) = E_g + \frac{\hbar^2 k^2}{2}\left(\frac{1}{m_c} + \frac{1}{m_v}\right) = E_g + \frac{\hbar^2 k^2}{2m_\tau} . \tag{3.7}$$

In the reciprocal space the constant energy surface *S* is a surface with constant energy difference between the CB and VB at each $\vec{k}$ point and:

$$d^3k = dSdk_n \, , \tag{3.8}$$

where dk_n is an element of wave vector normal to *S*.

Using the definition of gradient it is possible to write following the equation:

$$|\nabla_k E| dk_n = dE, \tag{3.9}$$

And considering surfaces with energy difference $E_c - E_v$, from (3.9) we get:

$$|\nabla_k (E_c - E_v)| dk_n = d(E_c - E_v) \, . \tag{3.10}$$

Combining (3.8) and (3.10) we can write d^3k as:

$$d^3k = dSdk_n = dS\left[\frac{d(E_c - E_v)}{|\nabla_k (E_c - E_v)|}\right] . \tag{3.11}$$

Using the result (3.11) the equation (3.3) becomes:

$$\rho_{cv}(\hbar\omega) = \frac{2}{8\pi^3} \iiint \frac{dS \, d(E_c - E_v)\delta(E_c - E_v - \hbar\omega)}{|\nabla_k (E_c - E_v)|} \, , \tag{3.12}$$

and taking advantage from the properties of δ-function it is possible to integrate over $d(E_c - E_v)$ and obtaining:

$$\rho_{cv}(\hbar\omega) = \frac{2}{8\pi^3} \iint \frac{dS}{|\nabla_k (E_c - E_v)|_{E_c - E_v = \hbar\omega}} \, . \tag{3.13}$$

$E_c - E_v$ is stationary for a critical point: in this case $\nabla_k(E_c - E_v)$ vanishes and in parabolic approximation it is possible to write the gradient of $E_c - E_v$ as:

$$\nabla_k(E_c - E_v) = \frac{\hbar^2 \vec{k}}{m_\tau}, \tag{3.14}$$

and the joint density of states (3.13) as:

$$\rho_{cv}(\hbar\omega) = \frac{2}{8\pi^3}\left[\frac{4\pi}{\hbar^2}\left(\frac{k^2 m_\tau}{k}\right)\right]_{E_c - E_v = \hbar\omega} = \left[\frac{m_\tau}{\pi^2\hbar^2}k\right]_{E_c - E_v = \hbar\omega}. \tag{3.15}$$

Reversing the equation (3.7), the relation between the absorbed photon energy $\hbar\omega$ and the crystal momentum k becomes:

$$k = \left[\frac{2m_\tau}{\hbar^2}\left(\hbar\omega - E_g\right)\right]^{1/2}. \tag{3.16}$$

In conclusion, using the result (3.16), if $\hbar\omega - E_g > 0$ the equation (3.15) becomes:

$$\rho_{cv}(\hbar\omega) = \frac{1}{2\pi^2}\left[\frac{2m_\tau}{\hbar^2}\right]^{3/2}\sqrt{\hbar\omega - E_g}. \tag{3.17}$$

In equation (3.17) it is important to observe that $\rho_{cv}(\hbar\omega) \propto \sqrt{\hbar\omega - E_g}$. This functional dependence will appear in the Tauc's formula for the determination of the optical energy gap for direct transitions.

Returning to the Fermi Golden Rule (3.1) now it is necessary to estimate the square of the matrix element $|\langle v|H'|c\,\rangle|^2$. The equation of motion of a charged particle in an electromagnetic field is [11]:

$$\frac{d}{dt}(m_\tau \vec{v}) = e\left[\vec{E} + \frac{1}{c}\left(\vec{v} \times \vec{H}\right)\right]. \tag{3.18}$$

If $\vec{A}$ is the vector potential, the Hamiltonian is:

$$H = \frac{1}{2m_\tau}\left(\vec{p} - \frac{e}{c}\vec{A}\right)^2. \tag{3.19}$$

In presence of an optical field in the solid the Hamiltonian for an electron is:

$$H = \frac{1}{2m_\tau}\left(\vec{p} - \frac{e}{c}\vec{A}\right)^2 = \frac{p^2}{2m_\tau} - \frac{e}{m_\tau c}\vec{A}\cdot\vec{p} + \frac{e^2 A^2}{2m_\tau c^2}, \tag{3.20}$$

It is possible to consider the equation (3.20) as the sum of a one-electron Hamiltonian without optical field H_0 and the optical perturbation H':

$$H' = -\frac{e}{m_\tau c}\vec{A}\cdot\vec{p} + \frac{e^2A^2}{2m_\tau c^2}. \tag{3.21}$$

If the optical field is very weak, the first order approximation of (3.21) is:

$$H' \approx -\frac{e}{m_\tau c}\vec{A}\cdot\vec{p}. \tag{3.22}$$

Assuming an absorption process in which the valence band is completely full and the conduction band completely empty, in (3.1) the matrix element is:

$$\langle v|H'|c\rangle = -\frac{e}{m_\tau c}\langle v|\vec{A}(\vec{r},t)\cdot\vec{p}|c\rangle. \tag{3.23}$$

If the light wave vector $\vec{K}$ is small compared to Brillouin zone dimension, the spatial dependence of the vector potential $\vec{A}(\vec{r},t)$ can be neglected. The square of the matrix element (3.1) becomes:

$$|\langle v|H'|c\rangle|^2 = \left(\frac{e}{m_\tau c}\right)^2 |A|^2|\langle v|p|c\rangle|^2. \tag{3.24}$$

Now it is necessary to estimate the absorption coefficient associated to an a- SiO_xN_y thin film. The light propagation through a thin film is described by Beer-Lambert's law:

$$I(d) = I(0)e^{-\alpha(\omega)d}, \tag{3.25}$$

where $I(d)$ is the intensity of light after traveling through a material of thickness *d*, $I(0)$ is the intensity of light at $d = 0$ and $\alpha(\omega)$ is the light absorption coefficient defined as:

$$\alpha(\omega) = \frac{\hbar\omega \cdot (\text{numeber of transition / unit volume / unit time})}{\text{incident electromagnetic flux}}. \tag{3.26}$$

The incident electromagnetic flux is calculated from the Poynting vector. This is defined for an electromagnetic plane wave $\vec{A} = \vec{A}_0 e^{i(\vec{K}\cdot\vec{r}-\omega t)}$ in a non-magnetic material as:

$$\vec{S} = \frac{\omega}{8\pi}\frac{\tilde{n}\omega}{c}\left|\vec{A}\right|^2\hat{K} \tag{3.27}$$

where $\tilde{n}$ is the real part of the complex index of refraction and $\hat{K}$ is a unit vector in the same direction of the Poynting vector. The quantity $|\vec{S}|$ becomes the incident electromagnetic flux in the equation (3.26).

If the absorption process at finite temperature is considered, it is also necessary to consider the Fermi functions to represent the occupation of the states:

$$f(E_v)[1-f(E_c)]-f(E_c)[1-f(E_v)]\,, \tag{3.28}$$

where the first group of terms represents the absorption process and the second the emission process. If the conduction band is nearly empty during the absorption process and the valence band is nearly full in the recombination process, the equation (3.28) becomes:

$$f(E_v)[1-f(E_c)]-f(E_c)[1-f(E_v)] \approx\; f(E_v)-f(E_c). \tag{3.29}$$

Collecting the results (3.24), (3.26), (3.27) and (3.29), the absorption coefficient (3.26) for direct interband transitions becomes:

$$\alpha(\omega)=\frac{\hbar\omega\cdot\frac{2\pi}{\hbar}\left(\frac{e}{m_\tau c}\right)^2|A|^2|\langle v|p|c\rangle|^2\,\rho_{cv}(\hbar\omega)[f(E_v)-f(E_c)]}{\frac{\omega}{8\pi}\frac{\tilde{n}\omega}{c}\left|\vec{A}\right|^2\hat{K}}. \tag{3.30}$$

Simplifying the equation (3.30) we obtain:

$$\alpha(\omega)=\frac{16\pi^2e^2}{{m_\tau}^2\mathrm{c}\tilde{n}\omega}\,|A|^2|\langle v|p|c\rangle|^2\,\rho_{cv}(\hbar\omega)[f(E_v)-f(E_c)]\,. \tag{3.31}$$

It is possible to estimate $|\langle v|p|c\rangle|^2$ with quantum-mechanical considerations and the final result is [12]:

$$|\langle v|p|c\rangle|^2\approx\frac{E_g}{2}\frac{m_0^2}{{m_\tau}^*}, \tag{3.32}$$

where m_0 is the free electron mass and m_τ the effective electron mass in the solid. At very low temperature or also at room temperature, a semiconductor has an essentially filled valence band and an empty conduction band ($f(E_v)\approx 1$ and $f(E_c)\approx 0$).

By substituting equations (3.17) and (3.26) into equation (3.31), the following frequency dependence for the absorption coefficient for direct allowed transitions can be written as follows:

$$\alpha(\omega) \propto \frac{1}{\omega}\sqrt{\hbar\omega - E_g}\,. \tag{3.33}$$

In semiconductors with indirect band gap the transition between an initial state with energy E_i and a final state with energy E_f requires that a phonon with energy $\hbar\omega_\Omega$ is emitted (+ sign) or absorbed (- sign). From the conservation of energy it is possible to write the equation:

$$\hbar\omega = E_f - E_i \pm \hbar\omega_\Omega. \tag{3.34}$$

In this case the absorption coefficients for the phonons absorption and emission are:

$$\alpha_{abs}(\omega) \cdot \hbar\omega \propto \frac{\left(\hbar\omega - E_g + \hbar\omega_\Omega\right)^2}{\exp\left(\frac{\hbar\omega_\Omega}{k_B T}\right) - 1}\;; \tag{3.35}$$

$$\alpha_{emis}(\omega) \cdot \hbar\omega \propto \frac{\left(\hbar\omega - E_g - \hbar\omega_\Omega\right)^2}{1 - \exp\left(-\frac{\hbar\omega_\Omega}{k_B T}\right)}, \tag{3.36}$$

where k_B is the Boltzmann constant and T the temperature.

The light absorption is controlled by $\alpha_{abs}(\omega)$ when the photon energy is in the range $E_g - \hbar\omega_\Omega < \hbar\omega < E_g + \hbar\omega_\Omega$. A plot of $(\alpha \cdot \hbar\omega)^{1/2}$ as function of $\hbar\omega$ has $E_g - \hbar\omega_\Omega$ as intercept point. If the photon energy is $\hbar\omega > E_g + \hbar\omega_\Omega$, the overall absorption coefficient becomes $\alpha_{abs} + \alpha_{emis}$ and when the photon energy increases α_{emis} quickly dominates over α_{abs} .

3.2 Optical Energy Gap

Tauc et al. first reported that it is possible to find the energy gap of amorphous germanium plotting $\hbar\omega(\varepsilon_2)^{1/2}$ as function of the photon energy $\hbar\omega$, where ε_2 is the imaginary part of dielectric constant. The optical energy gap E_{OPT} calculated with this method is widely known as Tauc energy gap [13].

Afterwards, E_{OPT} of tetrahedrally bounded amorphous semiconductors are usually deduced by a linear extrapolation of the $(\alpha\hbar\omega)^{1/2}$ versus $\hbar\omega$ plot to energy axis. Several experimental studies have revealed that there are other ways to determine E_{OPT}. Cody et al. [14] showed for hydrogenated silicon (Si:H) that the $(\alpha/\hbar\omega)^{1/2}$ versus $\hbar\omega$ plot has better linearity than the $(\alpha\hbar\omega)^{1/2}$ plot, in addition E_{OPT} turns to be more stable in terms of variation of sample thickness, than the $(\alpha\hbar\omega)^{1/2}$ plot. Hishikawa [15], Vorliček [16], Klazes [17] and Nitta [18] have reported that the $(\alpha\hbar\omega)^{1/3}$ or $(n\alpha\hbar\omega)^{1/3}$ versus $\hbar\omega$ plots of a-Si [16, 17], a-Ge [16] and a-Si:H [15, 17, 18] (fig. 3.1) have better linearity than the $(\alpha\hbar\omega)^{1/2}$ plot .

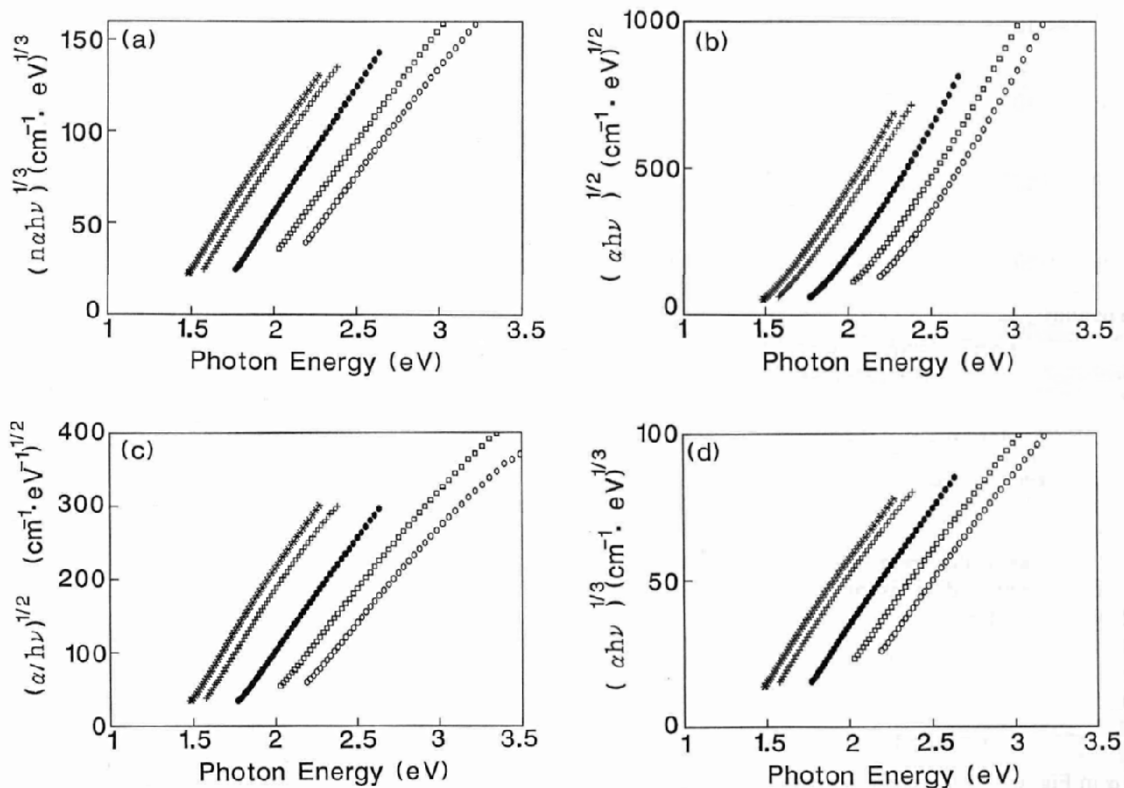

Figure 3.1: The (a) $(n\alpha\hbar\omega)^{1/3}$ *plot,* (b) $(\alpha\hbar\omega)^{1/2}$ *plot,* (c) $(\alpha\hbar\omega)^{1/3}$ *plot,* (d) $(\alpha\hbar\omega)^{1/3}$ *plot for a a-Si:H film (●), a-* $Si_{1-x}C_x$*:H film (□, ○), and a-* $Si_{1-x}Ge_x$*:H film (*,+). The linearity of the* $(n\alpha\hbar\omega)^{1/3}$ *is best among the three kinds of plots* (a)*,* (b)*,* (c)*. The* $(\alpha\hbar\omega)^{1/3}$ *versus ħω plot has almost the same linearity of* $(n\alpha\hbar\omega)^{1/3}$ *[15].*

Kruzelecky et al. [19] have reported that the $(\alpha\hbar\omega)^{1/2}$ plot for a-Si:H and a-Si films has two linear regions with different slopes (fig. 3.2). These regions are associated one to electronic transitions between extended states in CB and VB, the other to electronic transitions between localized tail states and extended states in the opposite bands.

Notwithstanding several different approaches, the equation:

$$(\alpha \cdot \hbar\omega)^{1/2} = B(\hbar\omega - E_{OPT}) \quad (3.36)$$

is widely used to define the band gap in amorphous semiconductors. The plot of $(\alpha \cdot \hbar\omega)^{1/2}$ versus the photons energy-axis gives the optical band-gap energy E_{OPT} and the scale factor of the plot *B*.

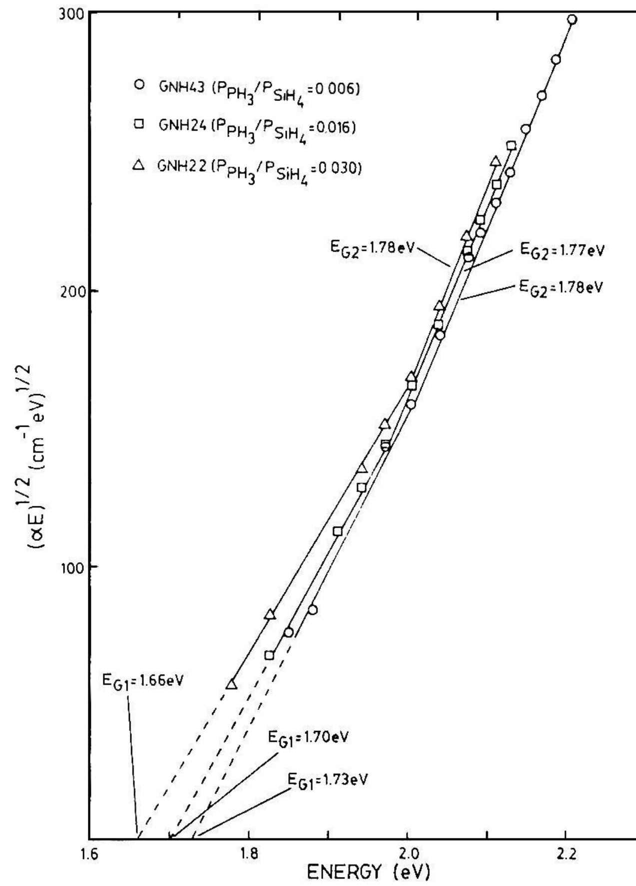

Figure 3.2: Plots of $(\alpha\hbar\omega)^{1/2}$ versus $\hbar\omega$ for three PH_3-doped a-Si:H films [19].

3.3 Urbach Tails

In optical absorption near band edges Urbach tails are observed in a variety of materials having crystal disorder of several origins. A broad discussion of the Urbach tails is reported by [20] and [21].

The pioneering experiments show that the absorption coefficient $\alpha(\omega)$ has a simple form at a low energy below the band gap:

$$\alpha(\mathrm{E}) = a_0 \cdot e^{(\mathrm{E}-E_1)^n / E_0(X,T)}, \tag{3.37}$$

where E_1, $E_0(X,T)$, a_0 and n are constants determined by fitting the experimental data and $E = \hbar\omega$ is the photons energy. $E_0(X,T)$ sets the width of the range over witch $\alpha(\omega)$ tails off exponentially. The simplest expression (3.36) having exponent $(\mathrm{E} - E_1)^n$ with $n = 1$ is known as the Urbach tail. It is possible to determine the exponent n studying $\ln \alpha(\mathrm{E}) \propto (\mathrm{E})^{\mathrm{n}}$.

In optical absorption near band edges electrons in VB are excited to empty states in CB. Urbach tails are observed when there is disorder in the band structure. In this case the electrons making transitions in a potential that differs from place to place in the material (fig. 3.1) and the edges of the conduction and valence bands blur. This happens because the electron-ion potential depends on the position into the solid. In disorder semiconductors the ionic potential loses its characteristic periodic properties, thus the band structures can be sketched as shown in fig. 3.3.

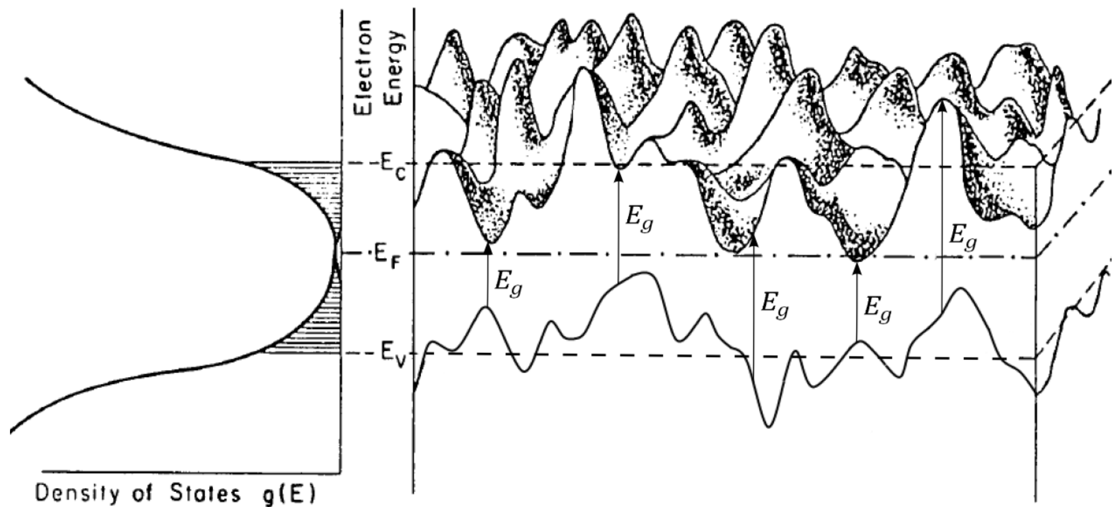

Figure 3.3: Potential fluctuations of the initial and final electron states for the optical transitions corresponding to the local energy gap E_g. The left side shows the density of states: the region of localized states lies between E_c and E_v. This figure shows only the spatial variation of $E_g$induced by the structural disorders of the solid [10].

When the disorder is large the density of electron states $g(E)$ near the band edges (in both CV and VB) develops tails which extend into the energy gap (fig.3.3). The simple form of Urbach edges is due to an equally simple exponential tail in the density of states $g(E)$. It is know that $\ln g(E) \propto (\mathrm{E})^{\mathrm{n}}$ (in three dimensions n lies in the range $0.5 \leq n \leq 2$ [22]) and for several types of disorder it was verified that $n = 1$ [23]. The exponent n is a function of the correlation length L of the band structure disorder and of the energy E. Sa-Yakanit and Glyde [21] show that for energies E near the band edge n is equal to 1 for any disorder having a length scale of order of the interatomic spacing ($L \sim 2 - 5\,Å$) leading to fluctuations in electron potential of order of atomic binding energies ($\sim(eV)^2$).

The Urbach tails were originally observed in ionic crystals having thermal disorder and in crystalline semiconductors at room temperature. A study of Urbach edges is particularly interesting for the amorphous semiconductors [20] for their application as solar cell materials. In a-Si the sunlight (peaked in intensity at $E{\sim}1.5eV$) is absorbed at band edges energies $1.4 \leq E \leq 1.9\,eV$. In this case the disorder is due to non-crystalline structure. In a-Si:H the disorder could be changed modifying the hydrogen content.

In semiconductors the width of the Urbach edge $E_0(X,T)$ can be written as [24]:

$$E_0(X,T) = K[\langle U^2\rangle_T + \langle U^2\rangle_X]\,, \tag{3.38}$$

where $\langle U^2\rangle_T$ is a thermal average of the square of the displacement U of the atoms from their equilibrium positions and $\langle U^2\rangle_X$ describes the structural (topological) disorder to mean-square deviation of atomic positions from a perfectly ordered configuration.

Sharpening of the band tails is desirable from the viewpoint of transport since it lowers trap densities as well as deep recombination center. This electrical improvement in the material results in a increase in E_{OPT} and significantly poorer optical absorption.

3.4 Determination of Absorption Coefficient

The optical properties of thin films are widely discussed by [25]. The figure 3.4 shows a homogeneous object that is irradiated with light under an angle of incidence θ. The incoming light I_0 could leave the sample in several directions after the interaction with this. In particular the light may either be:

a) transmitted through the sample in a well defined direction;
b) reflected from the sample;
c) scattered at the sample surface or in its volume;

d) absorbed at the sample surface or in its volume.

The transmittance *T* is defined as the ratio of the intensity of transmitted light I_T to the incoming light I_0 :

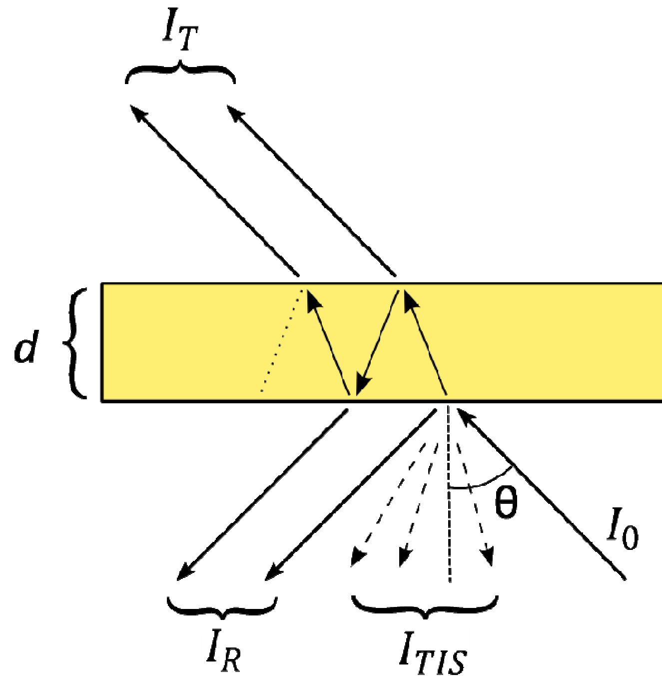

Figure 3.4: Distribution of light intensity incident on a sample with thickness d.

$$T = \frac{I_T}{I_0}. \tag{3.39}$$

The reflectance *R* is the ratio of the reflected intensity I_R to the incoming light I_0 :

$$R = \frac{I_R}{I_0}. \tag{3.40}$$

The expression (3.40) is correct if the RMS surface roughness is small compared to the wavelength of the light. If a surface is illuminated with a parallel beam of monochromatic light, the total reflected light may be divided into two components, one associated to the reflection, the other to the scattered radiation.

The Total Integrated Scatter (TIS) is the fraction of the total reflected intensity that is scattered out of the reflected beam. The TIS is related to the surface roughness R_{RMS} (2.3) by the following equation [26]:

$$TIS = R_{ss}\left[1 - e^{-\left(\frac{4\pi \cdot R_{RMS} \cdot cos\theta}{\lambda}\right)}\right], \quad (3.41)$$

where R_{ss} is the theoretical reflectance of a perfectly smooth surface of the same material, θ is the angle of incidence on the surface and λ is the wavelength of incident light. If the R_{RMS} is about few nanometers, the *TIS* is negligible for the visible and near UV-IR light.

Defining the absorbance *A* as the ratio of the absorbed intensity to the incoming one, the scattered light is neglected, the reflectance, transmittance and absorbance are related by the equation:

$$1 = R + T + A\,. \quad (3.42)$$

The relation (3.42) expresses the conservation of energy. The transmittance of the nc-SiO_xN_y films is a very important parameter. The efficiency of a solar cell is related to the optical losses associated to the layers that compound the cell. The equation (3.14) is equivalent to the following one:

$$T = 1 - R - A\,. \quad (3.42\ bis)$$

To increase the performance of the solar cell the nc-SiO_xN_y layers must have high transmittance *T*, therefore the reflectance *R* and in particular the absorbance *A* must be as low as possible.

Inside the sample the intensity of light at $d = 0$ is related to the intensity of light after traveling through the thickness *d* by the Beer-Lambert's law (3.25):

$$I(d) = I(0)e^{-\alpha(\omega)d}, \quad (3.25)$$

where $\alpha(\omega)$ is the light absorption coefficient of the sample tested. Using the equation (3.42) it is possible to replace $I(0)$ with $1 - R$ and $I(d)$ with *T* and the absorption coefficient becomes:

$$\alpha(\omega) = \frac{1}{d} ln\left(\frac{1 - R}{T}\right). \quad (3.43)$$

By the relation (3.43) we can experimentally estimate the optical absorption coefficient of a material. A thin film is usually deposited on a thick substrate, due to its mechanical support: this is typically a low absorption glass. In this case the values of T in (3.43) must be normalized with respect to the glass transmittance.

The main feature of thin-film is the presence of interference effects. If the thickness of the sample is very large compared to the wavelength, this effect is negligible and can be easily evaluated $\alpha(\omega)$. However, if the wavelengths are comparable with the thin-film thickness *d*, *T* and *R* are not interference free. In the strong absorption region the high light absorption destroys the interference effects and it is possible to use (3.36). It is also observed that the ratio $T/(1-R)$ is almost completely free from the interference effect as shown in fig. 3.5 [15]. This result suggests that $T/(1-R)$ is very effective for the determination of $\alpha(\omega)$ in wavelength regions where the interference effect exists.

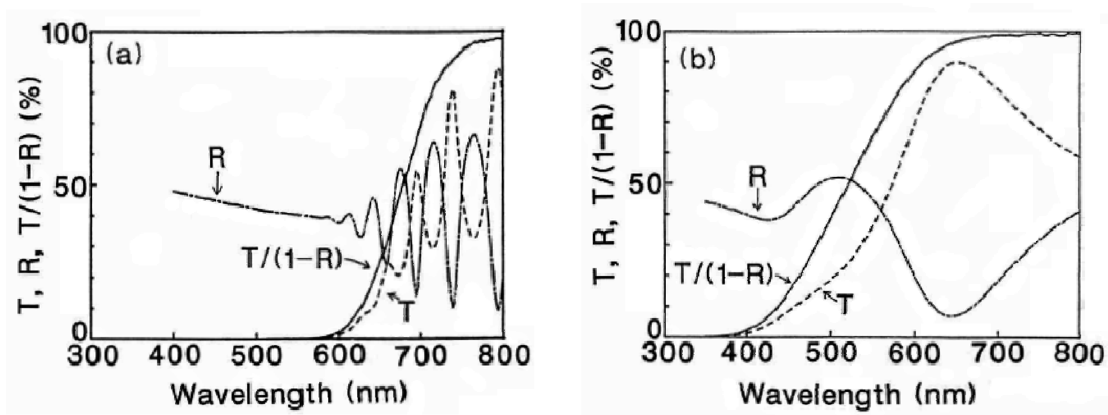

Figure 3.5: Experimental transmittance (T), Reflectance (R) and $T/(1-R)$ of (a) *an a-Si:H film with thickness = 1050 nm and* (b) *a-$Si_{1-x}C_x$:H film with thickness = 95 nm. Observing the figure it is clear that a maximum of T is associated to a minimum of R (and vice versa) from which it follows that the ratio $T/(1-R)$ is interference-free [15].*

4. Materials and Methods

In this chapter the sample growth process is illustrated and are reported the main growing features of all the samples studied in this work (tab. 4.1 - 4.5). The experimental setup and the main technical features of the equipments used to study the morphological and optical properties of the nc-$\mathrm{SiO_xN_y}$ films are also described.

4.1 PECVD Deposition and Annealing Treatment

The nc-$\mathrm{SiO_xN_y}$ films are grown using a commercial Plasma Enhanced Chemical Vapor Deposition (PECVD) unit (PlasmaLab 100 from Oxford Instruments) at the University of Konstanz (Germany) [27]. PECVD is a widely used technique which permits the deposition of thin and uniform layers on different types of substrates lying on a heated table as shown in fig. 4.1. The substrates used for the nc-$\mathrm{SiO_xN_y}$ film are an high-transmission glass or a crystalline boron-doped (100)-oriented silicon wafer. The first is essential to the study of the optical properties of nc-$\mathrm{SiO_xN_y}$:H films because the crystalline silicon does not transmit the visible light.

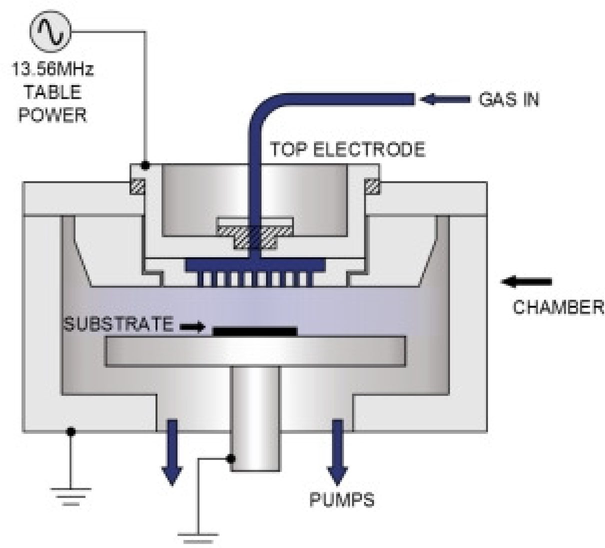

Fig. 4.1: Scheme of a PECVD PlasmaLab 100 reactor [28].

The material deposition takes place when the precursor gas is injected in the vacuum chamber. A 13.56 MHz Radio Frequency (RF) power is applied between the electrode plate and the heated table. At a given RF voltage there is usually a range of pressures for which plasma will occur.

The advantage of PECVD technique [29] with respect to standard Chemical Vapor Deposition (CVD) techniques is that the temperature of the substrate is completely controlled and it is an independent deposition parameter. Therefore, very low the deposition temperatures can be used, even room temperature. In a-Si:H films it is observed that H is incorporated more efficiently at low temperature ($T < 150°\mathrm{C}$) than at highest and this increases slightly the E_g of the a:Si:H [30]. At higher substrate temperature, less hydrogen is incorporated and the band gap is reduced.

The precursor gases used to grow the nc-$\mathrm{SiO_xN_y}$ films are silane ($\mathrm{SiH_4}$), hydrogen ($\mathrm{H_2}$) and nitrous oxide ($\mathrm{N_2O}$). The n- or p-doping of these films are obtained by adding phosphine ($\mathrm{PH_3}$) or dioborane ($\mathrm{B_2H_6}$) to the precursor gases. It In order to evaluate the relative concentration of the nitrous oxide, phosphine and dioborane in the precursors gases, dilution ratios are defined as follows:

$$R(N_2O) = \frac{[N_2O]}{[N_2O] + [SiH_4]}\ ; \tag{4.1}$$

$$R(PH_3) = \frac{[PH_3]}{[PH_3] + [SiH_4]}\ ; \tag{4.2}$$

$$R(B_2H_6) = \frac{[B_2H_6]}{[B_2H_6] + [SiH_4]}. \tag{4.3}$$

In a-Si:H films it is known that there some important effects of hydrogen dilution [29]:

1) as the hydrogen dilution increases, the deposition rate decreases;
2) the density of defects states is reduced because the hydrogen removes the strained weaker bounds that are in energetically unfavorable locations. Also the stability of the material against the light induced degradation effects is improved;
3) the hydrogen diffuses into the network, restructuring it and promoting a more stable structure. For this reasons, the formation of a silicon nano-crystalline structure is favored.

After the deposition, the samples were annealed at 800°C for some hours (typically 2, 3 or 6 hours). A great number of changes the microstructure of the films can occur during this thermal treatment. The most important of these is the recrystallization of

the amorphous films where the crystalline regions are surrounding by amorphous regions, as shown by the HRTEM images (fig.4.2).

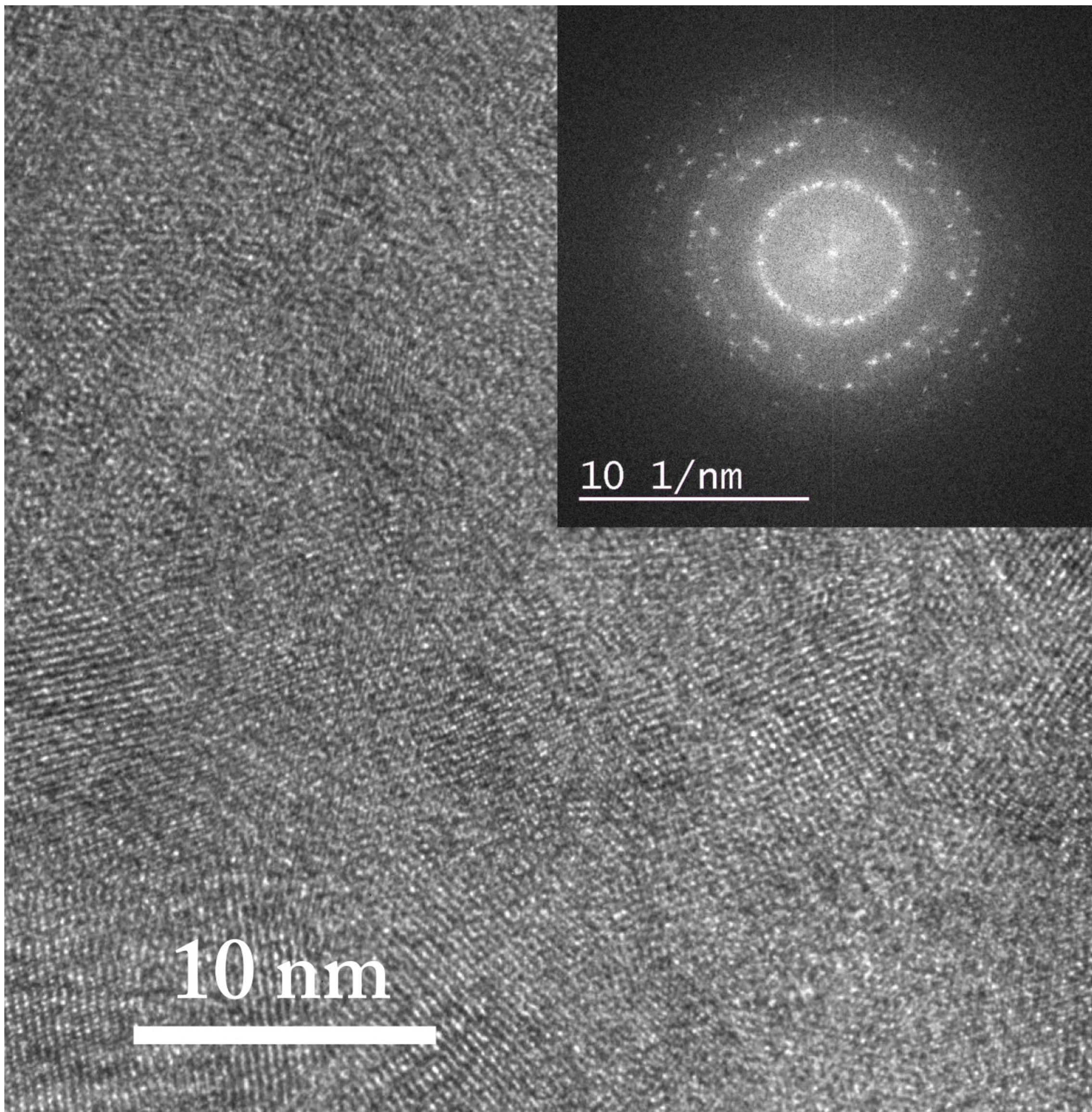

Fig. 4.2: HRTEM image of the sample SiD-3. In this image it is possible to observe the nano-crystalline structure of the nc- SiO_xN_y. *Image: A. Hammud.*

4.2 Samples

The samples characteristics are listed in table 4.1 – 4.5. In tab. 4.1 the main features of the samples grown on silicon wafers are summarized. The samples grown on high-transmission glasses are listed in the tab. 4.2 – 4.5. These samples have been analyzed

by optical transmission measurement (tab 4.2 -4.4) and both optical transmission and reflection measures (tab. 4.5).

Sample name	Annealing time (hours)	$R(N_2O)$ (%)	Thickness (nm)
SiA-0	2	9.09	417
SiB-0	0	16.7	437
SiB-2	2	16.7	437
SiB-6	6	16.7	437
SiC-3	3	23.1	540
SiD-3	3	28.6	510
SiE-3	3	47.4	(?)

Table 4.1: List of nc- SiO_xN_y *films grown on crystalline boron-doped (100)-oriented silicon wafers (* $R(B_2H_6)$ *= 2.34%).* $R(N_2O)$ *and* $R(B_2H_6)$ *are defined in eq. 4.1 and 4.3.*

Sample name	Annealing time (hours)	$R(N_2O)$ (%)	$R(PH_3)$ *(%)*	Thickness (nm)
GA-3	3	16.67	2.34	131
GA-6	6	16.67	2.34	131
GB-3	3	16.67	1.19	170
GB-6	6	16.67	1.19	170
GC-3	3	9.09	2.34	125
Gc-6	6	9.09	2.34	125

Table 4.2: nc- SiO_xN_y *films grown on high transmission glasses (RF power = medium).*

Sample name	Annealing time (hours)	RF power	Thickness (nm)
GD-3	3	low	135
GD-6	6	low	135
GE-3	3	high	190
GE-6	6	high	190
GF-3	3	medium	188
GF-6	6	medium	188
GG-3	3	medium	216
GG-6	6	medium	216

Table 4.3: nc- $\mathrm{SiO_xN_y}$ *films grown on high transmission glasses (*$R(N_2O)$ *= 28.6%,* $R(B_2H_6)$ *= 1.19%).*

Sample name	Annealing time (hours)	Thickness (nm)
GH-0	0	204
GH-3	3	204
GH-6	6	204

Table 4.4: Intrinsic nc- $\mathrm{SiO_xN_y}$ *films grown on high transmission glasses (*$R(N_2O)$ *= 9.09%).*

Sample name	Annealing time (hours)	$R(N_2O)$ (%)	Thickness (nm)
GI-0	0	9.09	209
GI-3	3	9.09	209
GI-6	6	9.09	209
GL-0	0	16.7	224
GL-3	3	16.7	224
GL-6	6	16.7	224
GM-0	0	23.1	270
GM-3	3	23.1	270
GM-6	6	23.1	270
GN-0	0	48.0	283
GN-3	3	48.0	283
GN-6	6	48.0	283

Table 4.5: nc- SiO_xN_y *films grown on high transmission glasses (*$R(B_2H_6)$ *= 2.34%).*

4.3 Atomic Force Microscopy and Image Processing

The Atomic Force Microscope (AFM) used in this work is a Solver P47H-Pro (fig.4.3) made by NT-MDT (*Molecular Devices and Tools for Nano Tecnology*) and controlled by the software "*NOVA*". The main feature of this instrument is the wide range of application and built-in techniques, but it requires a fair amount experience for proper use.

Figure 4.3: Solver P47H-Pro atomic force microscope [31].

An introduction to the atomic force microscopy methods applied in this thesis is reported in [32]. An AFM image is the result of the interaction between a sharp tip and sample surface. For the study of nc- SiO_xN_y films, the AFM was used in both semi-contact and contact mode. In contact mode the tip is in direct contact with the surface of the sample. In semi-contact mode the forced oscillations of the tip are exited near the resonance frequency of the cantilever and in the lower semi-oscillation the tip gets in contact with the sample surface (fig. 4.4). If z_0 is the distance covered by the tip from the equilibrium position until contact to the surface, the semi-contact mode is realized only when z_0 is smaller than the amplitude of cantilever oscillation. The amplitude variation is the feedback signal for the formation of a map. The semi-contact mode is more suitable for the morphological analysis because returns images of better quality than the contact mode. In addition to amplitude variation it is also possible to observe the phase shift between the driving signal of the piezoelectric vibrator and the stationary cantilever oscillation using the "phase contrast" acquisition mode. If the phase shift is >90°, an attractive interaction between the tip and the sample is established. If the phase shift is <90°, a repulsive interaction is predominant, the tip is damaged more quickly and the AFM images are typically of lower quality. Therefore morphological analyzes of nc- SiO_xN_y films were done in semi-contact mode, establishing an attractive interaction between the tip and the sample.

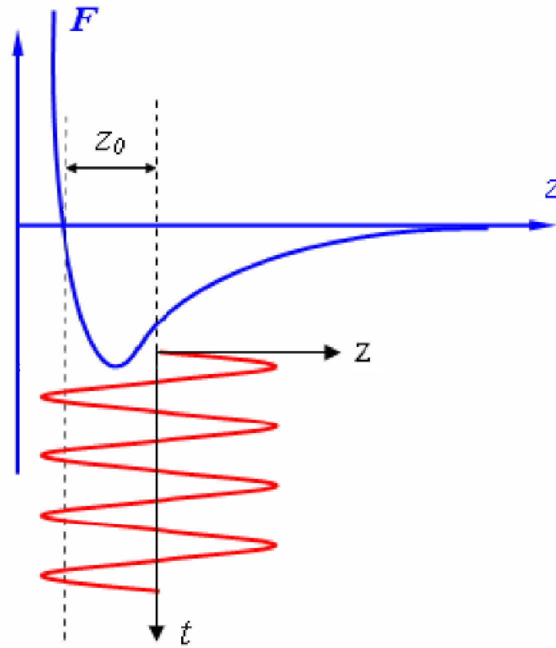

Figure 4.4: Total force acting on the tip F as function of the distance between the tip and the surface of the sample z (blue); oscillations of the tip z as function of time t (red) [32].

A proper choice of the probes is essential for obtaining good AFM images. For high resolution imaging, the most important parameter for an AFM probe is the curvature radius of the tip, which must be as small as possible to reduce tip-sample convolution effects. A thin tip can penetrate more easily than a bigger one deeper structures of a sample surface, thus the choice of the tip is subordinate primarily on the size of the details that we would reveal. As a general rule the dimension of the tip must be smaller than the smallest details that we want to observe.

The main features of the two different AFM probes used in this thesis are listed in table 4.6. The NSG10 are non-contact probes, with a curvature radius typically around 10 nm. For the study of nc-SiO_xN_y these probes can be used to obtain large field images, but they are unsuitable for high-magnification maps or for an accurate study of the statistical properties of the surfaces. The NSG10-DLC are super sharp Diamond-Like Carbon (DLC) probes with a curvature radius of about 1-3 nm. The DLC structures are controlled at Scanning Electron Microscope (SEM) by the producer after the growing process of the DLC structures on the standard tips(fig.4.4). The tips are selected only if the probes are longer than 20 nm or more. The NSG10-DLC extremely useful for obtaining high resolution images of objects with sizes of few nanometers. However, the high cost and the fragility of these tips make them a tool to be used only when the standard tips are not able to show the finest details of the surfaces.

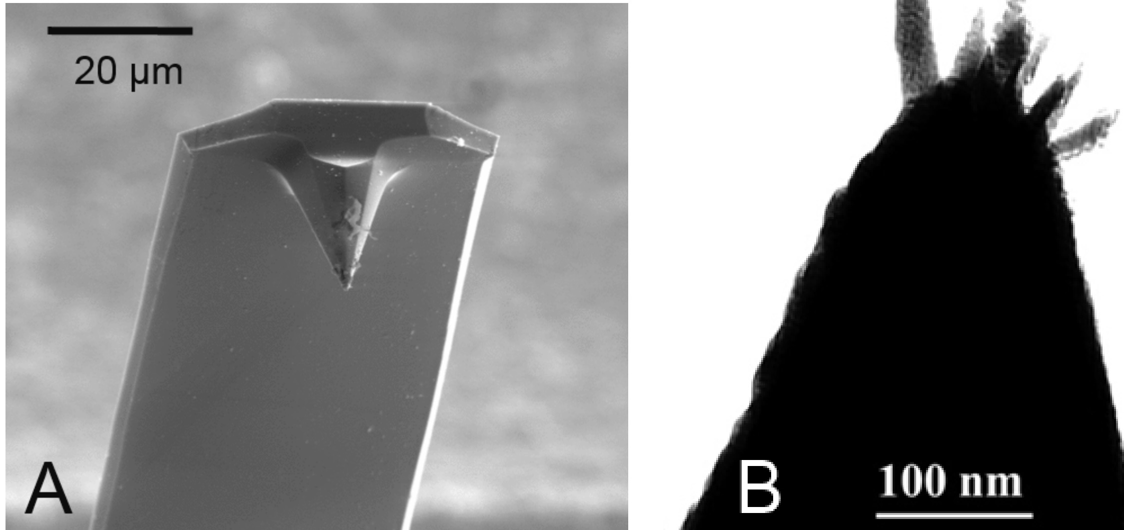

Figure 4.4: SEM image of a standard tip (A) the NSG10-DLC tip (B). It is possible to observe the diamond-like carbon (DLC) structures grown on a standard AFM tip. The high aspect ratio allows for obtaining high resolution maps [31].

Probe Series	NSG10	NSG10-DLC
Cantilever length (µm)	95±5	100±5
Cantilever width (µm)	30±3	35±3
Cantilever thickness (µm)	2.0	2.0
Curvature radius (nm)	10	1 - 3
Nominal resonant frequency (kHz)	240 [140-390]	255 [190-325]
Nominal force constant (N/m)	11.5 [5.5-22.5]	11.8 [3.1-37.6]

Table 4.6: Main features of the semi-contact mode probes used for the morphological characterization of nc-SiO_xN_y films.

The AFM images are processed by the freeware software "*Gwyddion*" (http://gwyddion.net). The data processing consists of three steps:

1. subtraction of a second order surface;
2. line averaging;
3. scars removing.

The surface images acquired by AFM show inclination and are superposition of the real topography and some surfaces of the second (and sometimes higher) order. This inclination can be the result of a tilted installation of the sample on the sample-holder, and/or non flatness of the sample, and/or non-linearity of the piezoelectric movement and temperature drift. In inclined image z varies over a large portion of the z-axis of a map, thus there are possible hiding small details. To overcome this inconvenience a second order surface is subtracts from all the AFM maps acquired (fig. 4.5).

Low-frequency noise affects the mean position of each line with respect to the adjacent lines. Moreover, the tip-sample distance could change during scanning, due to micro moments in elements of the scanner structure, or due to changes occurring on tip surface (for example, capture by the tip apex of a impurities or dust). This produces steps parallel to the direction of scanning on a AFM image. It is possible to remove all these steps applying the line averaging filter, as shown in fig. 4.6.

Another useful tool is the scars removing filter. Vibrations and abrupt changes of height generate scars on the AFM images. These artifacts are very difficult to correct.

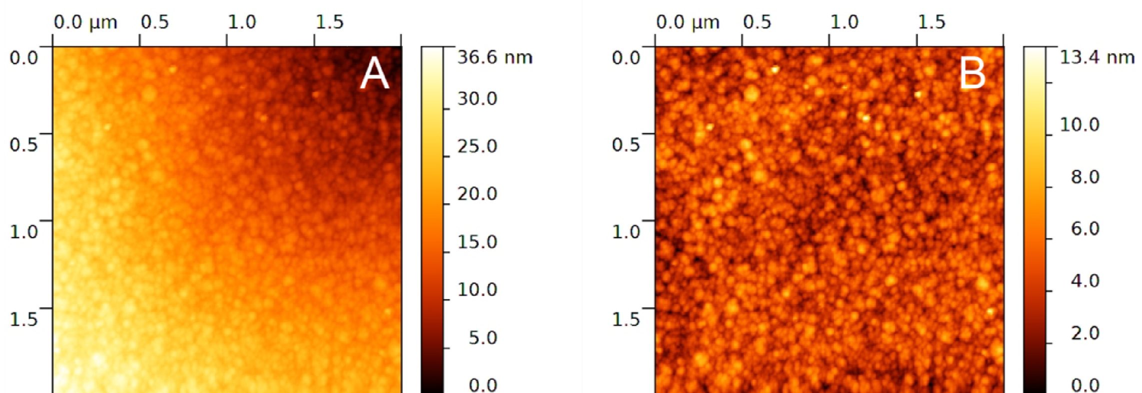

Figure 4.5: An AFM map (A); the same map after a subtraction of a second order surface (B).

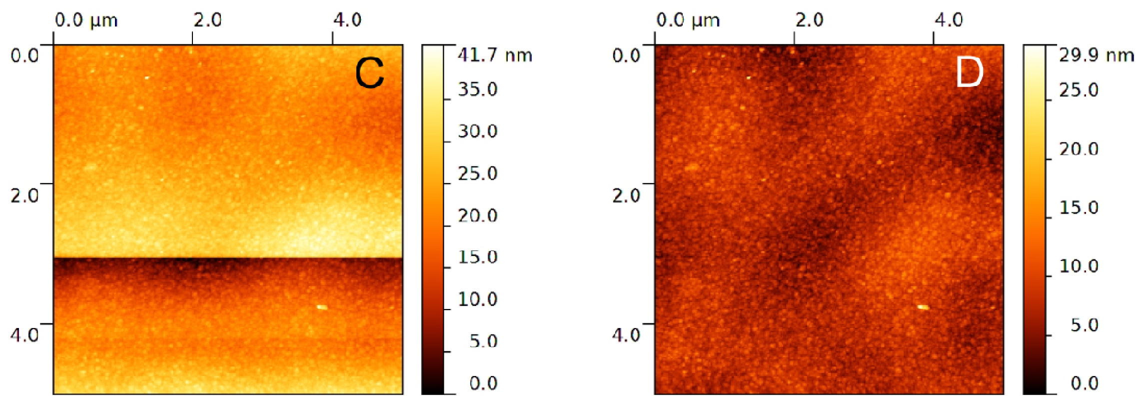

Figure 4.6: A map after a subtraction of a second order surface (C); the same map after line averaging (D).

4.4 Optical Spectroscopy

The optical characterization of nc-SiO_xN_y films grown on high-transmittance glass has been performed with the experimental setup shown in fig. 4.7.

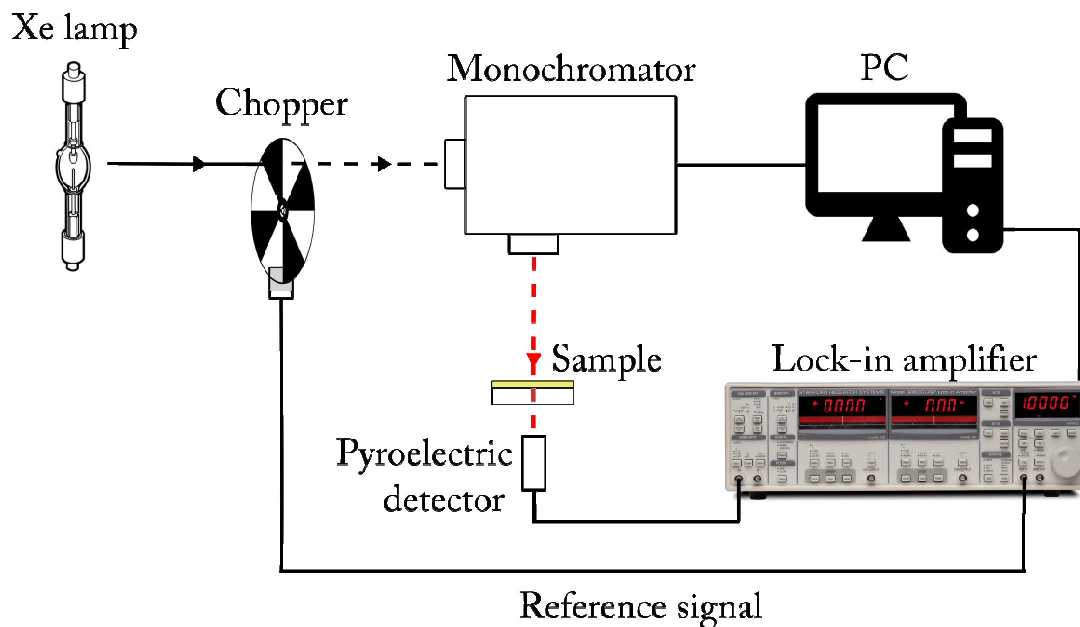

Figure 4.7: Scheme of the experimental setup for the optical characterization of the a-SiO_xN_y films. The optical configuration used for transmission measures is shown.

The equipments used are the following:

a) Xe lamp;
b) chopper (SCITEC 300CD);
c) monochromator SPEX500;
d) beam splitter (only to perform reflectance measures);
e) pyroelectric detector P2613-06 Hamamatsu;
f) lock-in amplifier SR830;
g) personal computer.

The Xe lamp is used as white light source. This lamp is characterized by a black body emission with the maximum emission in the blue region (≈470 nm). The chopper SCITEC 300CD is placed between the lamp and the monochromator and creates a beam of pulsed light. The chopping frequency is controlled by an independent power supply unity and is set at 30 Hz. The chopping frequency measured by an opto-switch is used for the reference of the lock-in amplifier. It is important that the chopping frequency doesn't change during the measures because the optical spectra depend on this value. The white pulsed light enters the monochromator SPEX500M which selects a bandwidth from the incoming spectrum. The optical configuration symmetric *Czerny-Turner* (fig. 4.8) allows to have an optical path of 0.5m: a larger one allows higher resolution. The blazing wave length of the diffraction grating used is 300 nm.

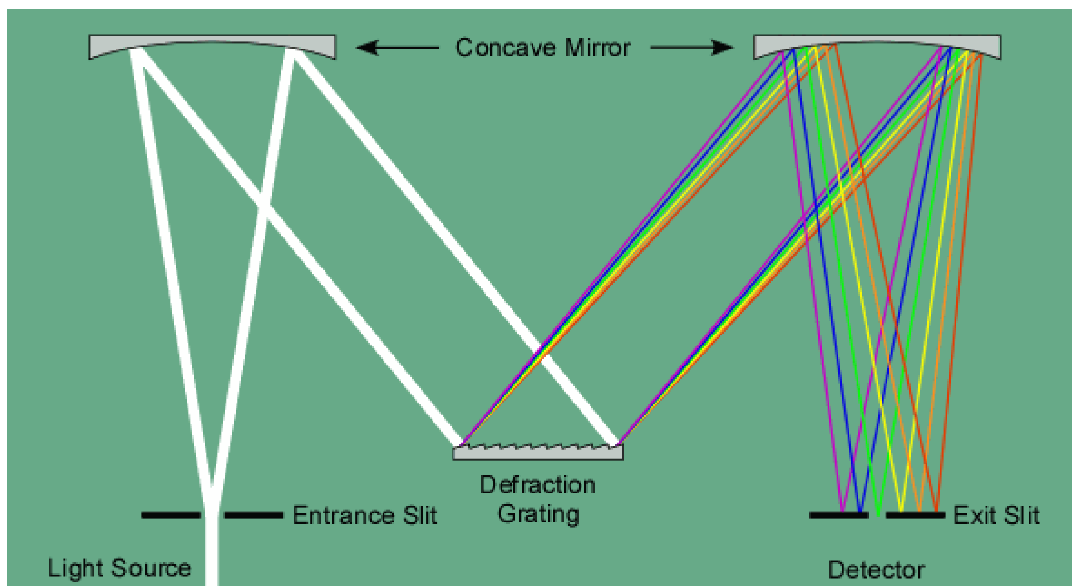

Figure 4.8: Optical configuration of a Czerny-Turner monochromator [33].

The most important technical features of the monochromator SPEX500M are the following:

Spectral range:	0 – 1500 nm
Linear dispersion:	1.6 nm / mm
Resolution:	0.02 nm
Width of the slits (adjustable):	0 – 3000 µm

The linear dispersion is very important because when the spectrometer is set at one particular wavelength the light that comes out from the exit slit is not a perfectly monochromatic one: the wavelength dispersion around the set value is related to the width of the slits. Because we set the slits width at 3 mm the light that comes out from the monochromator has a wavelength in the range of ±2.4 nm around the wavelength selected.

The pyroelectric detector used is the P2613-06 Hamamatsu (fig 4.9). A pyroelectric detector is a thermal type detector that operates at room temperature (fig. 4.8). The sensor detector is made by lead zirconium titanate (an intermetallic inorganic compound with chemical formula $Pb(Zr_xTi_{1-x})O_3$, also called PZT) having pyroelectric effects (fig. 4.10), a high electrical resistance and a low noise Field-Effect Transistor (FET), all hermetically sealed in a metal package to protect them against external noise.

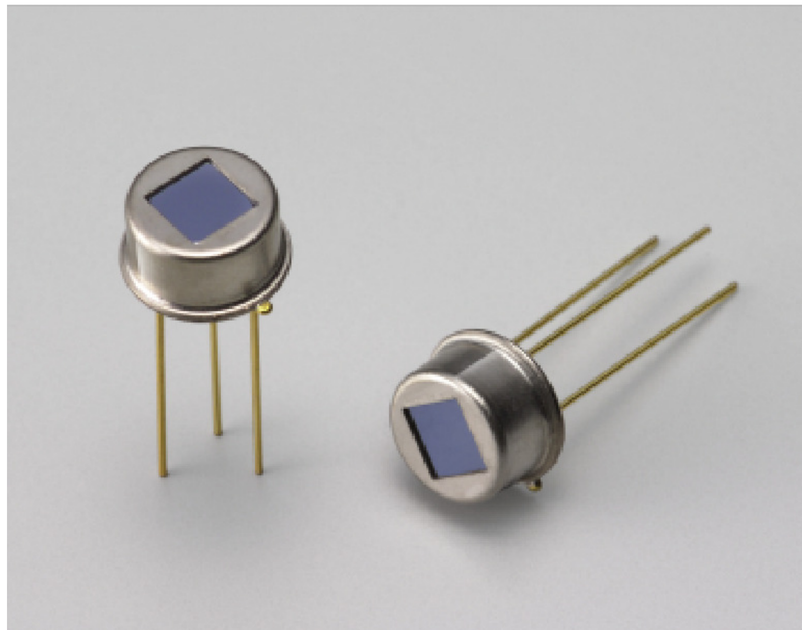

Figure 4.9: The pyroelectric P2613-06 made by Hamamatsu [34].

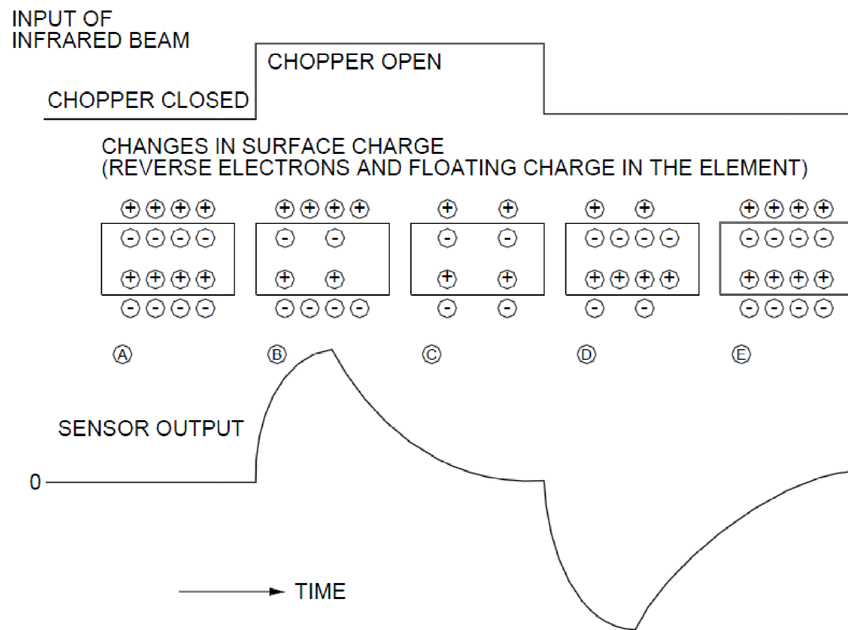

Figure 4.10: Schematic presentation of pyroelectric effects. (A) *In the dark state the PZT is spontaneously polarized and this electrical charge is neutralized by the ions present in the air.* (B) *When light enters the element and is absorbed, the temperature increases results in a change of the spontaneous polarization state, which is observed as a voltage change.* (C) *The new state of polarization vanishes due to charges in the ambient atmosphere after a short time.* (D) *In the dark condition the PZT returns in the original polarization state and is still observed a voltage change.* (E) *Other ions are placed at the surface of the PZT and the situation is similar to the initial* (A). *[34].*

There are two methods for extracting surface charge: using voltage or using current. Ordinarily, voltage output pyroelectric detectors are used. The voltage type offers a simple circuit configuration and less noise, and it has a sensitivity peak at a relatively low frequency. The current type features high gain and constant sensitivity ranging from low to high. The frequency limit is determinated by the constant of the amplifier, so the frequency response can be improved by adjusting the circuit configuration of the amplifier.

The size of the PZT element size must be chosen to match the size of the beam being detected.

The photo sensitivity (or responsivity) R is the output voltage per watt of incident energy when noise is neglected:

$$R = \frac{S}{PA}, \quad \left[\frac{\mathrm{V}}{\mathrm{W}}\right] \tag{4.1}$$

where S is the signal output [V], P the incident energy [W/cm^2] and A the detector active area [cm^2].

The Noise Equivalent Power (NEP) is the intensity of incident light equal to the intrinsic noise level of a detector. In other words, this is the quantity of incident light when the signal-to-noise ratio (*S/N*) is 1. If Δf is the noise bandwidth [Hz], *NEP* is defined as follows:

$$NEP = \frac{PA}{S/N \cdot \sqrt{\Delta f}} \, . \quad [\mathrm{W/Hz^{1/2}}] \tag{4.2}$$

In datasheets *NEP* is indicated as *NEP*$(T, f, \Delta f)$, where *T* [K] is the temperature of the black-body source and *f* is the signal frequency modulation [Hz].

The photo sensitivity *R* per unit active area of detector is called detectivity. The detectivity *D** allows us to compare more easily the characteristics of different detectors. In many detectors *NEP* is proportional to the square root of the detector active area, so *D** is defined by the following equation:

$$D^* = \frac{S/N \cdot \sqrt{\Delta f}}{P\sqrt{A}} = \frac{\sqrt{A}}{NEP} . \quad [\mathrm{cm \cdot Hz^{1/2}/W}] \tag{4.3}$$

A larger value of *D** indicates a better detector element.

The main features of the pyroelectric detector P2613-06 Hamamatsu previously described are the following:

Window material:	Sapphire
Active area:	2 mm diameter
Spectral response range:	0.15 – 5.5 µm
Sensitivity:	1500 V/W
Noise max.:	15 $\mu V/Hz^{1/2}$
D* (500,1,1):	$2 \cdot 10^8$ cm· $Hz^{1/2}$/W
NEP (500,1,1):	$1 \cdot 10^{-9}$ W/ $Hz^{1/2}$
Rise time 0 to 63%:	100 ms
Temp. coefficient of sensitivity max.:	0.2 %/°C
Supply voltage:	3 to 15 V
Offset voltage R_L=22 kΩ:	0.2 to 1.0 V
Operating temperature range:	-20 to +60 °C
Storage temperature range:	-30 to +85 °C

The pyroelectric detector generates a small AC signal with the same frequency measured by the opto-switch when the beam of pulsed light arrives on the PZT element. Accurate measurements cannot be made if the small AC signal is obscured by a noise sources many thousands of time larger. This problem is overcome using the SR830 Digital Signal Processor (DSP) Lock-in amplifier, an instrument able to detect and measure very small AC signals. A complete guide on the functioning of this instrument is at the manufacturer's site [35].

Lock-in amplifiers use a technique known as "phase sensitive detection" to single out the component of the signal at a specific reference frequency and phase. Noise signals at frequencies other than the reference frequency are rejected and do not affect the measurement.

Lock-in measurements require a frequency reference ω_r. The AC signal that we want to detect is:

$$V_{sig} sin(\omega_r t + \theta_{sig}) , \quad (4.4)$$

where V_{sig} is the signal amplitude and θ_{sig} a phase. Using the reference signal from the opto-switch (like a sine wave or a TTL logic signal), the SR830 generates its own a sine wave that becomes the lock-in reference signal:

$$V_L sin(\omega_L t + \theta_{ref}) . \quad (4.5)$$

The SR830 amplifies the AC signal (eq. 4.4) and then multiplies it by the lock-in reference signal (4.9). The output of the Phase-Sensitive Detector (PSD) is therefore the product of two sine waves:

$$\begin{aligned} V_{PSD} &= V_{sig}\, V_L sin(\omega_r t + \theta_{sig}) sin(\omega_L t + \theta_{ref}) = \\ &= 0.5 \cdot V_{sig}\, V_L cos([\omega_r - \omega_L]t + \theta_{sig} - \theta_{ref}) - \\ &+0.5 \cdot V_{sig}\, V_L cos([\omega_r + \omega_L]t + \theta_{sig} + \theta_{ref}) . \end{aligned} \quad (4.6)$$

The PSD output consists of two AC signals one at a difference frequency which is the difference $(\omega_r - \omega_L)$ and one at a frequency which is the sum $(\omega_r + \omega_L)$.

If ω_r equals ω_L, the first term in equation (4.10) will be a DC signal and the second an AC signal. Therefore the PSD output V_{PSD} goes through a low pass filter and all the AC signals are removed. The filtered PSD output will be:

$$V_{PSD} = \frac{1}{2} V_{sig}\, V_L cos(\theta_{sig} - \theta_{ref}) . \quad (4.7)$$

The equation (4.7) is a DC signal proportional to the signal amplitude V_{sig}.

If the two “notch filters” are switched on, it is clear that it is impossible to amplify the frequencies 50/60 Hz and 100/120 Hz. This is very useful to avoid interference with the grid frequency.

5. Experimental Results

In this chapter the experimental results obtained are illustrated. In the first part the method adopted for the morphological characterization of the nc-$\mathrm{SiO_xN_y}$ films is described. In particular, the evolution of the grain size and the cluster structure with respect to the deposition parameters is studied. In the second part of the chapter the optical spectroscopy experimental results are discussed.

5.1 Measurement of RMS Roughness at Different Magnifications

The first step in the characterization of nc-$\mathrm{SiO_xN_y}$ surfaces is an appropriate choice of the magnification at which the statistical analysis is done. The sample SiB-2 2h ($R(N_2O)$ = 16.7% and $R(B_2H_6)$= 2.34%) is mapped at different magnifications as shown in tab. 5.1. The AFM maps (fig. 5.1 a, b), made at 256x256 pixels, reveal that 5x5 μm^2 or 4x4 μm^2 map emphasizes macroscopic features of the surface but fail to reveal the nc-$\mathrm{SiO_xN_y}$ grain details. In these cases the resolution is insufficient for the successful outcome of a statistical analysis on grains. The 1x1 μm^2 or 0.5x0.5 μm^2 maps (fig. 5.1 e, f) reveal better the local surface features.

Map size (μm^2)	***R**** **(nm)**
0.5x0.5	1.5±0.2
1x1	1.5±0.2
2x2	1.5±0.2
3x3	1.6±0.2
4x4	1.8±0.3
5x5	3.2±1.0

Table 5.1: RMS roughness R (2.4) of the sample SiB-2 ($R(N_2O)$ = 16.7% and $R(B_2H_6) = 2.34\%$) as a function of the map size. Tip used: NSG10-DLC.*

a)

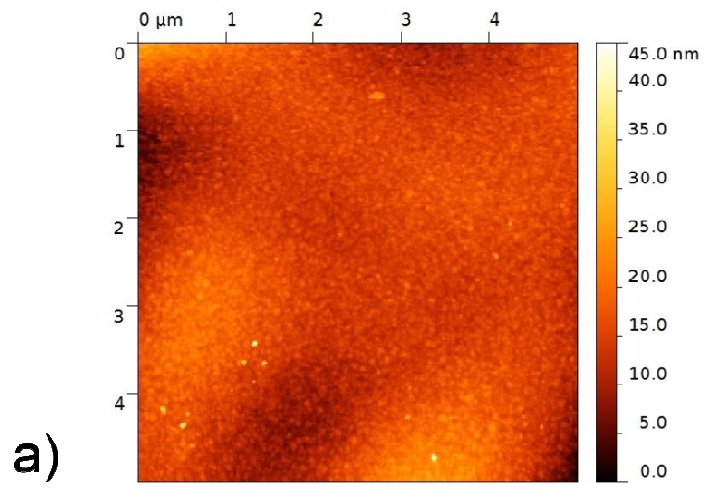

b)

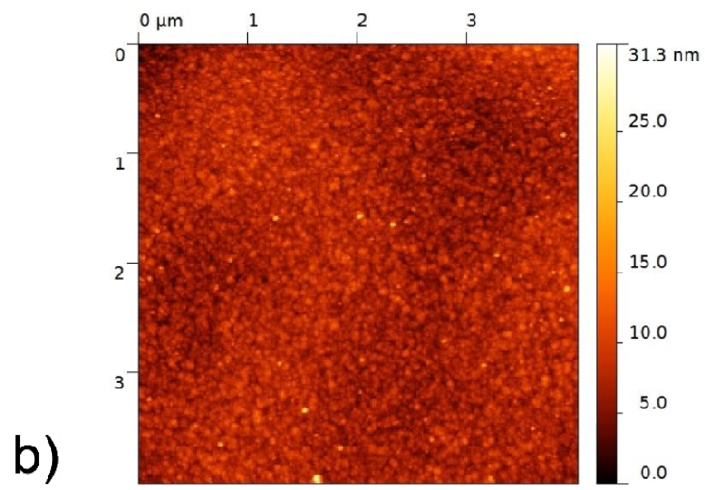

c)

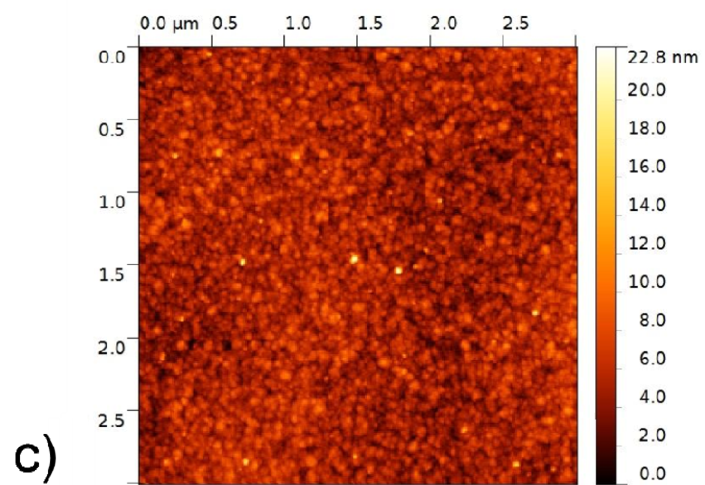

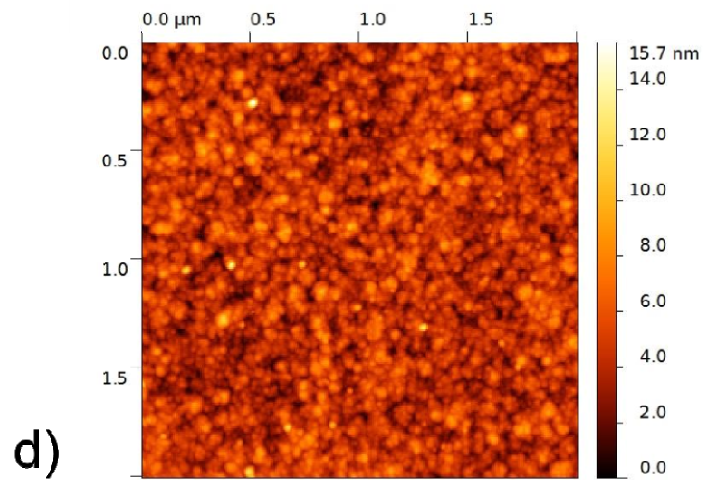

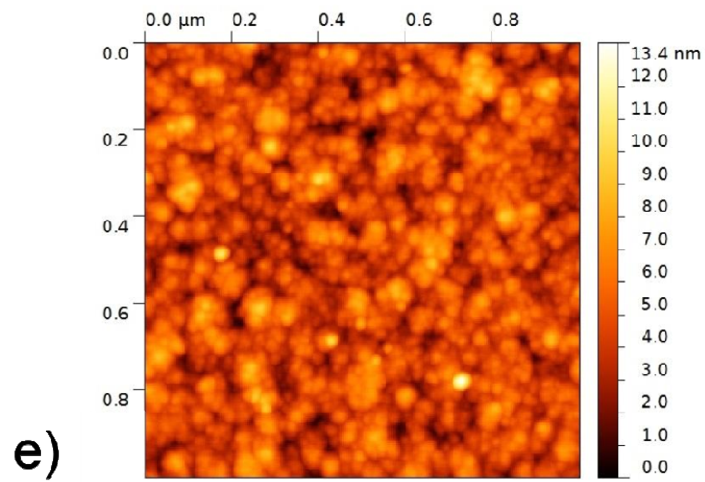

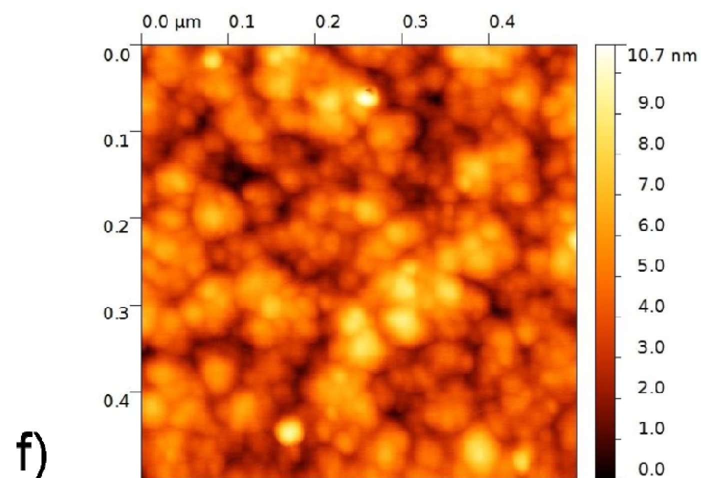

Figure 5.2: The surface of the sample SiB-2 ($R(N_2O)$ = 16.7% and $R(B_2H_6) = 2.34\%$) at different magnifications. Tip used: NSG10-DLC.

It is observed that the value of RMS roughness $R*$ defined in equation (2.4) is constant for 0.5x0.5, 1x1 and 2x2 μm^2 maps (tab. 5.1, fig. 5.1). Because the RMS roughness depends on the height distribution associated to the map, the 0.5x0.5 μm^2 or 1x1 μm^2 maps are more sensitive to the grains and clusters structures than to the macroscopic features of the surface on which they grow. If the map size is smaller than the wavelength that characterizes the macroscopic surface, the RMS roughness describes mainly the grains. The magnification at which it is possible to perform the statistical analysis can be identified observing for which map the grains are clearly visible. Furthermore R* should remain constant with respect to small changes of the map size. Since we are interested in the grain size and the cluster structure, the 0.5x0.5 μm^2 maps have been chosen for the statistical analysis.

The image processing was done by the software *Gwyddion* as described in chapter 4.3.

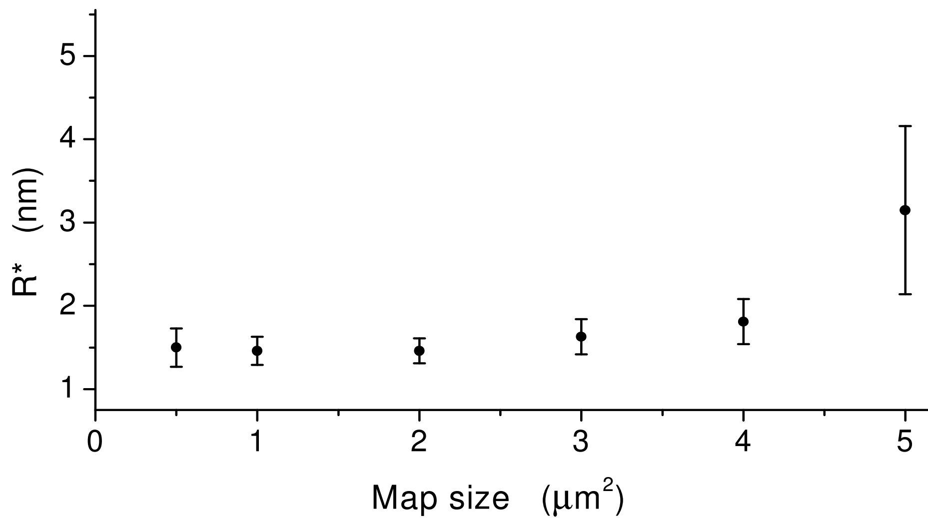

Figure 5.1: RMS roughness R (2.4) of the sample SiB-2 ($R(N_2O)$ = 16.7% and $R(B_2H_6) = 2.34\%$) as a function of the map size*. The value or *R* decreases with the map size* until *reaching a threshold value. Tip used: NSG10-DLC.*

5.2 Annealing Effect on the Surface Morphology

The SiO_xN_y films could be subjected to an annealing treatment after the deposition as described in tab. 4.1. The principal difference between annealed and as-deposed films is the fraction of nano-crystalline phase. After the deposition, the heat treatment decreases the amorphous phase and the HRTEM images (see chapter 4.1) show the

formation of nano-crystals. By acquiring some maps at different annealing times it is possible to reconstruct the dynamics of changes occurring on the surface.

The samples studied are the SiB-0, SiB-2 and SiB-6 ($R(N_2O)$ = 16.7% and $R(B_2H_6)$ = 2.34%). The surfaces of these samples are observed with DLC tips and for each sample some 0.5x0.5 μm^2 maps are acquired at different surface positions. A high number of maps improves the statistics on the grains, but this is not always possible, from one side because of the high cost of the NSG10-DLC tips, on the other hand because the tip degradation limited the number of well resolved map that can be acquired with each tip. For each of these samples the three best frames are selected and they are used to perform the surface statistical analysis. It is very important to select only the frames without artifacts because the numerical results of the statistical quantities studied could change.

Figure 5.3 and 5.4 shows 2D and 3D AFM maps of nc-$\mathrm{SiO_xN_y}$ films for different annealing conditions. The maps reveal that the features of the nc-$\mathrm{SiO_xN_y}$:H surfaces change with increasing the annealing time. In the as-deposited sample the grains are randomly spread on the surface and only small groups of them form little clusters. In the two hours annealed samples the clusterization is more evident and a great number of grains form larger clusters. In 6 hours annealed samples the clusterization is clearly evident and involves more grains; some clusters merge together forming sorts of islands with well-defined boundaries. All these effects are more evident in the 2D representation than in the 3D images.

There are three different way to calculate the RMS roughness with *Gwyddion*:

1. using the definition of RMS roughness *R* (eq. 2.3) calculated over the entire map;
2. applying the definition of RMS roughness R^* (eq. 2.5) averaged over scan lines;
3. using the properties of the HHCF function (eq. 2.20).

The RMS roughness has been obtained using methods 1. – 3. and the results will be compared. The procedure used to calculate the RMS roughness values is described below. With *Gwyddion* it is possible to export the HHCF curve associated to an AFM map as a text file. Data are analyzed using the software *OriginPro 8*. Each HHCF curve demonstrates an oscillatory behavior, as depicted in fig. 5.5. These oscillations are quite random and the oscillation amplitude is significantly reduced after further averaging of many HHCFs. As illustrated by Zhao et al. this feature does not represent a true statistical characteristic of the surface [9]. These random oscillations and fluctuations in each HHCF curve are associated to the finite data points and sampling size. For self-affine surfaces these behaviors occur because the number of sampled data points in the maps is not sufficient to describe the properties of the whole surface. These oscillations would diminish for a sufficiently large number of averaged curves: for

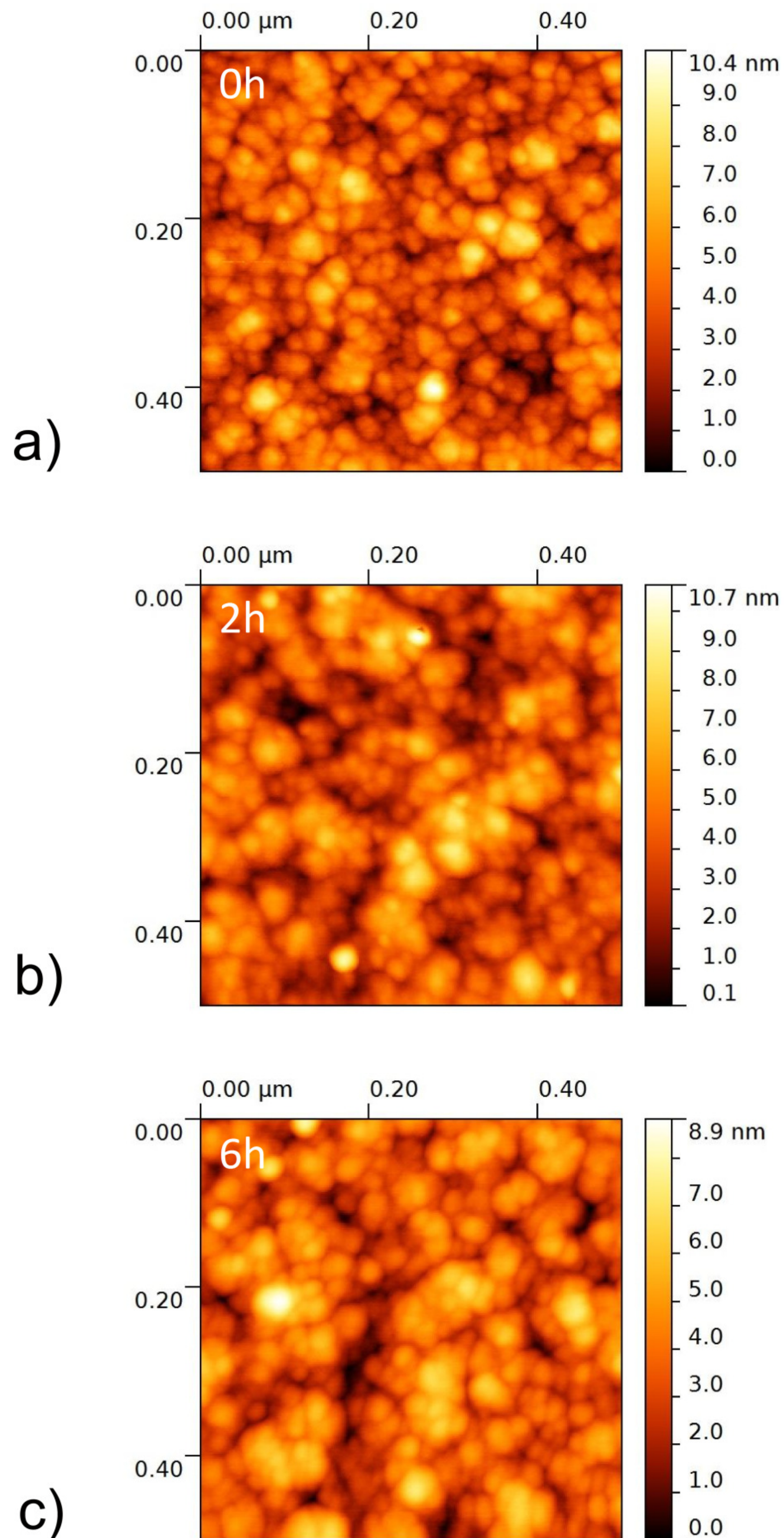

Figure 5.3: The images of the samples a) SiB-0, b) SiB-2 and c) SiB-6 *($R(N_2O)$* = 16.7% and $R(B_2H_6)$ = 2.34%*). Tip used: NSG10-DLC.*

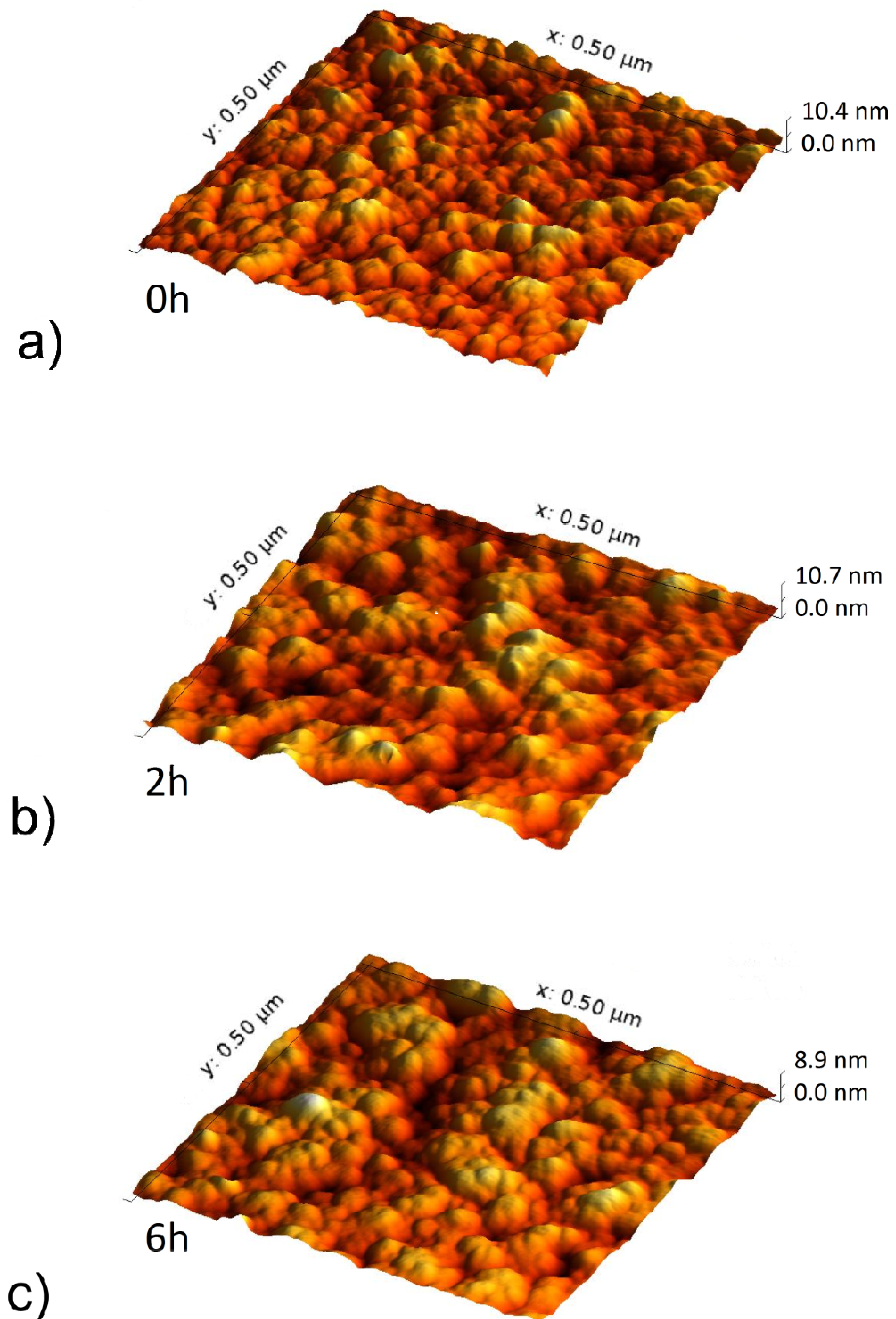

Figure 5.4: 3D view of the samples a) SiB-0, b) SiB-2 and c) SiB-6 *($R(N_2O)$* = 16.7% and $R(B_2H_6)$ = 2.34%. *The maps are the 3D version than those of the previous figure 5.3. The scale along the z-axis is magnified four times. Tip used: NSG10-DLC.*

this reasons, the average HHCF is calculated for each sample and it is possible to determine the values R, α and ξ using the equation (2.20).Another solution to diminish these oscillations is to acquire larger maps with higher resolution. In this case it has been preferred to acquire several 0.5x0.5 μm^2 maps to preserve the resolution of a single map.

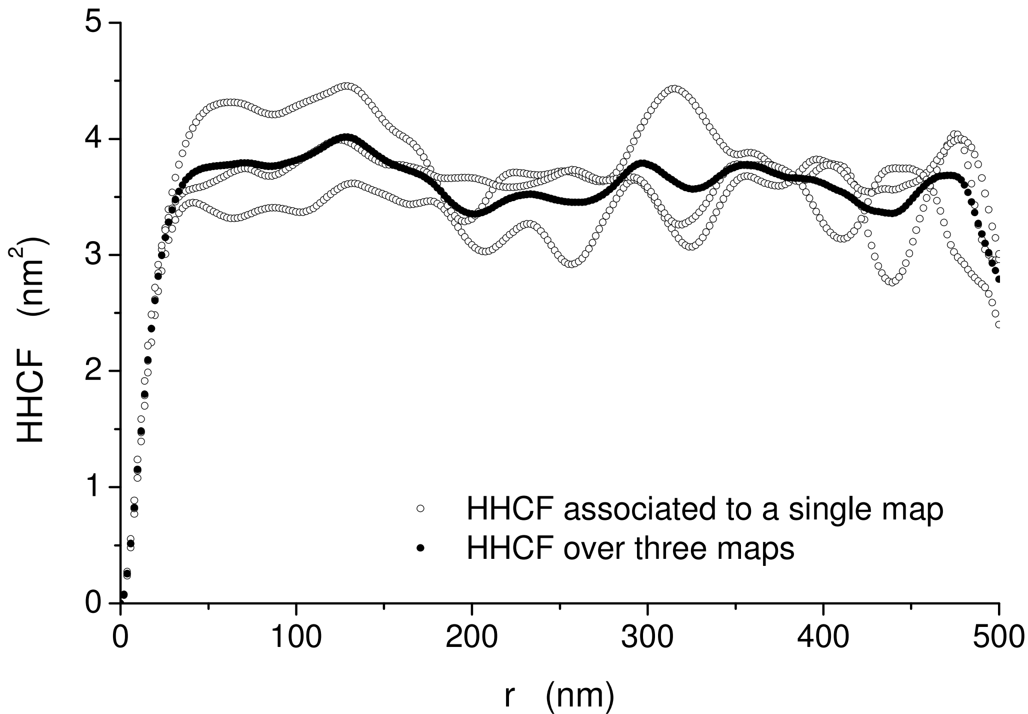

Figure 5.5: HHCF curves calculated for the sample SiB-0 ($R(N_2O)$ = 16.7% and $R(B_2H_6)$ = 2.34%). Tip used: NSG10-DLC.

The RMS roughness obtained by these three methods are consistent, within the errors (tab. 5.2). It is worth noting that errors associated to these three ways to calculate the same physical quantity are not comparable: the errors reported are the statistical ones. From the results it appears that the RMS roughness slightly increases after the first annealing hours, and the decreases.

From the average HHCF it is possible to calculate the roughness exponent α and the lateral correlation length ξ, as defined by equation (2.20). The roughness exponent α increases after the thermal treatment: this is easy to understand considering the acquired maps. The formation of clusters is observed with increasing annealing time (fig. 5.3), and the surface appears locally less wiggly. The present results well compare with the ones obtained by Zhao et al. on a-Si:H ($\alpha \approx 1$) [9, 36].

The annealing effects on grains are analyzed with *Gwyddion* studying the Mean Grain Size (MGS) calculated with the watershed method. The parameters used for this analysis are:

1. grain location:
   a. number of steps 1;
   b. drop size 10%;
   c. threshold 2 px^2;
2. segmentation:
   a. number of steps 100;
   b. drop size: 10%.

A correct choice of these parameters is essential for the success of the watershed method. However, observing the "watershed mask" it is clear that there are always some cases of incorrect grains identification (fig. 5.6). In particular two o more grains could be recognized as a single grain or vice versa. Finally, a cut is applied to remove the noise at low grain size values: the optimal threshold values identified is 2 px^2.

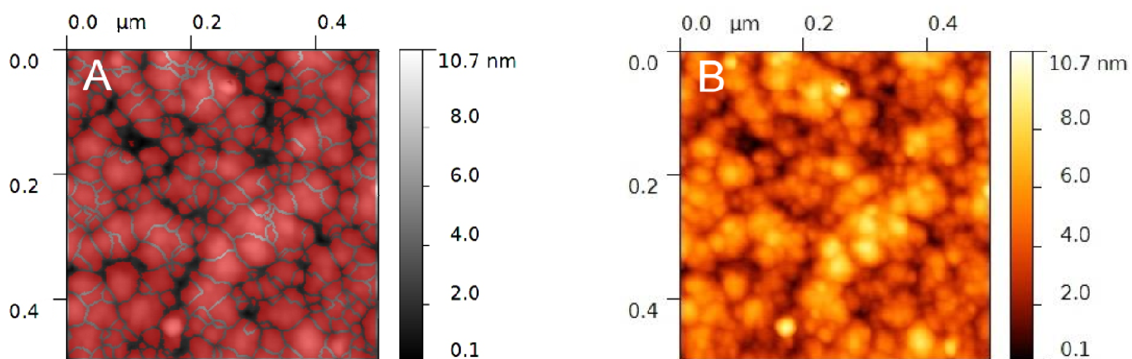

Figure 5.6: Watershed mask (A) over an AFM map (B) of the sample SiB-2. Tip used: NSG10-DLC.

In conclusion the watershed method presents some issues about the recognition of the grains. To understand how much this problem is significant, the diameter of one hundred grains is directly measured for three maps with different annealing times. The results for as-deposited, 3 and 6 annealing hours are respectively: 20±4, 24±6 and 24±7nm. These demonstrate that the watershed method gives a reliable estimate of the MGS.

It is possible to compare the MGS with the lateral correlation length ξ: these values show the same trend (fig. 5.7). Because the MGS is a measure of the grain size, it is considered that ξ should be associated to the grain size.

All the results obtained for the samples *SiB-0, SiB-2 and SiB-3* are summarized in tab. 5.2.

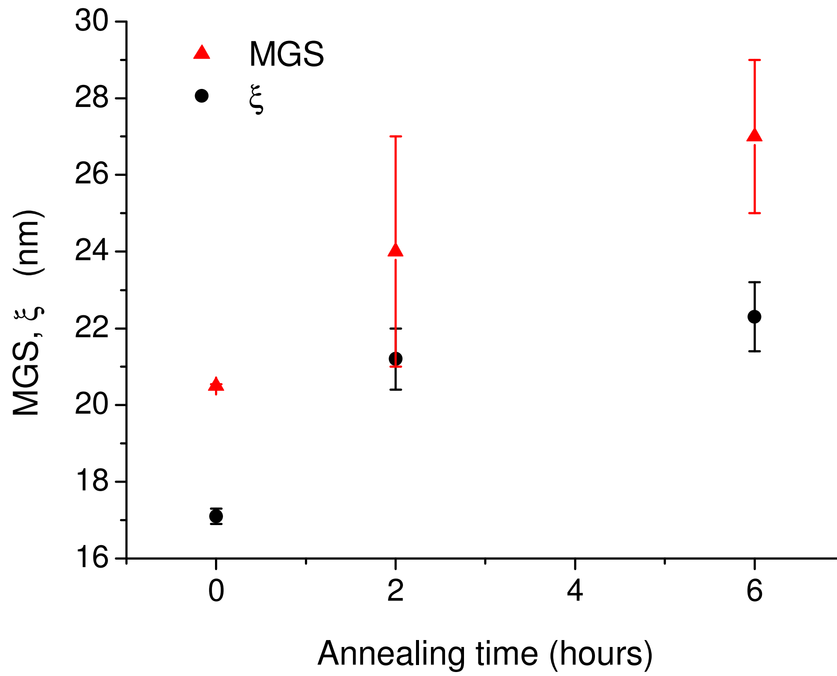

Figure 5.7: MGS and ξ as function of the annealing time for the samples SiB-0, SiB-2 and SiB-6 ($R(N_2O)$ = 16.7% and $R(B_2H_6)$ = 2.34%). Tip used: NSG10-DLC.

Sample	**SiB-0**	**SiB-0**	**SiB-0**
R (nm)	1.3±0.1	1.4±0.1	1.3±0.1
R* (nm)	1.3±0.1	1.4±0.1	1.3±0.1
R (HHCF) (nm)	1.35±0.01	1.36±0.01	1.26±0.01
α	0.89±0.01	0.94±0.04	0.94±0.03
ξ (nm)	17.1±0.2	21.2±0.8	22.3±0.9
MGS (nm)	20.5±0.5	24±3	27±2

Table 5.2: The analysis of the AFM maps provides some statistical quantities associated to the growth of the samples: the root mean square roughness, the roughness exponent α, the correlation length ξ and the Mean Grain Size MGS. Tip used: NSG10-DLC.

5.3 Changes in Surface Morphology with Increasing R(N_2O)

The nc- SiO_xN_y films surfaces grown with different nitrogen dioxide content ($R(N_2O)$ = 9.09%, 16.7%, 23.1%, 28.6%, 47.4%) are studied fixing the annealing time to 2 or 3 hours and $R(B_2H_6)$ to 2.34% (tab. 4.1). The exact oxygen and nitrogen content of the samples is not known, but it depends on the proportions in which the gases are present in the plasma during the growth phase as shown by SIMS measurements performed by Brinkmann et al. [27]. The effect of $R(N_2O)$ on the surface morphology is studied selecting 3 through 5 best maps for each sample. The observation of the AFM maps reveals changes in the surface morphology (fig. 5.8, 5.9). The clustering is evident in each sample, but the grain dimensions are different and increase with $R(N_2O)$.

All the statistical quantities that characterize the surface are listed in tab. (5.3).

$\boldsymbol{R(N_2O)}$	**9.09%**	**16.7%**	**23.1%**	**28.6%**	**47.4%**
R (nm)	1.3±0.1	1.4±0.1	1.4±0.1	1.4±0.1	1.6±0.1
R* (nm)	1.4±0.1	1.4±0.1	1.3±0.1	1.4±0.1	1.6±0.2
R (HHCF) (nm)	1.49±0.01	1.36±0.01	1.31±0.01	1.41±0.01	1.59±0.01
α	0.84±0.01	0.94±0.04	0.92±0.01	0.86±0.02	0.90±0.02
ξ (nm)	20.0±0.3	21.2±0.8	23.9±0.5	23.5±0.6	27.9±0.1
MGS (nm)	16±1	24±3	25±1	19±2	26.6±0.3

Table 5.3: Statistical quantities associated to the measured surfaces for different $R(N_2O)$. Tip used: NSG10-DLC.

The exponent α appears to be independent from $R(N_2O)$. However, we can observe that the samples with the $R(N_2O)$ = 9.09 and 28.6% are characterized by a lower roughness exponent α. The interpretation of the roughness is instead very difficult and there is not a particular trend with changing $R(N_2O)$. It is worth noting that for all the samples the roughness calculated by the three different methods results consistent within the errors.

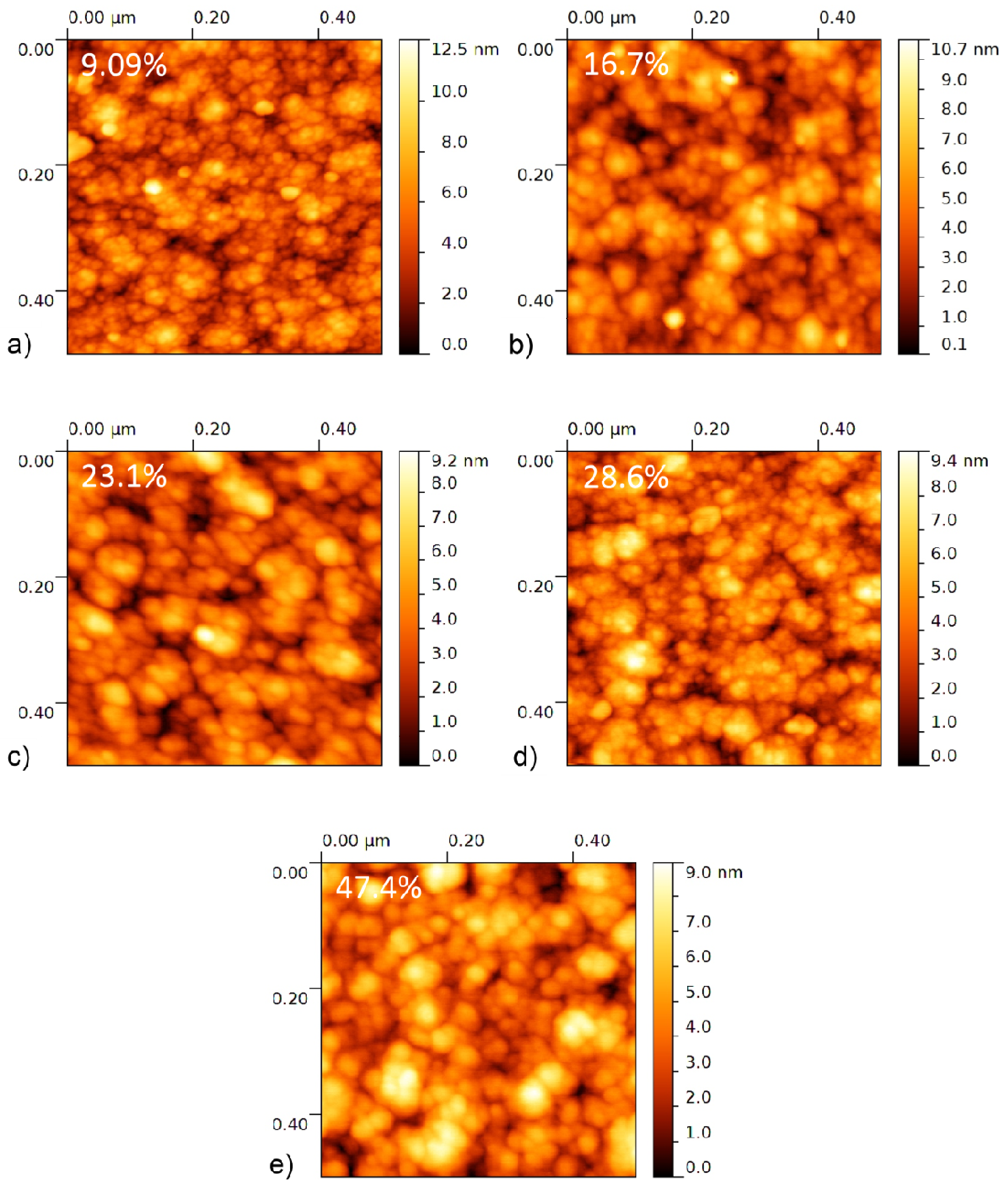

Figure 5.8: AFM images of the samples with different $R(N_2O)$ content: 9.09% a), 16.7% b), 23.1% c), 28.6% d), 47.4% e). Tip used: NSG10-DLC.

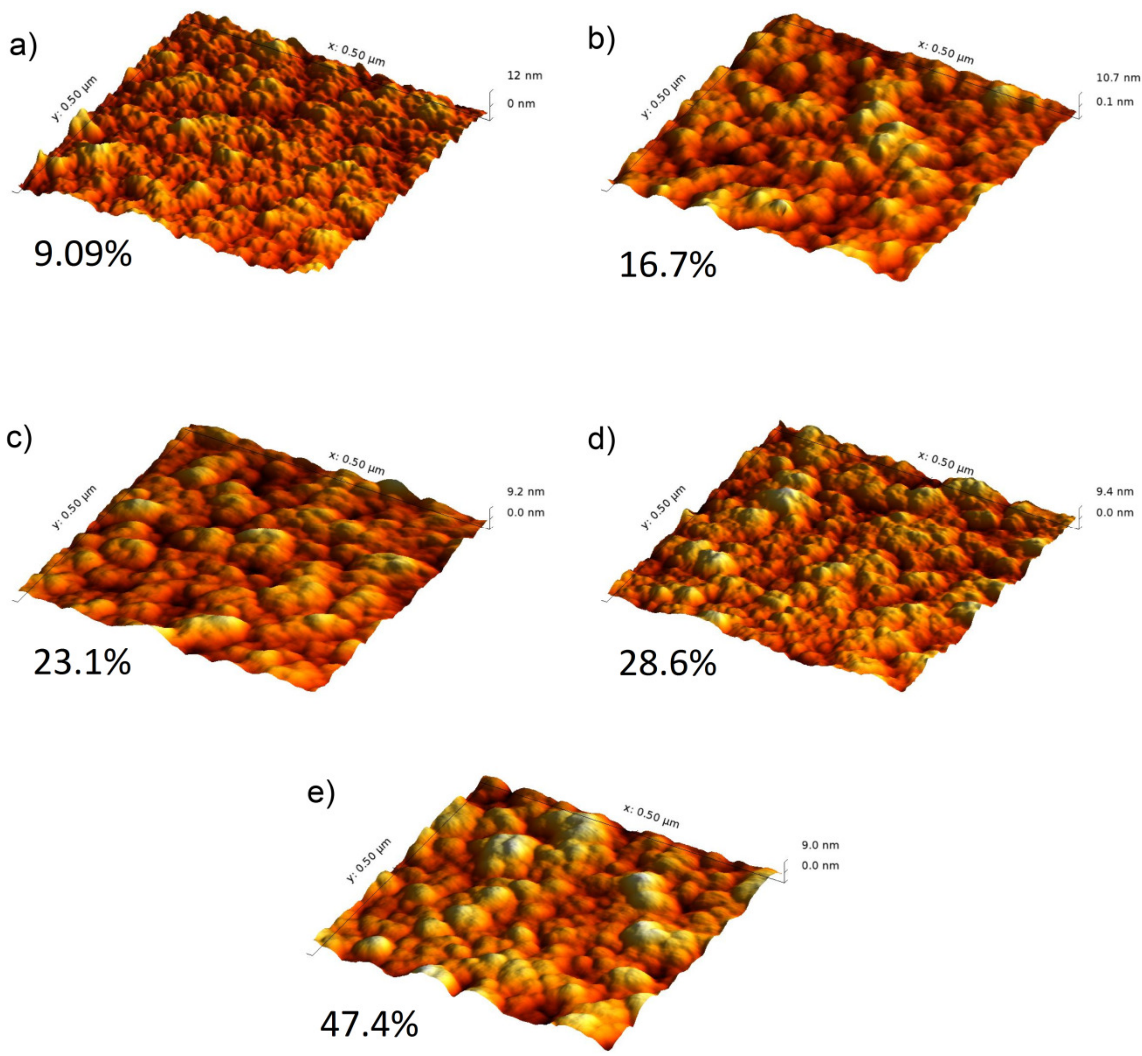

Figure 5.9: 3D AFM maps of fig. 5.8 for samples with different $R(N_2O)$ content. Tip used: NSG10-DLC.

The correlation length ξ increases linearly with the nitrogen dioxide content. A linear fit of the data reveals that ξ = $\left(18.3 + 0.2 \cdot R(N_2O)\right)$ nm (fig. 5.10). The MGS calculated with watershed method shows approximately the same trend but the errors associated with these results are bigger because watershed analysis is more sensitive to measurement noise. The correlation length ξ is probably linked to the grains size and not to the clusters.

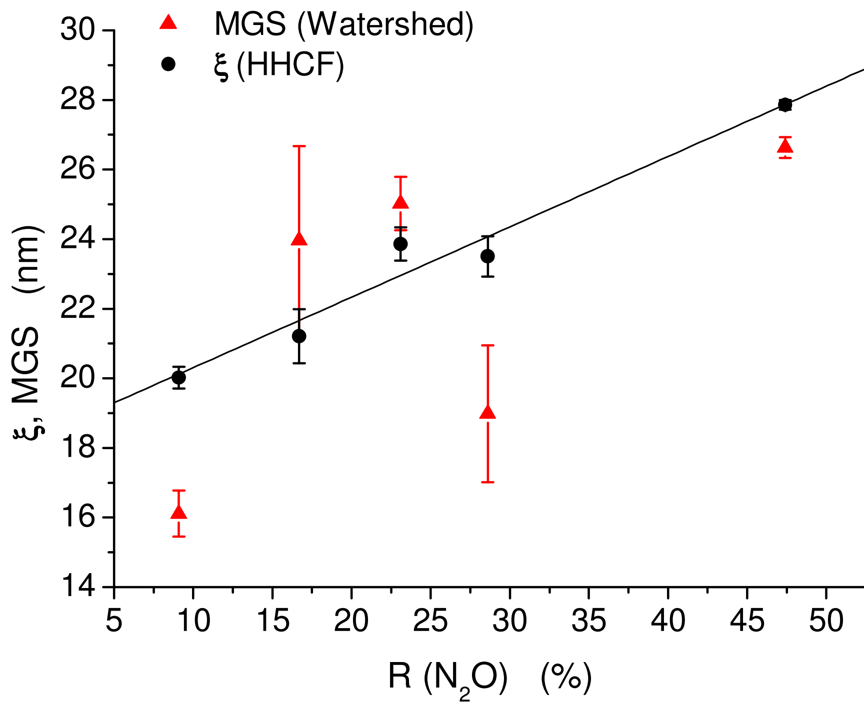

Figure 5.10: ξ and MGS plotted as function of $R(N_2O)$. *Tip used: NSG10-DLC.*

5.4 Changes in the Morphology Induced by the Growth Substrate

In order to measure the optical transmittance of nc-SiO_xN_y films, the optical characterization of the nc-SiO_xN_y films would impossible on films grown on a silicon wafer, because the silicon absorbs the visible and near-UV light. To allow measurements the films are have been grown also low-absorption glass substrate.

First of all three films have been analyzed with the AFM (GI-0, GI-3, GI-6) and they all show the presence of clusters which have not been observed on layers deposited on Si (fig. 5.12). It is observed that these clusters are always isolated and circular, randomly scattered on the surface. These circular structure, present only on films grown on glass, should be related to the glass substrate itself [36]. The consequence of the presence of these isolated structures is an increasing of the RMS roughness and therefore of the theoretical Total Integrated Scatter TIS (eq. 3.41).

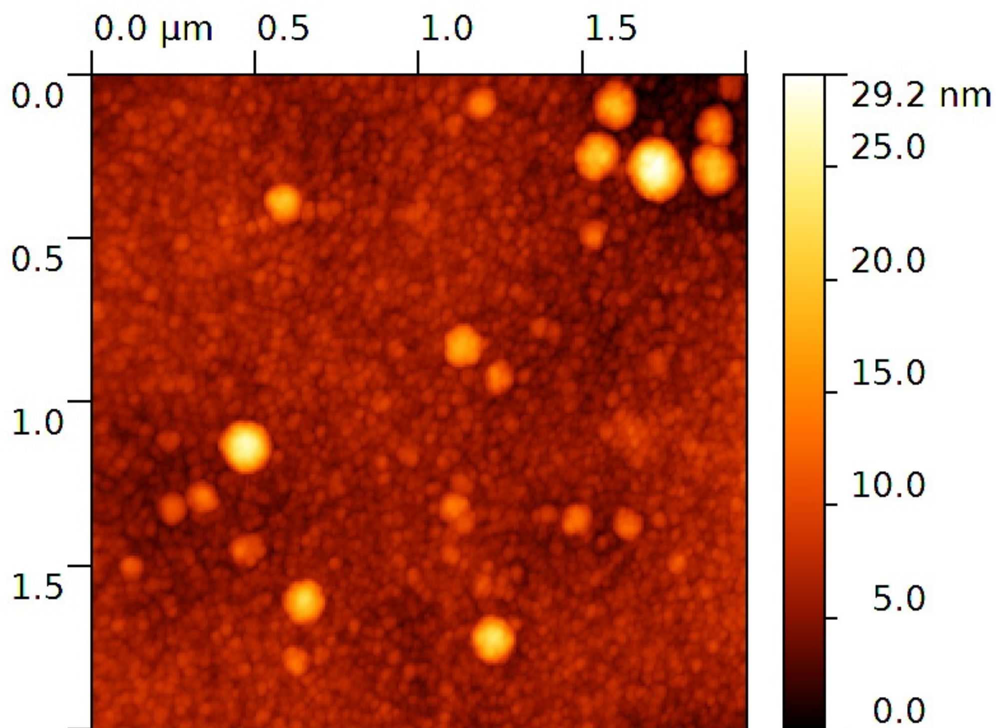

Figure 5.12: AFM map of the sample GI-3 (R_{N_2O}= 9.09% and $R_{B_2H_2}$= 2.34%) grown on glass substrate. The RMS roughness R is (2.2±1.1) nm. Tip used: NSG10.

5.5 Annealing Effect on Optical Properties

The optical properties of the nc-SiO_xN_y films are studied with transmission and reflection measurements. The spectral region investigated ranges from 350 nm to 600 nm. The experimental setup used is described in chapter 4.

First of all, it is necessary to measure the transmittance T_{glass} (eq. 3.29) and the reflectance R_{glass} (eq. 3.40) of an high transmission glass on which the nc-SiO_xN_y films are grown. The experimental results are shown in fig. 5.13. It is possible to observe from the data that T_{glass} and R_{glass} are constant and their average values are respectively 0.92 and 0.09. The transmittance T associated to a nc-SiO_xN_y:H film grown on a high-transmission glass is:

$$T = \frac{I_T}{T_{glass} \cdot I_0}, \tag{3.39}$$

where I_0 is the light intensity incident on the nc-SiO_xN_y film and I_T the intensity transmitted by the entire system.

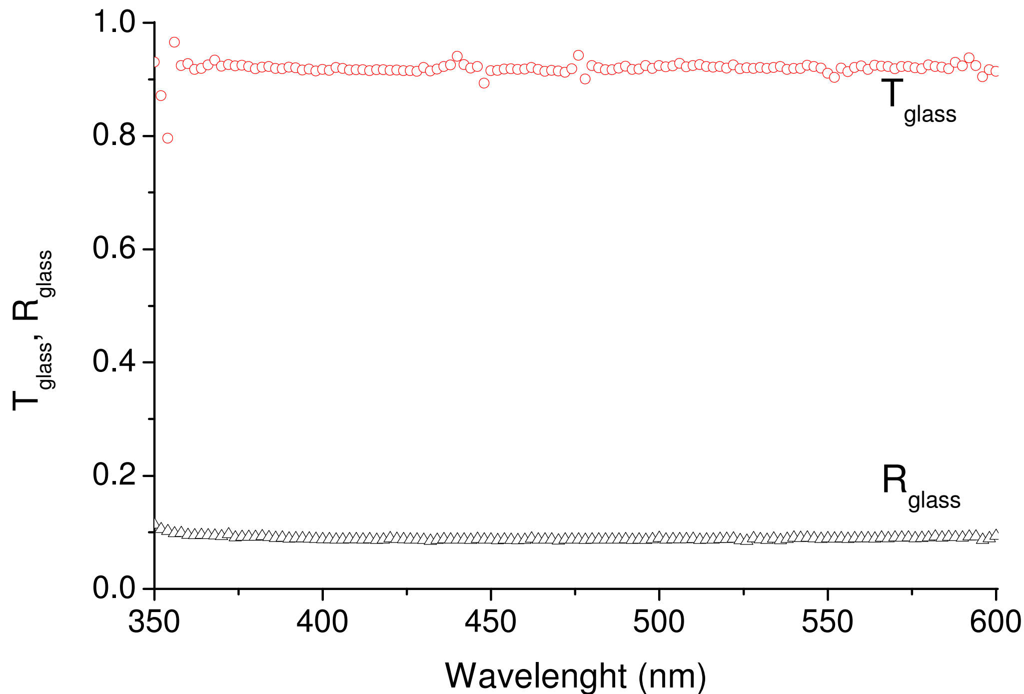

Figure 5.13: Transmittance T and reflectance R of an high transmission glass used as substrate for the nc-SiO_xN_y films.

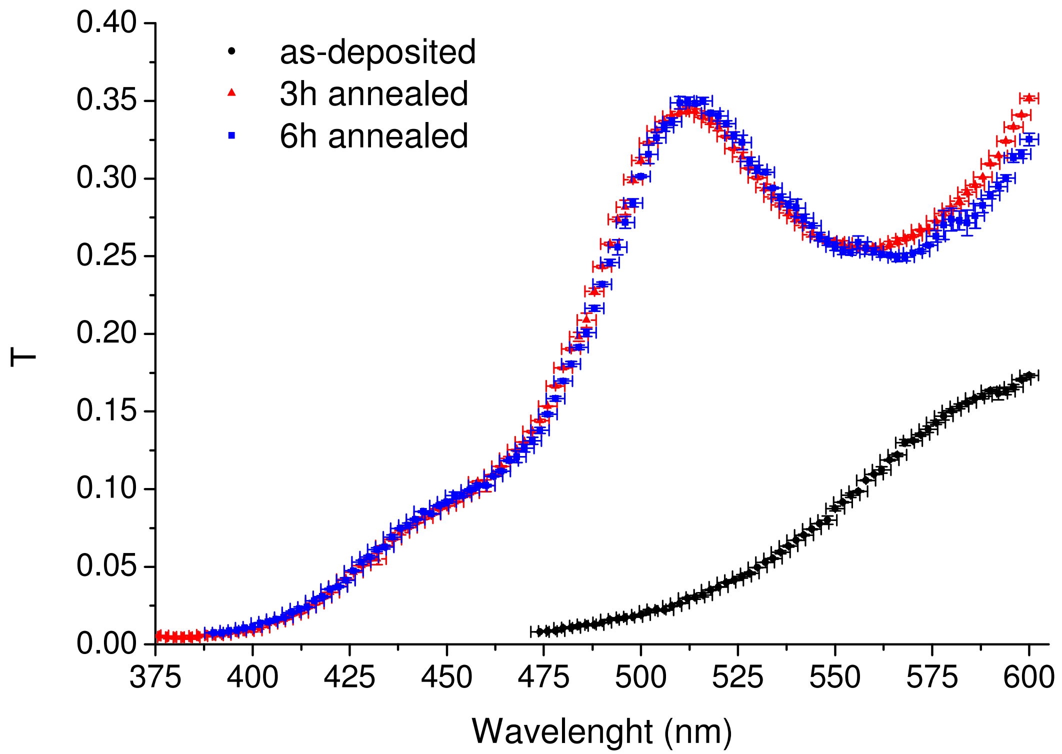

Figure 5.14: Transmittance T of the samples GI-0, GI-3 and GI-6. $R(B_2H_6)$ *= 2.34 % and* $R(N_2O)$ *=9.09%.*

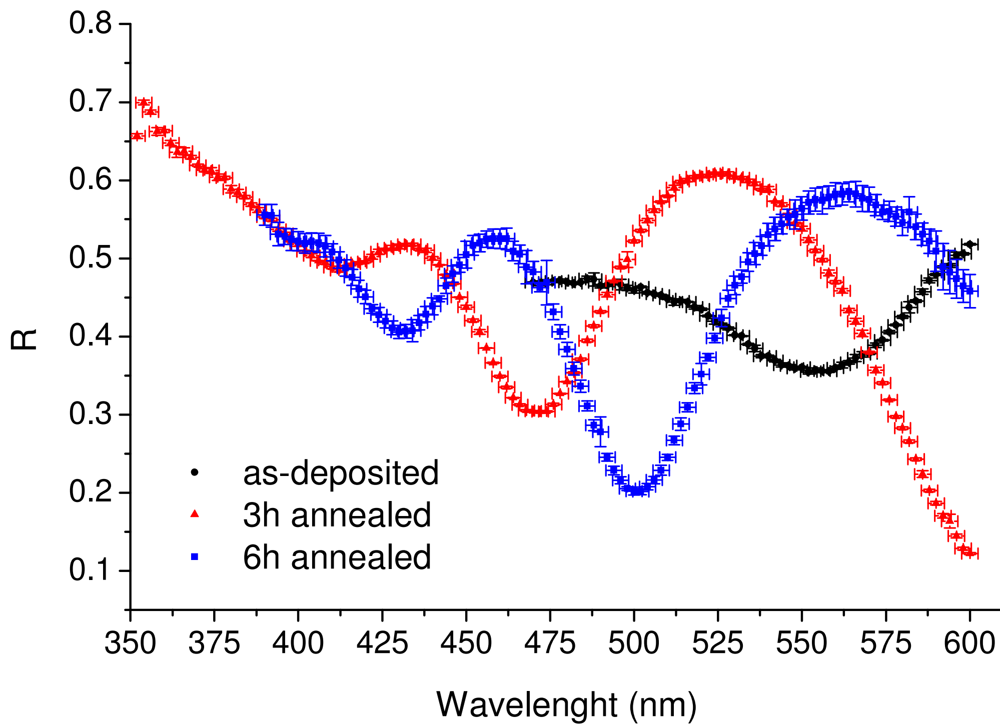

Figure 5.15: Reflectance R of the samples GI-0, GI-3 and GI-6. $R(B_2H_6)$ *= 2.34 % and* $R(N_2O)$ *=9.09%.*

Transmission measurements are done for the samples listed in tab. 4.2 – 4.5. The wavelength step is 5 nm for the samples in tab. 4.2 – 4-4 and 2 nm for the samples in tab. 4.5. Reflectance measurements are done only for the samples listed in tab. 4.5 and the wavelength step is 2 nm. An interesting result is that the transmittance spectra of the samples with low $R(N_2O)$ change significantly after the thermal treatment (fig. 5.14). In particular it is observed that the *T* of the as-deposited samples is much lower at lower wavelength than the *T* of the 3 and 6 hours annealed samples. Furthermore no significant difference in the transmittance of 3 hours and 6 hours annealed samples is observed. This effect can be explained by the increase of the crystalline phase after the annealing treatment evidenced by Raman measurements [7].

The simulations done by Veronesi [38] with the software Optical [39] show that the transmittance of amorphous (a-Si) and crystalline (c-Si) silicon thin films exhibit similar behavior to the experimental one of the nc-$\mathrm{SiO_xN_y}$ layers, as shown by fig. 5.16.

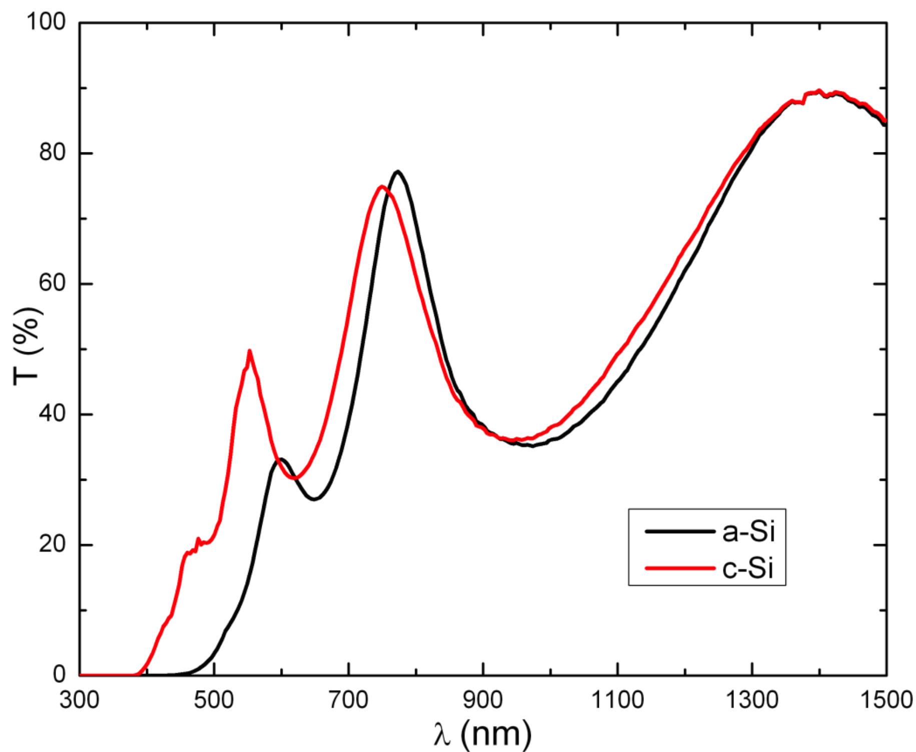

Figure 5.16: Simulated transmittance T of a-Si and c-Si [38].

The thin-film interference effect is visible in all the transmittance spectra but it is less evident for the as-deposited films: this happens because the high absorption destroys the interference effect that is visible for higher wavelengths. Also the reflectance spectra are suffering from the thin-film interference effect as shown in figure 5.15.

The energy gap of the nc-SiO_xN_y films is estimated by the optical band-gap energy E_{OPT} using the Tauc equation for amorphous semiconductors (3.36):

$$(\alpha \cdot \hbar\omega)^{1/2} = B(\hbar\omega - E_{OPT}), \quad (3.36)$$

where ħω is the photons energy. The absorption coefficient α is defined by the equation (3.45):

$$\alpha(\omega) = \frac{1}{d} ln\left(\frac{1-R}{T}\right), \quad (3.43)$$

where *R* and *T* are reflectance and transmittance of a film with thickness *d*. The equation (3.36) is well defined only in the high absorption region. This region is typically characterized by $\alpha(\omega) > 10^5\ cm^{-1}$ and the thin-film interference effects are negligible. The plot of $(\alpha \cdot \hbar\omega)^{1/2}$ versus the photons energy-axis gives the optical band-gap energy E_{OPT} (fig 5.17).

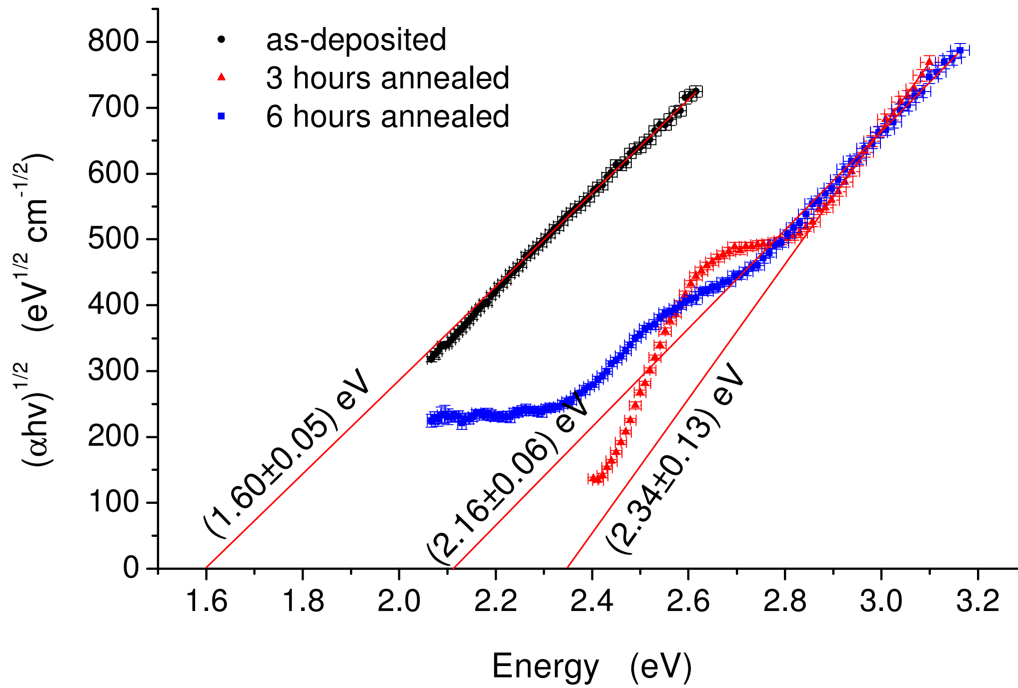

Figure 5.17: Measure of the optical band-gap energy E_{OPT} using the Tauc equation (3.30) for samples with different annealing treatment. $R(B_2H_6)$ = 2.34% and $R(N_2O)$ =9.09%.

At constant $R(B_2H_6)$ equal to *2.34%,* the optical band-gap values E_{OPT} as function of the annealing time are measured for different $R(N_2O)$. The experimental results obtained for the sample listed in tab. 4.5 are summarized in tab. 5.4 and plotted in fig. 5.18.

Sample	Annealing time (hours)	$R(N_2O)$ (%)	E_{OPT} (eV)
GI-0	0	9.09	1.60±0.05
GL-0	0	16.7	1.67±0.06
GM-0	0	23.1	1.71±0.07
GN-0	0	48.0	2.00±0.02
GI-3	3	9.09	2.34±0.13
GL-3	3	16.7	2.14±0.10
GM-3	3	23.1	1.99±0.01
GN-3	3	48.0	2.06±0.07
GI-6	6	9.09	2.16±0.06
GL-6	6	16.7	2.01±0.15
GM-6	6	23.1	2.08±0.08
GN-6	6	48.0	1.94±0.14

Table 5.4: Optical band-gap E_{OPT} for samples with different annealing time and $R(N_2O)$. $R(B_2H_6)$ is fixed at 2.34 %.

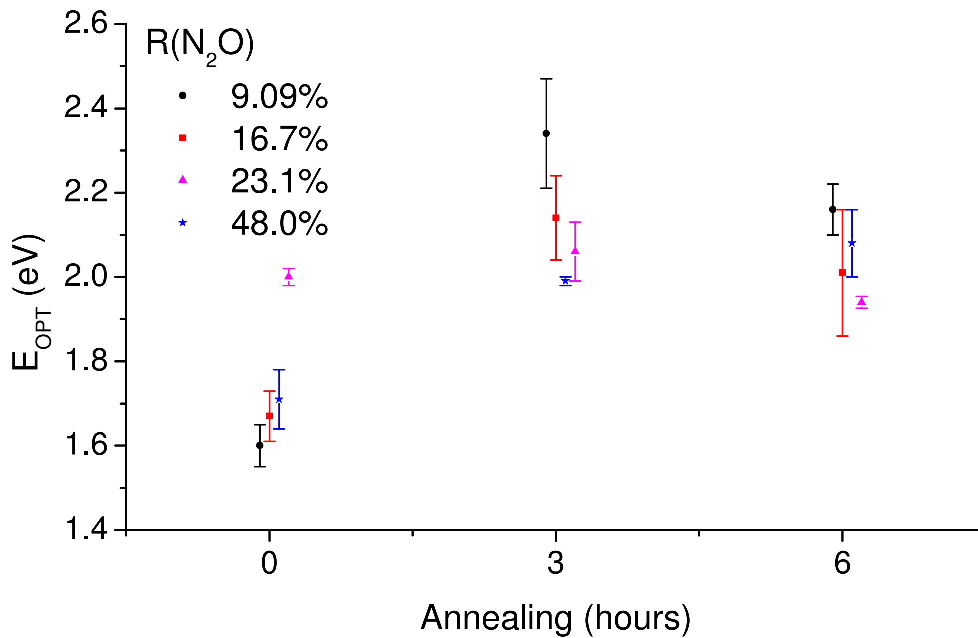

Figure 5.18: Optical band-gap E_{OPT} as a function of the annealing time for samples with different $R(N_2O)$. All the samples have $R(B_2H_6)$ = 2.34 %.

From the result obtained it is possible to observe that the optical band-gap E_{OPT} depends on the annealing time. After the first three annealing hours, E_{OPT} increases and after further three hours appears to decrease. This effect is maximum for the sample with low $R(N_2O)$ values and for the sample with $R(N_2O)$ = 48% is almost negligible.

5.6 R(N_2O) Effects on Optical Properties

Using the values in tab. 5.4 it is possible to study the effects of $R(N_2O)$ on the transmittance and the optical band-gap E_{OPT} of the nc-SiO_xN_y:H films.

The spectra of the as-deposited samples with different $R(N_2O)$ reveal that the transmittance is related to this parameter (fig. 5.19). Increasing $R(N_2O)$ results in a blue-shift of the cutoff wavelength ad an increase of the transmittance at all the wavelengths.

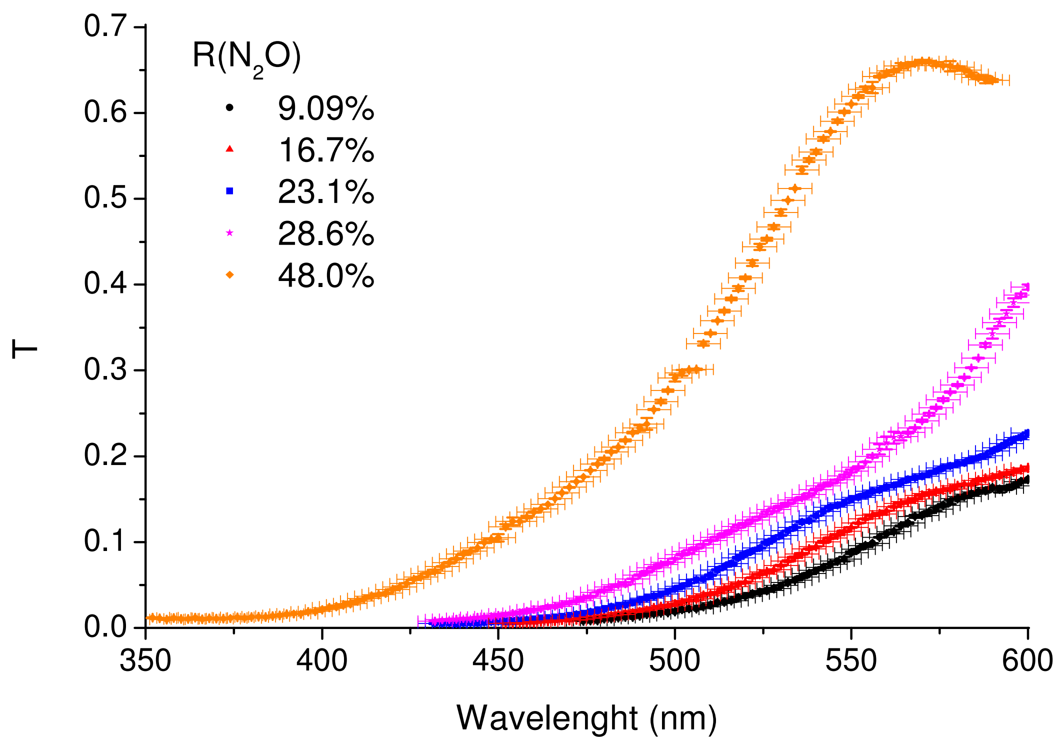

Figure 5.19: Transmittance T of the as-deposited samples with $R(B_2H_6)$ = 2.34 % at different $R(N_2O)$.

The optical band-gap E_{OPT} is plotted as function of $R(N_2O)$ in fig. 5.20. In this graph it is possible to notice that the annealing treatment is less efficient for high values of

$R(N_2O)$. The energy gap of the nc-SiO_xN_y films in the as-deposited state is a linear function of $R(N_2O)$:

$$E_{OPT} = \left(1.47 + 0.01 \cdot \mathrm{R(N_2O)}\right) eV.$$

These results are very important because in order to optimize the HIT solar cell efficiency the nc-SiO_xN_y film will have energy gap and transmittance as high as possible.

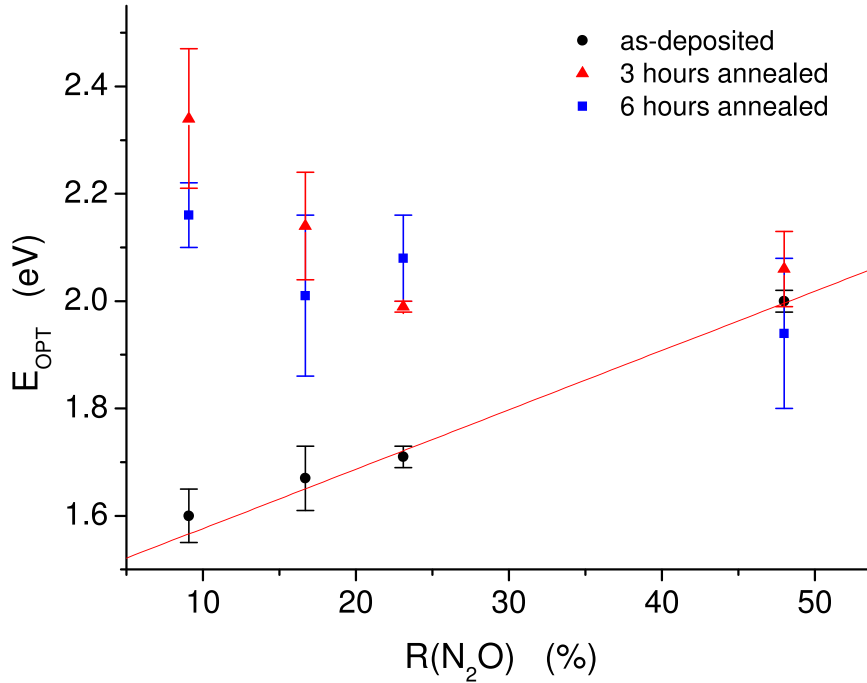

Figure 5.20: E_{OPT} as function of $R(N_2O)$ for samples with different annealing time. All the samples have $R(B_2H_6)$ = 2.34 %.

5.7 The Effects of Doping on the Optical Properties and the Band Structure

Phosphine (PH_3) or dioborane (B_2H_6) is added to precursor gases in order to achieve n- or p-doped nc-SiO_xN_y films. Samples with different doping (tab. 4.2 – 4.4) are analyzed only by transmission measurements (spectral range: 350-600 nm, step: 5 nm). The absorption coefficient $\alpha(\omega)$ is mainly influenced by scattering and absorption losses. In high absorption region ($\alpha(\omega) > 10^5\ cm^{-1}$) the absorption may be obtained from the transmittance T by the following equation [40]:

$$\alpha(\omega) = \frac{1}{d} ln\left(\frac{1}{T}\right). \qquad (3.43 \text{ bis})$$

Using the Tauc's formula (3.36) it is possible to determine the optical band-gap energy E_{OPT}.

The crystal disorder and its impact on the band structure of nc-$\mathrm{SiO_xN_y}$ is estimated studying the absorption coefficient for $\alpha(\omega) > 10^5\ cm^{-1}$. In these interference-free regions a plot of equation $\alpha(\mathrm{E}) = a_0 \cdot e^{(\mathrm{E}-E_1)/E_0(X,T)}$ provides the width $E_0(X,T)$ of the Urbach tails (fig.5.20).

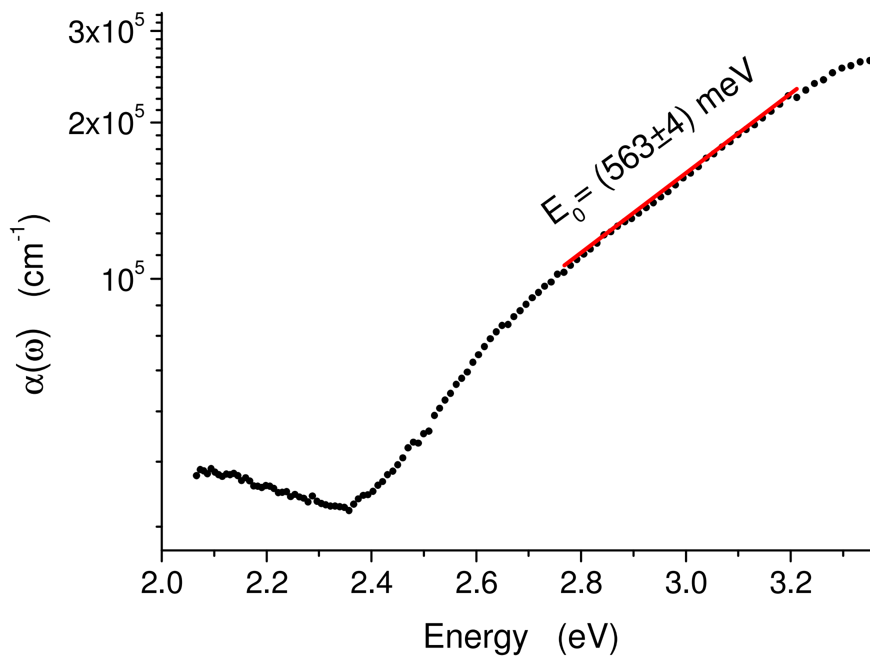

Figure 5.20: Absorption coefficient $\alpha(\omega)$ of the sample GH-3.

The experimental results (tab. 5.5 - 5.7) show that E_{OPT} values change for p-type, n-type or intrinsic samples.. The optical-energy gaps of the intrinsic nc-$\mathrm{SiO_xN_y}$ films are comparable with the gaps of p-type films. N-type samples show E_{OPT} values higher than the ones of p-type intrinsic samples. As the investigated samples show not only different dopant, but also different deposition conditions, the observed difference in E_{OPT} cannot be ascribable to the difference of the dopant. It is noteworthy that all the investigated samples large values of Urbach tails (ranging from 524 to 563 meV) have been measured. This demonstrated the large crystal disorder of these structures.

Sample	Annealing time (hours)	$R(N_2O)$ (%)	$R(PH_3)$ (%)	E_{OPT} (eV)	E_0 (meV)
GA-3	3	16.7	2.34	2.40±0.13	364±8
GA-6	6	16.7	2.34	2.36±0.12	339±8
GB-3	3	16.7	1.19	2.47±0.13	337±5
GB-6	6	16.7	1.19	2.49±0.14	324±5
GC-3	3	9.09	2.34	2.40±0.13	407±7
GC-6	6	9.09	2.34	2.39±0.12	382±10

Table 5.5: Optical band-gap and Urbach tails of n-type samples. These samples have been deposited with the same RF power and low plasma hydrogen content.

Sample	Annealing time (hours)	$R(N_2O)$ (%)	$R(B_2H_6)$ (%)	E_{OPT} (eV)	E_0 (meV)
GD-3	3	28.6	1.19	2.17±0.13	473±5
GD-6	6	28.6	1.19	2.23±0.13	475±5
GE-3	3	28.6	1.19	2.13±0.11	479±4
GE-6	6	28.6	1.19	2.10±0.15	511±12
GF-3	3	28.6	1.19	2.11±0.16	480±6
GF-6	6	28.6	1.19	2.12±0.12	481±10
GG-3	3	28.6	1.19	2.04±0.08	467±6
GG-6	6	28.6	1.19	2.08±0.09	476±7

Table 5.6: Optical band-gap and Urbach tails of p-type samples. These samples have been deposited with different RF power and plasma hydrogen content.

Sample	Annealing time (hours)	$R(N_2O)$ (%)	E_{OPT} (eV)	E_0 (meV)
GH-0	-	9.09	2.14±0.04	558±4
GH-3	3	9.09	2.10±0.08	563±4
GH-6	6	9.09	2.10±0.04	536±3

Table 5.7: Optical band-gap and Urbach tails of undoped samples.

Conclusions

Notwithstanding silicon HIT shows the highest efficiency among the Si-based solar cells, emitter layer based on a-Si:H can be responsible for factors decreasing the solar cell efficiency like light parasitic absorption, high resistivity or light induced degradation effects. The proposed substitution of a-Si:H with nc-SiO_xN_y can contribute to the enhancement of HIT efficiency.

The optical and morphological properties of nc-SiO_xN_y films have been studied in view of the their application in silicon hetero-junction solar cells. In particular the effect of oxygen content and the annealing treatments on the surface characteristics and optical properties have been investigated.

The AFM maps reveals the presence of grains which can be associated to clustering of nano-crystals related to both annealing time and N_2O content of plasma used for deposition, defined by $R(N_2O)$ (eq. 4.1). In particular it is has been observed that the size of the grains increase and the clustering becomes evident after the annealing treatment. Two different method have been used to analyze AFM data, one of them allows for the estimation of the mean grains size and the other of the correlation length. These two morphological parameters can be related to the grains dimensions and shown similar trend versus deposition parameters. The understanding of the surface morphological features is of main importance for optimization and use of this material in HIT cells where appropriate surface treatments are necessary for enhancement light trapping.

The optical properties of nc-SiO_xN_y films have been investigated in the spectral range 350-600 nm. The optical transmittance of the films increases after three annealing hours, in addition a blue shift of absorption edge is observed. The energy gap is estimated using the Tauc gap for disorder semiconductors E_{OPT}. The optical data show that the E_{OPT} of the as-deposited samples is a linear function of $R(N_2O)$. The annealed samples have higher E_{OPT} than the as-deposed ones but the annealing treatment is less effective for higher values of of $R(N_2O)$. The optical gaps obtained range from 1.60 to 2.49 eV, values always higher than the a-Si:H ones.

List of Abbreviations

AC	Alternate Current.
ACF	AutoCorrelation Function.
AFM	Atomic Force Microscope.
a-Si	amorphous silicon.
a-Si:H	hydrogenated amorphous silicon.
a-SiO_x	amorphous silicon oxide.
a-SiO_xN_y	amorphous silicon oxy-nitride.
$\alpha(\omega)$	absorption coefficient.
CB	Conduction Band.
CIGS	Cooper-Indium-Gallium-Diselenide.
c-Si	crystalline silicon.
CVD	Chemical Vapor Deposition.
DC	Direct Current.
DLC	Diamond Like Carbon.
DSP	Digital Signal Processor.
E_g	energy gap.
E_{OPT}	optical energy gap (Tauc energy gap).
FET	Field-Effect Transistor.
HHCF	Height-Height Correlation Function.
HIT	Hetero-junction with Intrinsic Thin-layer.
i(a-Si)	intrinsic-amorphous silicon.
IR	InfraRed light.
I_R	intensity of reflected light.
I_T	intensity of transmitted light.
I_0	incoming light on the surface of the sample.
LR	Learning Rate.
MGS	Mean Grain Size.

mc-Si multy-crystalline silicon.

nc-SiO_xN_y nano-crystalline silicon oxy-nitride.

nc-SiO_xN_y nano-crystalline silicon oxy-nitride.

nc-Si nano-crystalline silicon.

PECVD Plasma Enhanced Chemical Vapor Deposition.

PSD Phase-Sensitive Detector.

PSDF Power Spectral Density Function.

PV PhotoVoltaic.

PZT lead zirconium titanate: $Pb(Zr_xTi_{1-x})O$.

QDSC Quantum Dot Solar Cell.

R reflectance.

*R** root-mean square roughness (eq. 2.4).

RF Radio Frequency.

RMS Root Mean Square.

R_{ss} theoretical reflectance of a perfectly smooth surface.

SEM Scanning Electron Microscope.

Si:H hydrogenated silicon.

SiO_xN_y silicon oxy-nitride.

SWE Staebler-Wronsky Effect.

T transmittance.

TCO Thin Conductive Oxyde.

TIS Total Integrated Scatter.

UV UltraViolet light.

VB Valence Band.

η solar cell efficiency.

ξ lateral correlation lengths.

Bibliography

[1] http://www.iea.org/.

[2] http://www.statista.com/.

[3] http://www.ise.fraunhofer.de/en.

[4] F. Köhler, T. Zimmermann, S. Muthmann, A. Gordijn, R. Carius, Structural order and Staebler–Wronski effect in hydrogenated amorphous silicon films and solar cells, IEEE Journal of Photovoltaic, vol. 4, n. 1, 2014.

[5] M. A. Green, The path to 25% silicon solar cell efficiency: history of solar cell evolution, Progress in Photovoltaics, vol. 17, p.183-189, 2009.

[6] D. Abou-Ras, T. Kirchartz, U. Rau, Advanced characterization techniques for thin film solar cells, WILEY-VCH, 2011.

[7] M. Perani, N. Brinkmann, A. Hammud, D. Cavalcoli, B. Terheiden, Nanocrystal formation in silicon oxy-nitride films for photovoltaic applications: optical and electrical properties. Article submitted.

[8] M. Pellicione, T. Lu. Evolution of thin films morphology - modeling and simulations, Ed. Springer, 2007.

[9] Y. Zhao, G. Wang, T. Lu. Characterization of amorphous and crystalline rough surface: principles and applications. Experimental methods in the physical science, vol. 37. Ed. Academic Press, 2001.

[10] M. S. Dresselhaus, Solid state physics - part II, optical properties of solids. Free download notes: http://web.mit.edu/course/6/6.732/www/6.732-pt2.pdf

[11] L. D. Landau, E. M. Lifšits, Teoria dei Campi. Fisica teorica 7. Ed. Riuniti, 3° edizione: 2004.

[12] M. Grundmann, The physics of semiconductors - an introduction including devices and nanophysics, Ed. Springer, 2002.

[13] J. Tauc, R. Grigorovici, A. Vancu, Optical properties and electronic structure of amorphous germanium. Phys. Status Solid 15, p.627-37, 1966.

[14] G. D. Cody, B. G. Brooks, B. Abels. Optical absorption above the optical gap of amorphous silicon hydride. Sol. Energy Mat., p.8-231, 1982.

[15] Y. Hishikawa, N. Nakamura, S. Tsuda, S. Nakano, Y. Kishi, Y. Kuwano, Interference-free determination of the optical absorption coefficient and the optical gap of amorphous silicon thin films, Japanese Journal of Applied Physics, vol.30, n.5, p.1008-1014, May 1991.

[16] Vorliček, M. Závětová, S. K. Pavlov, L. Pajasová, On the Optical Gap of Amorphous Silicon, Journal of Non-Crystalline Solids 45, p.289–292 (1981).

[17] R. H. Klazes, M. H. L. M. van der Broek, J. Bezemer, S. Radeleer, Mag. B B45, p.377 1982.

[18] S. Nitta, S. Itoh, M. Tanaka, T. Endo, A. Hatano. Sol. Energy Mater. 8, p.249, 1982.

[19] R. V. Kruzelecky, C: Ukah, D. Rakansky, S. Zukotynsky, Interband Optical absorption in amorphous silicon, Journal of Non-Crystalline Solids 103, p.234-348, 1988.

[20] G. D. Cody, T. Tiedje., B. Abels, B. G. Brooks, Y. Goldstein, Disorder and the optical-absorption edge of hydrogenated amorphous silicon, Physical Review Letters, vol. 47, num. 20, p.1480-1483, 1981.

[21] V. Sa-Yakanit, H. R. Glyde, Urbach tails and disorder, Comments Cond. Mat. Phys, vol. 13, num. 1, p.35-48, 1987.

[22] B. I. Halperin and Melvin Lax, Impurity-Band Tails in the High-Density Limit. I. Minimum Counting Methods, Phys. Rev. 148, p.722, 1966.

[23] W. Sritrakool, V. Sa-yakanit, and H. R. Glyde, Band tails in disordered systems, Phys. Rev. B 33, p.1199, 1986.

[24] J. Tauc, Amorphous and liquid semiconductors, ed. By J. Tauc, Plenum Press – London and New York, 1974.

[25] O. Stenzel, The physics of thin film optical spectra, Ed. Springer, 2005.

[27] N. Brinkmann, D. Sommer, G. Micard, G. Hahn, B. Terheiden, Electrical, optical and structural investigation of plasma-enhanced chemical-vapor-deposited amorphous silicon oxynitride films for solar cell applications. Solar Energy Materials & Solar Cells 108, p.180-188, 2013.

[28] H. E. Bennett, J. O. Porteus, Relation between surface roughness and specular reflectance at normal incidence, Journal of the Optical Society of America, vol. 51, n.2, p.123-129, 1961.

[28] http://www.oxford-instruments.com.

[29] X. Deng, E. A. Schiff, Amorphous Silicon–Based Solar Cells, in Handbook of Photovoltaic Science and Engineering (eds A. Luque and S. Hegedus), John Wiley & Sons, Ltd, Chichester, UK, ch.12, 2003.

[30] S. Hama, H. Okamoto, Y. Hamakawa, T. Matsubara, Journal of Non-Crystalline Solids 59-60, p.333, 1983.

[31] http://www.ntmdt.com.

[32] V. L. Mironov, Fundamentals of scanning probe microscopy, the Russian Academy of Science, Institute of Physics of Microstructures, Nizhniy Novgorod, 2004.

[33] http://people.whitman.edu/.

[34] http://www.hamamatsu.com.

[35] http://www.thinksrs.com/.

[36] F. Detto, Silicio cristallino per applicaizoni fotovoltaiche studiato mediante tecniche di microscopia a forza atomica, University of Bologna, 2008.

[37] H. Yang, Y. Zhao, A. Chan, T. Lu, G. Wang, Sampling-induced hidden cycles in correlated random rough surfaces, Phys. Rev. B 56, 4224, 1997.

[38] M. Veronesi, Studio di proprietà ottiche di SiON con simulazioni software, University of Bologna, 2013.

[39] https://www.bo.imm.cnr.it/users/centurioni/optical.html.

[40] M. Sreemany, S. Sen, A simple spectrophotometric method for determination of the optical constants and band gap energy of multiple layer TiO_2 thin films, Materials Chemistry and Physics 83, p.169-177, 2004.

Publications

Martina Perani, Enrico Di Russo, Nils Brinkmann, Barbara Terheiden, Daniela Cavalcoli, Morphology of multiphase and functional thin films by atomic force microscopy. E-MRS Spring Meeting, Lille, may 2014.

Ringraziamenti

Al termine di questa tesi di laurea è doveroso ricordare tutti coloro che hanno dato, seppure in modi diversi, un contributo alla stesura di questa tesi.

Uno speciale ringraziamento va alla Prof.ssa D. Cavalcoli, la quale ha reso possibile questo lavoro, dandomi fiducia e autonomia nella fase sperimentale, e che mi ha guidato lungo questo percorso fino alla correzione finale dei testi. In particolare un grazie per avermi sempre supportato, ma soprattutto - cosa non facile - sopportato.

A M. Perani un doveroso ringraziamento per il supporto tecnico e i preziosi suggerimenti che mi ha fornito. La sua collaborazione è stata indispensabile, specie nella fase di revisione finale della tesi.

Si ringrazia il Dipartimento di Fisica dell'Università di Costanza per aver messo a disposizione capacità e mezzi per depositare i film analizzati in questa tesi. In particolare si ringrazia A. Hammud per le immagini HRTEM.

Parecchie delle misure ottiche sono state realizzate in collaborazione con M. Giangolini e M. Veronesi, i quali hanno contribuito anche alla realizzazione del programma che ha permesso l'analisi degli spettri. Il loro contributo e la loro disponibilità sono stati molto importanti.

Uno speciale ringraziamento a tutto il personale del Settore di Fisica Della Materia, dai tesisti fino ai docenti. In particolare grazie a: Giorgio M., Stefania C., Giulia V., Antonio C., Maurizio S., Marco. C., Marco M., Alberto B., Andrea C., Laura B., Isacco G..